THEORETICAL AND EXPERIMENTAL MULTI-SCALE STUDY OF AN ARTIFICIAL BONE CONSTRUCT: FROM TIBIAL OSTEOTOMY TO CELL/FLUID INTERACTION

THÈSE N^{O} 3841 (2007)

PRÉSENTÉE LE 13 JUILLET 2007
À LA FACULTÉ DES SCIENCES ET TECHNIQUES DE L'INGÉNIEUR
Laboratoire de biomécanique en orthopédie EPFL-HOSR
PROGRAMME DOCTORAL EN MÉCANIQUE DES SOLIDES ET DES FLUIDES

ÉCOLE POLYTECHNIQUE FÉDÉRALE DE LAUSANNE

POUR L'OBTENTION DU GRADE DE DOCTEUR ÈS SCIENCES

PAR

Luc Dominique BLECHA

ingénieur mécanicien diplômé EPF
de nationalité suisse et originaire de Genève (GE)

acceptée sur proposition du jury:

Prof. L. Laloui, président du jury
Prof. D. P. Pioletti, Prof. L. Rakotomanana, directeurs de thèse
Prof. C. Jacobs, rapporteur
Prof. M. Swartz, rapporteur
Dr P.-Y. Zambelli, rapporteur

ÉCOLE POLYTECHNIQUE
FÉDÉRALE DE LAUSANNE

Suisse
2007

Natura non nisi parendo vincitur
(Nature to be commanded must be obeyed)
– Francis Bacon 1561 - 1626

Acknowledgments

This work was the fruit of collaboration between researchers of the Ecole Polytechnique Fédérale de Lausanne, the Hôpital Othopédique de la Suisse Romande and University of Rennes I (France). Financial support was provided by the Swiss National Science Foundation (FNRS No. 2100-066872.01/1 and and No. 205320-105940/1), the Fondation Lémanique pour la Recherche sur le Tissu Osseux and the Lausanne Center for Bone Tissue Engineering.

First, I would like to thank my two thesis directors Prof. Dr. D. P. Pioletti at the Laboratory for Biomechanical Orthopaedics EPFL-HOSR and Prof. Dr. L. Rakotomanana at the Institut de Recherche en Mathématique de Rennes (France).

I am very grateful to Prof. Dr. D. P. Pioletti for his daily support, his valuable advice and the confidence he showed in my work throughout the PhD preparation. I especially appreciated his friendly, open-minded character and his excellent teaching skills. In addition to his high quality intellectual support, I also thank him for his constant attention that ensured an optimal and stimulating environment in the lab.

I owe much thanks to Prof. Dr. L. Rakotomanana, who warmly welcomed me in Rennes. The four stays I had the chance to spend there were very intellectually and personally enriching. I am extremely respectful of his intellectual honesty and straight-forward thinking that greatly contributed to the success of this work.

This multi-disciplinary work would not have been possible without the precious contribution of Prof. P.-F. Leyvraz, director of the Hôpital Ortopédique de la Suisse Romande and PD. MER Dr. P.-Y. Zambelli, senior surgeon at the same hospital. I owe to Prof P.-F. Leyvraz much thanks for his pertinent remarks and advice that contributed to the clinical relevance of this work. I am very grateful to PD. MER Dr. P.-Y. Zambelli for having generously shared his accurate and detailed medical knowledge as well as his clinical experiences. His contribution was essential as he supervised the clinical aspects and the medical dimension of this work.

I give much thanks to Dr. F. Razafimahery who was always ready to fill his black board with equations and discuss mathematical and mechanical issues. He also helped on the resolution of numerical problems and is a friendly source of enriching knowledge.

Many thanks to Dr. L. A. Laurent-Appelgate who encouraged me throughout the duration of the PhD, gave precious information and advice on the biological aspects of the project and is always ready and willing to explain biological issues to an engineer.

A special thanks to Dr. L. Mathieu who processed for the first time PLLA foam during her PhD thesis. In addition to her major intellectual contribution, she actively and generously processed all the PLLA samples that were used in this study.

I am very grateful to Prof. M. Bohner and Dr Robert Mathys Fondation who provided the ChronOs samples that were used in this study.

All the mechanical parts that were necessary for the experimental part of this work are

the fruit of a successful collaboration with the mechanics and biomechanics workshop. The technical excellence of the team composed of M. Jeanneret, S. Haldner and N. Favre greatly accelerated the design and manufacturing of the dozens of items that were developed. They not only helped on the design but also anticipated the possible problems that could have been encountered during the use of these wonderful tools.

I would like also to express my gratitude to Dr. N. Ramaniraka and Dr. A. Terrier who offered their knowledge and the numerical tools they developed. Besides their technical assistance, I had the chance to share some privileged moments with them during coffee breaks and international congresses.

Many thanks to M. Bergomi from the Laboratory of Applied Mechanics and Reliability Analysis EPFL who showed me the use of the Instron compression test bench and to Prof. Dr. I. Botsis who kindly permitted my access to it.

I owe much thanks to the Lyncée Tec team that permitted the use of their innovative digital holographic microscope. Especially, I would like to thank Dr. P. Marquet who led and coordinated the collaboration and B. Rappaz, T. Colomb and P. Jourdain who generously helped me and taught me how to use the microscope.

I would like to highlight the patience, the availability and professionalism of Sandra Jacoud, our lab assistant, who was always willing to help me in the lab and ready to try new methods. I thank her for all the work she carried out and for all the advice and background knowledge she generously offered me.

Many thanks to Jane Cantova and Mark Newson who agreed to correct this document at the last minute.

Many thanks to the lab secretary, Virginie Kokocinski who was always willing to find the best solution for organizational issues, for her daily good mood and for the friendly discussions we had.

My everyday life at the lab was greatly brightened by all the people with whom we shared our thoughts, doubts, hopes, experiences and views on professional as well as private topics. Namely, many thanks to Aurélie, Corinne, Cynthia, Ana, Katarina, Claire, Arlette, Miguel, Arne, Francesco, Vincent, Marc-Olivier, Tom, Loic, Hicham, Pierre-Jean, Ermano, Philippe.

Many thanks to the students who worked on this projet: Marco Martin, Sylvain Iff and David Atlani.

I would like to express my happiness to be supported by my perfect parents, my delightful sister, the affectionate Bustamante-Masana family and my rocking friends.

Finally, I owe everything to Vera who was always willing to help and who maintained my mental health. Indeed, she always brought her sunshine with her which makes life much more fun.

Abstract

Synthetic bone substitutes are potentially the future gold standard in orthopaedic and traumatologic surgery. The availability of these bone substitutes with different biomechanical properties may well replace autografts in the future as they overcome complications associated with the graft harvesting procedure. In addition, bone substitutes have the potential to replace allografts as the risk of virus transmission may be greatly reduced. However, the biomechanical properties of the new bone substitute should be carefully analyzed to identify optimal parameters and configurations that are likely to favor an enhanced osteointegration. In this thesis, a multi-scale approach is adopted to systematically screen the impact of different mechanical parameters on the bone substitute osteointegration and to propose an optimized solution.

At a large length scale (0.5 m), the impact of the bone substitute size, position and mechanical properties is studied to optimize the substitute osteointegration. In the particular case of open wedge tibial osteotomy, the development of a finite element model achieves this goal. It is found that a wedge covering one fourth of the osteotomy and placed posteriomedially together with an anteromedial supporting plate is likely to reduce the fibrous tissue ingrowth at the wedge/bone interface. In addition, the maximum stresses in the bone substitute and in the tibia are computed to be smaller for wedges with stiffness in the range of 0.5 to 3 GPa. Finally, it is suggested that patients should use crutches during the first post-operative weeks to favor the bone ingrowth at the wedge/bone interface and to limit the risk of tibial head fracture or wedge failure.

At an intermediate length scale (10 mm), the bone substitute is no longer considered as a bulk material but as a construct: a porous solid material impregnated with fetal bone cells and saturated with a fluid. Such a construct is likely to be a competitive alternative to bone allografts or autografts. However, its biomechanical properties need to be adapted to each particular clinical application to favor its osteoinduction and osteointegration. Therefore, the systematic screening that was initiated at the large length scale is pursued to identify the optimal fluid conductivity and porous mechanical properties as a function of the mechanical environment.

A general algorithm based on the poroelasticity theory is proposed to determine the target fluid conductivity and the mechanical properties of the construct. Maximal fluid volume exchange between the construct and its environment is researched whilst bearing in mind that the average fluid-induced shear stress will stay within a defined range for an optimal stimulation of the bone cells. In the particular case of open wedge tibial osteotomy, an optimized construct would be a porous material that has a stiffness of 0.5 GPa, a Poisson's ratio of 0.1, a porosity larger than 50% and a permeability of $1 \cdot 10^{-10}$ m^2.

Poroelasticity based on mechanical and fluid conductivity tests identifies the optimal mechanical environment of PLLA-5%βTCP porous material. It appears that oscillating stresses in the range of 0-0.4 MPa are associated with optimal fluid-induced stimulation of the embedded bone cells. Finally, a constitutive viscoelastic description of the construct is proposed, which can be used to determine the mechanical environment of the PLLA-5%βTCP constructs in a given clinical application.

At a small length scale (400 μm), the mechanical interaction that takes place between bone cells attached to the pore walls and the moving fluid is likely to modulate the dynamic fluid-induced shear stress. A theoretical model of this phenomenon identifies the novel dimensionless number N_{fs} that indicates whether the cells' mechanical stimulation might be damped or amplified. This dimensionless number highlights the central role of the pore size. It is computed that pore diameters smaller than 100 μm are likely to significantly reduce the dynamic stimulation of bone cell. On the other hand, pore diameters larger than 300 μm are found to permit an undamped mechanical stimulation. It is thus hypothesized that constructs with pore diameters larger than 300 μm would more efficiently stimulate the embedded bone cells which appear to be especially sensitive to high frequency mechanical stimulation.

Keywords: bone tissue engineering, biomechanics, bone substitute, open wedge tibial osteotomy, poroelasticity, viscoelasticity, PLLA, fluid structure interaction, orthopedic surgery.

Résumé

Les substituts osseux synthétiques vont probablement devenir la référence en matière de greffons osseux en orthopédie et en traumatologie. En effet, la disponibilité de nouveaux substituts osseux adaptables à différentes applications cliniques devrait rapidement remplacer les autogreffes qui sont souvent source de complications liées à l'opération de prélèvement du greffon. L'utilisation de substituts osseux pourra également remplacer les allogreffes et ainsi éliminer le risque de transmission de virus du donneur au receveur. Par contre, l'analyse détaillée des propriétés biomécaniques de ces nouveaux substituts osseux est indispensable afin d'identifier les caractéristiques et les configurations optimales favorisant l'ostéo-intégration. C'est dans ce but qu'une approche multi-échelle a été développée. Les différents niveaux d'observation ont permis d'analyser l'impact de plusieurs caractéristiques mécaniques sur l'ostéo-intégration du substitut osseux et de proposer un cahier des charges optimal.

A un niveau d'observation large (0.5 m), l'influence de la taille, de la position et des propriétés mécaniques du substitut osseux a été étudiée afin d'optimiser son ostéo-intégration. Dans le cas particulier de l'ostéotomie tibiale d'ouverture, un modèle par éléments finis a permis d'identifier les caractéristiques favorables. Une configuration comprenant un coin couvrant un quart d'ostéotomie, positionné postéro-médialement et associé à une plaque de support en position antéro-médiale semble réduire la probabilité de croissance de tissus fibreux à l'interface entre l'os et le coin. De plus, les contraintes maximales dans le substitut osseux et dans le tibia sont apparues moins importantes lorsque la rigidité du substitut osseux est comprise entre 0,5 et 3 GPa. Cette échelle d'analyse a aussi mis en évidence l'avantage qu'ont les patients à utiliser des béquilles durant les premières semaines suivant l'opération. Ceci, d'une part, pour favoriser la croissance de l'os dans la zone d'interface entre le coin et l'os, et d'autre part pour réduire les risques de fracture de la tête tibiale et de rupture du coin.

A un niveau d'observation intermédiaire (10 mm), le substitut osseux n'est plus considéré comme un matériau plein, mais comme un *construct*, c'est-à-dire une structure poreuse, imprégnée de cellules føetales osseuses et saturée par un fluide. Du point de vue de l'ostéo-induction et de l'ostéo-intégration, un tel construct pourrait être une alternative intéressante à l'allo- et l'auto-greffe. Ceci à la condition d'en adapter les propriétés biomécaniques aux différentes applications cliniques. L'analyse à cette échelle a été approfondie dans le but d'optimiser la conductivité du fluide et les caractéristiques mécaniques du construct à un environnement mécanique donné.

La poroélasticité a permis de concevoir un algorithme général pour déterminer la conductivité du fluide et les propriétés mécaniques optimales du construct. Sachant que la contrainte de cisaillement moyenne induite par le fluide devrait être comprise dans un certain intervalle pour une stimulation optimale des cellules osseuses, l'objectif a été de mettre en évidence les caractéristiques favorisant un échange maximal de fluide entre le construct et son environnement.

Dans le cas particulier de l'ostéotomie tibiale d'ouverture, un construct optimal aurait les caractéristiques suivantes: un matériau poreux d'une rigidité de 0.5 GPa, d'un coefficient de Poisson de 0.1, d'une porosité supérieure à 50% et d'une perméabilité de $1 \cdot 10^{-10}$ m^2.

Basé sur des tests mécaniques et de conductivité du fluide, la poroélasticité a aussi permis d'identifier l'environnement mécanique optimal d'un matériau poreux PLLA-5%βTCP. Il est apparu que des oscillations comprises entre 0 et 0.4 MPa sont associées à une stimulation optimale des cellules osseuses. Une loi constitutive viscoélastique a été développée, celle-ci pouvant être utilisée pour déterminer l'environnement mécanique du PLLA-5%βTCP dans une application clinique donnée.

A un niveau d'observation microscopique (400 μm), l'interaction mécanique entre les cellules osseuses adhérentes aux pores du matériau et le fluide semble moduler la contrainte de cisaillement dynamique. Un modèle théorique de ce phénomène a mis en évidence un nouveau nombre adimensionnel N_{fs} qui indique si la stimulation mécanique des cellules est amplifiée ou amortie par cette interaction. Ce nombre adimensionel met en évidence le rôle prépondérant de la taille des pores. En effet, les pores de moins de 100 μm semblent amortir significativement la stimulation dynamique des cellules osseuses. Par ailleurs, des pores d'un diamètre de plus de 300 μm éliminent cet amortissement. Ceci a amené à émettre l'hypothèse qu'un construct avec des pores de diamètre supérieur à 300 μm stimule plus efficacement les cellules osseuses. Ces dernières sont en effet particulièrement sensibles aux stimulations mécaniques de haute fréquence.

Mots-clés: ingénierie tissulaire de l'os, biomécanique, substitut osseux, ostéotomie tibiale d'ouverture, poroélasticité, viscoélasticité, PLLA, interaction fluide structure, chirurgie orthopédique.

Contents

Acknowledgments **i**

Abstract **iii**

Résumé **v**

1 Introduction **1**
1.1 Objectives 2
1.2 Outlines 4

2 Open Wedge Tibial Osteotomy **5**
2.1 Clinical Background 5
2.1.1 Open Wedge Tibial Osteotomy 6
2.1.2 Autograft 8
2.1.3 Allograft 9
2.1.4 Synthetic Bone Substitute 10
2.2 Biomechanical Model 12
2.2.1 Method 12
2.2.2 Material Properties 14
2.2.3 Loading and Boundary Conditions 14
2.2.4 Periosteum Elongation Model 16
2.2.5 Experimental Determination of the Maximal Jaw Force 17
2.2.6 Effects of Friction Coefficient 18
2.3 Effects of the Supporting Plate Position 19
2.3.1 Micromotions 20
2.3.2 Stresses 20
2.3.3 Conclusions 21
2.4 Effects of Wedge Geometry 22
2.4.1 Micromotions 23
2.4.2 Stresses 24
2.4.3 Octahedral Strains 25
2.4.4 Economic and Handling Aspects 26
2.4.5 Conclusions 27

2.5 Effects of Wedge Stiffness 28
2.5.1 Micromotions 28
2.5.2 Stresses 29
2.5.3 Octahedral Strains 30
2.5.4 Conclusions 30
2.6 Discussion 31
2.7 Conclusions 33

3 Porous Construct for Artificial Bone Substitute 35
3.1 Biological Aspects of an Artificial Bone Graft 36
3.2 Cell Delivery Systems 37
3.2.1 Fibrin Gel as Cell Carrier 38
3.2.2 Culture Medium as Cell Carrier 40
3.2.3 Conclusions 42
3.2.4 Perspectives 43
3.3 Mechanical Behavior of the PLLA Bone Construct 43
3.3.1 Mechanical Testing of PLLA Bone Construct 44
3.3.2 Construct Continuum Description 48
3.3.3 Conclusions 57
3.4 Fluid Motion in PLLA Bone Construct 58
3.4.1 Continuum Mechanics of Porous Media 59
3.4.2 Fluid Motion in a Cylindrical Sample 63
3.4.3 Application to a PLLA-5%βTCP Construct 65
3.4.4 Results 67
3.4.5 Discussion on Fluid Motion 72
3.5 Conclusions 76

4 The Interaction Between Fluids And Cells 79
4.1 A One Dimensional Cell/Fluid Model 81
4.1.1 Assumptions & Governing Equations 81
4.2 The Analytical Solution 83
4.2.1 The Interfacial Shear Stress 83
4.2.2 The Cell Layer Deformation 86
4.3 Numerical Validation 87
4.3.1 Effect of Large Deformations on Interfacial Shear Stress 88
4.3.2 Effect of Excitation Frequency on Interfacial Shear Stress 89
4.4 Applications To Osteoblasts in PLLA Construct 89
4.5 Discussion and Conclusions 92

5 Conclusions and Perspectives 95
5.1 Conclusions 95
5.2 Perspectives 98

A Glossary 99

B Fluid Flow in a Poroelastic Cylinder 103

C Average Wall Shear Stress 109

D Analytical Solution of the Cell/fluid Interaction Problem 111

E Derivation of N_{fs} 115

References 121

Curriculum Vitae 137

Publications 139

CHAPTER 1

Introduction

Recent enhancements of surgical techniques together with increasing expectations regarding the quality of life and the aging of the world's population have resulted in a rapid growth of the number of skeletal reconstruction surgeries. The number of bone-grafting procedure reached an estimated 1.3 million per year in 2002 worldwide and this figure is likely to reach 3 million interventions in 2010 [76].

Bone grafts are used in many applications such as filler of bone cavities due to tumor or impacted fracture, arthroplasty revision, traumatology surgery, spine fusion and open wedge tibial osteotomy. Most of the bone grafts used today are natural bone harvested on the same patient (autograft) or taken from a bone bank (autograft). These procedures present good clinical results but come with clinical complications and are in limited supply. An alternative to natural bone graft is synthetic bone substitute.

Synthetic bone substitute is likely to become a major clinical advance in bone reconstruction surgery. Indeed, synthetic bone graft may avoid the long term pain caused by the autograft harvesting procedure that was reported in 25% of cases [178]. In addition, the risk of virus transmission associated with allograft [15] may be avoided by synthetic bone graft as the sterility of the manufacturing process is controlled.

However, the biomechanics of synthetic bone graft is not yet fully understood and must be studied carefully to obtain a competitive alternative to auto and allograft. Although the medical objectives of grafts are known, their optimal biomechanical properties are not always accurately defined. A systematic screening of the graft biomechanical properties for each application might help to identify the optimal configuration to enhance the likelihood of successful surgical procedure.

The bone mechanics and, by extension, bone substitute mechanics are multi-scale and complex phenomena. For instance, the cellular activity and gene expression which are phenomena taking place at micro and nanometer length scales modulate the macroscopic bone resistance. Macroscopic phenomenon such as mechanical loading due to physical activity or being overweight may also impact cell activity and gene expression. The bone mechanics complexity results from the biological activity that ensures a constant remodeling and repair of bone. The balance of activity between the bone forming cells (osteoblasts) and the bone resorbing cells (osteoclasts) determines the bone structure and mass density. It is regulated by many factors and the exact biophysical phenomena involved in these processes are not yet fully understood.

However, the bone formation/resorption balance was found to be impacted by many aspects, for instance gender [55], ethnicity [9, 137], age and menopausal status [86, 95], total body mass index[1] [195], fat mass [204], calcium and D vitamin intake [30] and physical activity [158, 189]. In particular, the physical activity is shown to enhance bone mass [128], whereas bed rest [197] or microgravity exposure [170] reduces bone mass. Nevertheless, the macroscopic mechanical properties of the bone substitute as well as its internal 3D architecture are parameters that may be tuned to enhance the bone substitute efficiency.

A three length scales approach is adopted to assess the role of the biomechanical properties observable at these length scales on specific phenomena (see Figure 1.1 for a schematic summary). At a large length-scale, the effect of bone substitute mechanical properties, overall size and position are studied to optimize its osteointegration. The biomechanical environment of the optimal graft configuration sets the framework to study the impact of phenomenon taking place at smaller length-scales. At an intermediate length scale, the fluid conductivity properties of the bone substitute are studied to maximize its osteoinductivity and osteogenesis. The fluid motion inside the synthetic bone graft due to the mechanical environment defined at the larger length-scale is then studied at a small length scale. The impact of the cell/fluid mechanical interaction on the cell mechanical stimulation is investigated to identify the local parameters that play a dominant role. This phenomenon is likely to impact the bone graft osteoinduction and osteogenesis and may require specific 3D internal architecture of the graft.

1.1 Objectives

The principal objective of the thesis is to identify the optimal biomechanical parameters of a porous artificial bone construct to maximize its osteointegration and osteoinduction. The use of bioengineered porous construct in clinics is recent and many theoretical as well as practical aspects still need to be studied. It is thus proposed to investigate the impact of some of these aspects from a biomechanical point of view. In the particular case of open wedge tibial osteotomy, the optimal mechanical properties, size and location of the construct shall be evaluated bearing in mind economical and practical considerations. Then, the optimal construct characteristics for fluid conductivity shall be examined so that the fluid volume exchange between the construct and its environment is maximized. The average fluid-induced shear stress due to the fluid volume exchange should be within the range which favor the production of an extracellular matrix by bone cells. Finally, the dynamic coupling phenomenon between the moving fluid and the deformable cell layer attached on the construct pore walls shall be studied to assess which are the key parameters and what are the effects of such phenomenon.

The second objective is to determine the mechanical and fluid conductivity characteristics of a PLLA-5%βTCP porous construct that was developed at EPFL by Dr. L. Mathieu [118]. First, the maximal dynamic loading history that can be applied to these constructs shall be quantified so that their range of applications may be defined. Second, a constitutive law describing the construct bulk volume shall be proposed as well as its evolution as a function of the number of mechanical loading cycles. Finally, the porous construct permeability and porosity shall be measured for the subsequent evaluation of the construct fluid conductivity and mechanical-induced fluid motion.

---

[1] The total body mass index (BMI) is defined by the ratio of patient mass to the square of their height.

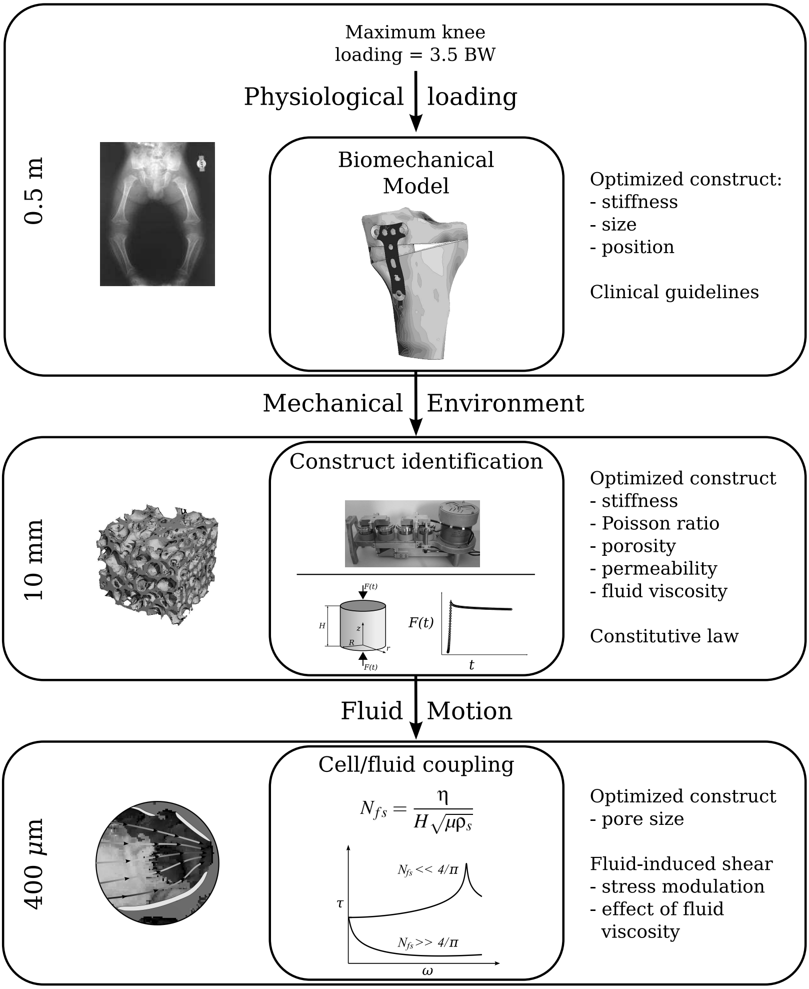
Maximum knee
loading = 3.5 BW
Physiological loading
0.5 m
Biomechanical
Model
Optimized construct:
- stiffness
- size
- position
Clinical guidelines
Mechanical Environment
10 mm
Construct identification
F(t)
H
z
R
r
F(t)
F(t)
t
Optimized construct
- stiffness
- Poisson ratio
- porosity
- permeability
- fluid viscosity
Constitutive law
Fluid Motion
400 μm
Cell/fluid coupling
$N_{fs} = \frac{\eta}{H\sqrt{\mu\rho_s}}$
τ
$N_{fs} << 4/\pi$
$N_{fs} >> 4/\pi$
ω
Optimized construct
- pore size
Fluid-induced shear
- stress modulation
- effect of fluid
viscosity

Figure 1.1: Schematic view of the multiscale approach used in this study. At a large length scale (0.5m), the mechanical environment is determined to optimize the construct stiffness, size and position. At an intermediate length scale (10 mm), the fluid conductivity and construct mechanical properties are optimized with regards to the fluid exchange and fluid-induced shear stress. At a small length scale (400 μm), the cell/fluid interaction phenomenon may modulate the fluid-induced shear stress and define a minimal pore diameter.

The third objective is to find a suitable method to embed bone cells inside the porous construct. The method shall be efficient and harmless for the cells. In addition, such a method shall be user-friendly and have low associated costs so that future use in the operating theater may be possible.

1.2 Outlines

The thesis is divided into three chapters that focuses on three different length scales as portrayed in Figure 1.1.

In chapter 2, the clinical and mechanical framework is set by the open wedge tibial osteotomy. General considerations on the graft requirements and on the available graft material are presented. Then, a numerical biomechanical model is presented which permitted the testing of several mechanical and spatial configurations. Bearing in mind the economical consequences of each configuration, an optimized configuration is proposed.

Then, chapter 3 focuses on the artificial construct definition and mechanical behavior at an intermediate length scale. Based on basic biological considerations, the construct is proposed to be made of a porous PLLA-5%βTCP skeleton filled with fetal bone cells and culture medium. Then, the experimental and theoretical characterization of the construct's mechanical behavior are presented. Finally, the experimental identification of the construct fluid conductivity characteristics are presented together with a theoretical study on the mechanically induced fluid motion inside the construct.

In chapter 4, the mechanical interactions between the fluid motion inside the construct and the bone cells that colonize the pore walls are studied from a theoretical point of view. The impact of the cell/fluid interaction on the cell mechanical stimulation is examined to identify the parameter that might impact the bone cell mechanical stimulation. A minimal pore diameter seems to be required so that the stimulation of bone cells is not damped for physiological excitation frequencies.

Finally, a glossary lists the definition of the words appearing in *italics* in this manuscript. At the very end, some mathematical developments are expanded upon in the appendices.

CHAPTER 2

Open Wedge Tibial Osteotomy

2.1 Clinical Background

It was estimated in 1995 that 15% of the North American population had some form of *osteoarthritis* [105]. This proportion is foreseen to increase to 18% in 2020. However, few risk factors for disease progression or functional decline have been identified so far [166]. Nevertheless, the mechanical malalignment of the lower limb[1] is identified as a risk factor for osteoathritis degeneration.

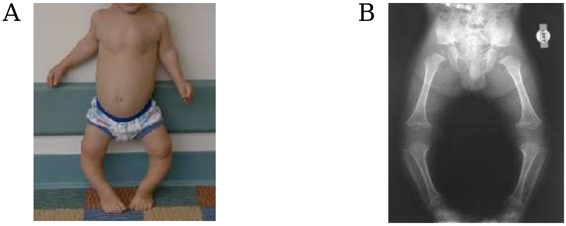

Figure 2.1: (A) Dramatic *varus* deformation of a child's lower limbs and (B) the corresponding radiograph [155].

Indeed, the alignment in the *coronal plan* of the knee with the ankle and the hip is essential for a good function of the lower limb; it is a key determinant in the load distribution between the two compartments of the knee (see Figure 2.1). In healthy humans, the hip-knee-ankle angle measures between 183 to 186°. The *weight-bearing line*, which is the line drawn from the mid femoral head to mid ankle, crosses the knee joint at a distance corresponding to 40% of the tibial plateau width from *medial* side (see Figure 2.2). It is estimated that the medial compartment of the knee supports 60% of the total joint load and the *lateral* compartment support the remaining 40% [50, 79].

---

[1] The human lower limb is defined anatomically as the limb of the body, extending from the hip to the ankle. The lower limb is separated into two segments called the thigh and the leg. The two segments are joined together by the knee.

However, many humans don't present an optimal hip-knee-ankle alignment. Either the lower limb turns outward away from the midline of the body or turns inward towards the midline of the body. In the first case, the lower limbs form an X and this deformation is called *valgus*. In the second case, the lower limb form an O which is due to a *varus* deformation (see Figure 2.1). The immediate consequence of these deformations is that the optimal load distribution between the lateral and medial knee compartments is not achieved. Overloading of one of the two compartments is taking place. Sharma et *al.* [166] succeed in relating the effect of the lower limb malalignment with knee osteoarthritis. The study shows that a deviation of more than 5° from the normal frontal femorotibial angle is associated with significantly greater function deterioration after as little as 18 months observation. Furthermore, the severity and the side of the deterioration correlates with the severity and side of the lower limb deformity. Therefore, it may be reasonably hypothesized that the restoration of an optimal frontal femorotibial angle in patients suffering knee osteoarthritis may stop or reverse the progression of the disease.

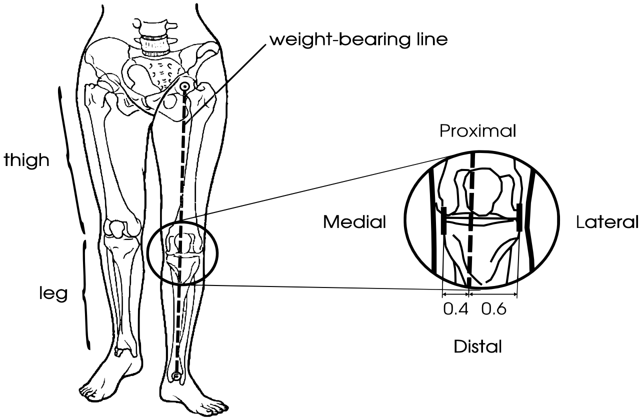

Figure 2.2: Human lower limb adapted from [89].

2.1.1 Open Wedge Tibial Osteotomy

One of the solutions proposed by traditional occidental medicine to prevent the osteoarthritis induced by varus or valgus lower limb deformation is high tibial osteotomy. The principle is to restore an optimal weight-bearing line by creating a cortical bone hinge on the lateral or medial side of the tibial head. That is achieved by cutting the tibia along its width, leaving a small thickness of *cortical bone*. In so-called open wedge tibial osteotomy, the surgeon leaves the cortical bone hinge on the side opposite to the direction of the lower limb deformation. The hinge is opened to the desired angle, and held in place by a wedge and a supporting plate (see

Figure 2.3). Conversely, the closing tibial osteotomy is achieved by removing a wedge of the patient's bone and leaving a cortical hinge on the side of the deformation. The tibia is then held in position with a metallic plate. Each of these surgical interventions has its drawbacks and advantages. For the sake of clarity and clinical relevance, the following discussion is restricted to the surgical intervention performed on a patient suffering from lower limb varus deformation.

Medial open wedge tibial osteotomy is a current surgical intervention for the correction of varus lower limb deformation. It is preferred to the lateral closing wedge osteotomy as numerous complications are avoided such as neurological complications [66], *compartment syndrome* [174], lateral muscle detachment, proximal *fibula* osteotomy and leg shortening [111]. In two clinical studies, better scores on open wedge than on closing wedge osteotomy are observed [6,100]. Moreover, the open wedge osteotomy is preferred as the difficulties encountered when performing a subsequent *total knee arthroplasty* are reduced [66].

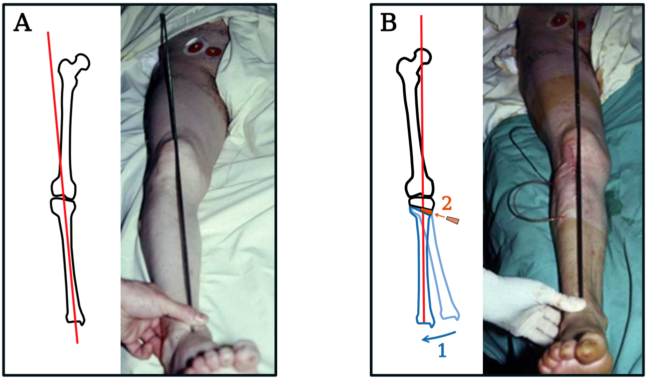

Figure 2.3: Principle of the open wedge tibial osteotomy. (A) Before the surgical intervention, the tibial axis differs from the weight bearing axis. (B) In order to restore a favorable weight bearing axis, the surgeon carries out a high tibial osteotomy, (1) opens the tibia to the desired angle and (2) introduces a wedge to maintain the tibia in this position.

The medial open wedge tibial osteotomy requires a supply of material to act as a wedge. Such material may be from natural source such as *allo* or *auto* bone graft and may also be a synthetic bone graft. Each of these possible solutions has its drawbacks and advantages which are exposed in sections 2.1.2-2.1.4.

There are four characteristics that an ideal bone graft material should exhibit which include [124]: (*i*) *osteointegration*, the ability to chemically bond to the surface of bone without an intervening layer of fibrous tissue; (*ii*) *osteoconduction*, the ability to provide a support on which bone cells can attach, migrate, grow and divide; (*iii*) *osteoinduction*, the capacity to stimulate primitive stem cells or immature bone cells to differentiate into mature, bone forming cells; and (*iv*) *osteogenesis*, the formation of new bone by osteoblastic cells present within the graft material. In addition, bone graft material should be mechanically resistant and offer a range of different stiffness characteristics depending on the location of implantation. Finally, the ideal bone graft substitute must be remodeled in a way that sufficient mechanical resistance and stiffness is ensured until complete substitute degradation.

In this chapter, the osteointegration as well as the mechanical resistance of a bulk graft was studied in the special case of open wedge tibial osteotomy. Using a mathematical approach, the internal forces taking place in the wedge, bone, supporting plate and screws were computed for maximal gait load and for different configurations. Based on these computations, an optimized configuration is proposed. But let's first review the existing bone graft materials that are the most used in surgery. They are composed of three main categories which are autografts, allografts and synthetic bone substitutes.

2.1.2 Autograft

Autogenous grafting (or autograft) describes the action of transferring cells, tissue or organs from one point to another of the same individual. In the particular case of bone autograft, it generally consists of harvesting bone from the patient's iliac crest and transferring it to the required location. The iliac crest provides easy access to good quality bone. The harvested autograft has proven optimal osteoinductive and osteoconductive and is not immunogenic. Furthermore, the mechanical properties of the graft may be modulated by harvesting cancellous bone or corticalo-cancellous bone graft. It can reach high resistance in bi-cortical iliac bone graft.

Although the autologous bone graft is nowadays the *golden standard*, it comes with complications. First, the harvesting of the bone graft lengthens the surgical intervention and the hospitalization. In terms of cost, it can be roughly estimated that the basic cost (without including costs related to complications) of an autograft harvest is equivalent to thirty minutes in the operating theater plus one additional hospitalization day. In 2007 and in Switzerland, this had a cost of about 1000 €. Second, the bone harvesting procedure induces between 5.8% [4] and 8.6% [202] of major donor site complications such as herniation of abdominal contents through bone graft donor sites (see Figure 2.4), vascular injuries, deep infections at the donor site, neuro-

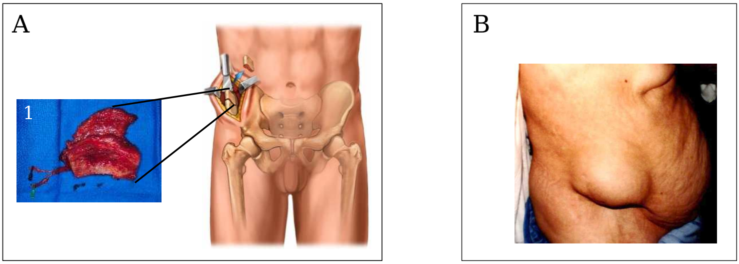

Figure 2.4: (A) Illustration showing the harvest of an autograft from the iliac crest and (1) an example of a freshly harvested autograft . (B) One of the major complications is the iliac crest hernia resulting from a defect in the *endoabdominal fascia* of the patient.

logical injuries, deep hematoma formation requiring surgical intervention, uretal injury, pelvic instability and iliac wing fractures.

In addition, one forth of the patients that underwent an iliac crest bone harvest procedure complain of chronic pain at the donor site [178]. Finally, the graft may fail at the host site due to loss of osteogenic agents subsequent to cellular death during transplantation [162].

In summary, the bone autograft is nowadays the golden standard although it is associated with 8.5-20% of major or minor complications at donor or host sites. It is therefore justified to research an alternative solution to autograft in order to avoid the donor site associated complications.

2.1.3 Allograft

Allografting designates the transfer of cell, tissue or organ between two individuals of the same species but of different *genotype*. Bone allograft is the surgeon's second choice after autograft and represents about one-third of the total bone grafting performed [15]. In 2006, mainly two types of bone allograft were used: frozen and freeze-dried bone, corresponding to the sterilization technique used. Both types of allografts are available in large quantities and in different forms allowing the surgeon to elaborate a customized treatment for each patient (see Figure 2.5). However, although efficient and systematic sterilization processes are used, an existing risk of virus transmission still exists. This was estimated to be 1 over 1.6 million for transmission of HIV [15]. Up to the year 2006, there was no recorded incident of fatal virus transmission through allografts. However, this risk remains like a sword of Damocles over the head of the allograft market.

Allografts available on the market in 2006 were rather expensive. Their price varied from one supplier to another and with size. Typically, an allograft used for open wedge tibial osteotomy costs in Switzerland and in 2006 between 370 € and 560 €. The use of allograft was thus cheaper than autograft.

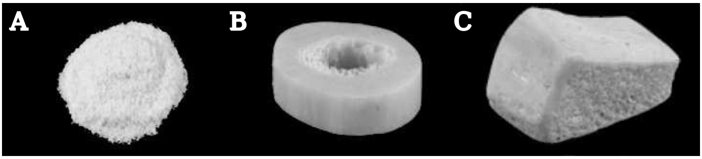

Figure 2.5: Allografts are available in several forms such as (A) powder, (B) bone section or (C) bone wedge. Whole bones are also available.

In addition to virus transmission, allografts may initiate immunological response at the host site due to the presence of cellular debris in the graft [15, 175]. The associated side effects of the sterilization are the loss of osteogenesis, a lower osteoinduction and lower mechanical properties than autografts. The more aggressive the sterilization is, the less osteoinductive and the weaker the allograft becomes. For instance, freeze-dried grafts are weaker and less osteoinductive than fresh-frozen grafts but induce a lower immune response [51].

To conclude, allografts are less osteoinductive, more immunogenic than autografts and present a low but non-negligible risk of virus transmission. However, allografts are available in large quantities, at least in Western countries[2], in various forms and have lower associated costs than autografts. Finally, the use of allograft shortens the operation time and eliminates the risks associated with the harvesting operation.

2.1.4 Synthetic Bone Substitute

Synthetic bone substitutes represent a fast growing industry that reached a market share of 16% of total bone grafting in 2005 [1] compared to 10% in 2002 [21]. A large number of bone-graft alternatives were commercially available for orthopaedic use in 2006. They varied in composition, mechanism of action and clinical efficiency. Their principal advantages are that they may be processed on an industrial scale and in many different forms, ensuring an unlimited and customized supply. Thanks to mass production, their cost might become less although the 2006 prices were still high. Again, their prices depend on the type of product and vary from one supplier to another, however an average price of about 115 € per cubic centimeter could be calculated[3]. Therefore, one of the major problem with large synthetic bone substitute volumes was their associated cost.

The principal categories of synthetic bone substitutes are cements, ceramics, polymers and composite materials (see Figure 2.6). Despite the wide variety of material, none of the EMEA[4] or FDA[5] approved products available in 2006 fulfilled all the requirements for an ideal bone graft. Most of them presented good osteoconduction characteristics, but poor osteoinduction and osteogenesis properties. Indeed, inclusion of growth factor or bone forming cells into the

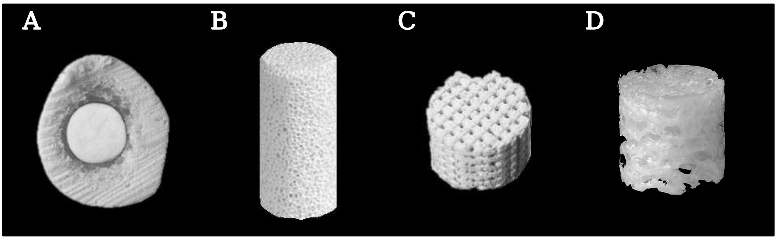

Figure 2.6: Different bone substitute: (A) Bone cement (Zimmer's Palacos, (B) Hydroxyapatite ceramic substitute (Mathys's ChronOs) (C) Bioactive Glass, (D) PLLA construct developed at EPFL.

---

[2] Organ donation, although encouraged by many religions, may be restricted by some others. For instance, the Shintoist may be reluctant to organ donation [126]

[3] The averaged price was based on the prices of Tutoplast®Spongiosa Block, Tutoplast®tutobone (Tutogen Medical GmbH, Germany), ChronOs™(Synthes, Switzerland) and Pro Osteon®(Biomet, Inc., USA). For more details see section 2.4.4.

[4] European Medicine Agency

[5] Food and Drug Administration

Table 2.1: Comparison between different bone graft materials.

Graft type	Osteo-induction	Osteo-conduction	Osteo-genesis	Immo-genicity	Mechanical strength	Mechanical stiffness	Fracture toughness
Autograft							
Cortical	+++	+++	+++	No	150 MPa	15 GPa	2-8 MPa$\sqrt{m}$
Cancellous	+++	+++	+++	No	4 MPa	0.3 GPa	0.1 MPa$\sqrt{m}$
Allograft							
Cortical frozen	++	+	No	Mid	150 MPa	14 GPa	2-8 MPa$\sqrt{m}$
Cortical γ-irradiated	No	+	No	Low	110 MPa	12 GPa	0.1 MPa$\sqrt{m}$
Cancellous frozen	++	+	No	Mid	4 MPa	1 GPa	0.1 MPa$\sqrt{m}$
Cancellous γ-irradiated	No	+	No	Low	3 MPa	0.9 GPa	-
Natural Biomaterials							
DBM[a]	++	+	No	Low	N/A	N/A	N/A
Collagen	No	++	No	No	N/A	N/A	N/A
Coralline hydroxyapatite	No	+	No	No	9 MPa	7.9 GPa	1.0 MPa$\sqrt{m}$
Synthetic Biomaterials							
Porous ceramics (TCP[b], HA[c])	No	+	No	No	2-8 MPa	0.5-4 GPa	1.0 MPa$\sqrt{m}$
Bioglass	No	++	No	No	42-103 MPa	5-35 GPa	0.6-1.2 MPa$\sqrt{m}$
Porous Polymers (PLLA[d], PGA[e])	No	+	No	No	2 MPa	0.2 GPa	-
Calcium phosphate cement	No	+	No	No	4 MPa	3 GPa	-
PMMA[f] cement	No	+	No	No	90 MPa	2.4 GPa	1.7 MPa$\sqrt{m}$
Glass Ionomer	No	+	No	No	180 MPa	4-10 GPa	1.2 MPa$\sqrt{m}$

---

[a] Demineralized Bone Matrix
[b] TriCalcium Phosphate
[c] HydroxyApatite
[d] Poly-L-lactic acid
[e] Polyglycolic acid
[f] Polymethyl methacrylate

artificial bone material needs to be further studied before these novel grafting solutions may be used in surgery. A synthesized review of the different bone graftings used in surgery are presented in table 2.1 from review articles [15, 44, 59, 124, 138].

One of the promising approaches consists of combining an artificial bioresorptive porous material with bone cells. Such *constructs* are complex biomechanical systems that must be optimized before they can be used in surgery. Indeed, appropriate chemical and/or mechanical stimulation of the bone cell may provide the osteoinductive and osteogenesis properties of the graft (see chapters 3 and 4). Finally, the mechanical properties of the skeleton may be tuned to favor a rapid osteointegration. This particular point is the subject of the following sections.

2.2 Biomechanical Model

The osteointegration isn't determined solely by the intrinsic characteristics of the graft material. Osteointegration is a complex mechanism that involves biological processes such as angiogenesis, transport of nutriment, waste, biochemical signals and cells. From a macroscopic point of view, the bone formation at the interface which ensures the osteointegration of the graft, may be related to the micromotions between the implant and the existing bone and shear strain near the interface. Experimental studies [85, 139, 171–173] have demonstrated that micromotion of more than 100 μm triggers formation of fibrous tissue instead of mineralized bone. Therefore, the osteointegration of a graft is related to its mechanical environment and to its mechanical properties. However, it is impossible to draw general guidelines concerning osteointegration. Each clinical intervention using bone graft must be studied to determine the best graft physical properties.

The case of open wedge tibial osteotomy is interesting as the mechanical loads applied on the bone graft are important. Therefore, the biomechanics may play an important role and clear clinical guidelines may be proposed regarding the bone graft mechanical properties, size and location for the best possible osteointegration. Using the commercial software ABAQUS/Standard 6.2-1 (HKS Inc., Newpark, USA), a mathematical model based on the finite element method (FEM) was built to numerically investigate open wedge tibial osteotomy.

2.2.1 Method

First, the external contour of a tibia from a 35 year old male patient without apparent pathology was reconstructed from Computed Tomography *(CT)* images (see Figure 2.7). It was assumed that the tibia of a patient with varus deformation had a similar spatial bone density distribution to a healthy knee. A satisfactory density representation of the tibia was achieved with CT scans taken every 700 μm with a resolution of 512x512 pixels per slide and a pixel size of 390 μm. The 3D geometry reconstruction of the cortical and cancellous bone volumes were generated by AMIRA software (Konrad-Zuse-Zentrum für Informatik Berlin, Germany) using a semi-automatic algorithm based on the pixel's Hounsfield unit (see Figure 2.7 A). It was estimated that such a procedure was able to reconstruct the exact bone geometry within an error margin of 2 pixels, i.e. 0.78 mm [20].

Second, the 3D cortical and cancellous bone contours were transferred to the PATRAN software (MacNeal-Schwendler, South Coast Metro, California, USA) that generated a mesh of first order hexahedral elements (C3D8 elements). Thorough attention was paid in obtaining at least two elements through the cortical bone depth. Consequently, a good numerical representation of the density step between cancellous and cortical bone [160] was achieved.

Then, the osteotomy was performed on the computer under the supervision of a senior orthopedic surgeon and a correction angle of 10° was applied. At this stage, several wedge geometries and positions could be tested - a detailed discussion on the effect of the wedge geometry, position and mechanical characteristics are discussed in sections 2.4 to 2.5. All wedges tested were assumed to be uniformly in contact with the remaining bone at their upper and lower interfaces. These interfaces were modeled by contact surfaces that allowed separation and friction. The tangential friction law was based on Coulomb's criterion for delimiting adherence from friction and a non-associated slip rule governed the slip velocity.

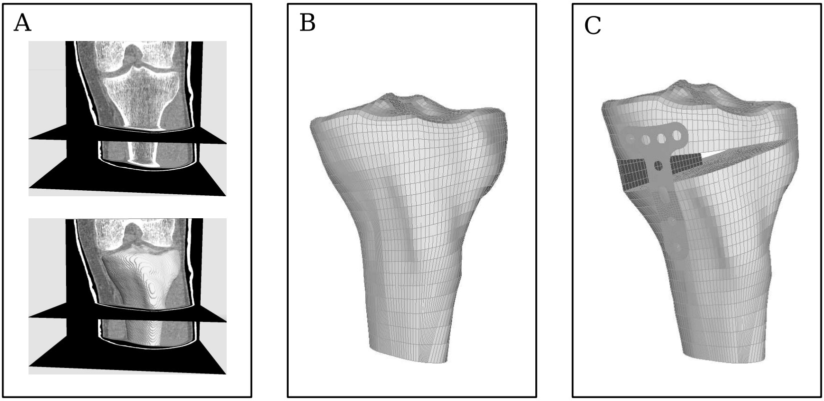

Figure 2.7: (A) The 3D geometry is first reconstructed from CT images. (B) The cortical and cancellous bone are then discretized into finite elements. (C) The osteotomy is carried out on the finite element model.

Finally, the supporting plate was reconstructed geometrically from a standard stainless steel T-plate (Synthes, Soloturn, Switzerland), and modeled by quadrilateral shell elements (S4R5). It was tightened to the tibial head by four titanium M4x55 screws, which were modeled by beam elements (B31). In order to model the load transfer at the interface between the screw and the bone, multipoint elements (LINEA) were used to connect each node of the screw (beam elements) to the neighboring nodes of the bone located within a disc of 4mm diameter. Thus, the bending and axial stiffness of the screws were modeled accurately. The connection of the screw head to the T-plate was similarly achieved. The leg of the T-plate was fixed to the main tibia part by two screws which were modeled identically to the screws fixing the T-plate to the tibia head.

The whole osteotomy model was composed of 98 beam elements (B31), 676 shell elements (S4R5) and 25496 volume elements (C3D8).

2.2.2 Material Properties

The constitutive laws for both cortical and cancellous bones were assumed to be linear elastic, inhomogeneous and to exhibit transverse isotropic properties with the principle direction along the bone axis. This was found to be a reasonable assumption [148, 160, 198]. Inhomogeneity of bone was taken into account by considering a quadratic relation between elastic moduli, shear modulus and apparent density [109, 154]. The apparent bone density was obtained by the CT images and assigned to the nodes of the finite elements using a program developed by Dr. Terrier [185]. Finally, the elastic constants were taken from the literature [42, 152].

The friction coefficient between the wedge and the tibia was assumed to be similar to the one observed at a bone-bone contact. Van Frauenhofer et al. [82, 167] have quantified the translational and the rotational friction coefficient between two bony structures to be between 0.5 and 0.7.

The T-plate material was assumed to be linearly elastic, homogeneous and isotropic. The T-plate was made of surgical stainless steel (AISI 316L) which has an elastic modulus of 200 GPa and Poisson ratio of 0.3.

2.2.3 Loading and Boundary Conditions

The loading occurred in two steps corresponding to *(i)* the surgical intervention induced-loads and *(ii)* physiological loads taking place after surgery (see Figure 2.8). First, the tibia was opened with a correction angle of 10°, corresponding to the mean correction angle [41,66]. The wedge was placed in-between the tibia parts. The opening of the tibia induced the elongation of the remaining intact cortex, medial collateral, patellar ligaments and the muscles having an insertion *distal* to the osteotomy[6]. The mechanical loads resulting from the opening of the tibia exterted a jaw force on the wedge and maintained it in position. The knee pre-tension due to muscle tonus was modeled as a femorotibial contact force of 400 N [183]. Finally, a dedicated finite element model was created to evaluate the periosteum elongation loads which is described in section 2.2.4.

Once the T-plate was screwed, the osteotomized tibia was loaded by postoperative physiological loads. The maximal gait load was applied to the operated knee, bearing in mind that this load case was very limiting for the open wedge tibial osteotomy. In fact, the first knee postoperative movement is passive flexion and then crutches are prescribed to the patient. However, maximal gait load might be present in the early recovery phase and must therefore be taken into account as the worst loading case.

The precise moment of the gait where the muscle activity and joint contact loading are maximal takes place just before *toe off* and at the second peak in ground reaction forces (45% of the whole gait cycle) [50]. *In vivo* measurements of the tibial strains demonstrate that the maximal strains did in fact occur between *heel off* and *toe off* phase [103]. At this instant, the total femorotibial contact force was measured *in vivo* to be 3.5 times the body weight (BW)

---

[6] The muscles that are compressing the osteotomy are all muscles active in the gait except the semimembranosus, semitendinosus and pes anserinus expansion that have insertions proximal to the osteotomy.

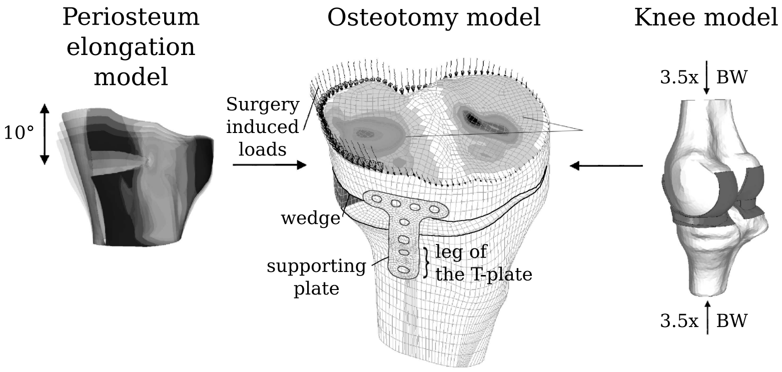
Periosteum elongation model
10°
Osteotomy model
Surgery induced loads
wedge
supporting plate
leg of the T-plate
Knee model
3.5x BW
3.5x BW

Figure 2.8: Medial open wedge tibial osteotomy finite element model: The loads due to the elongation of the periosteum after the opening the tibia were evaluated with a simplified periosteum elongation model (left) and applied to the osteotomy model (middle). The maximal gait loads were calculated with an entire knee model (right) and then applied to the osteotomy model (middle).

[79,183] and to occur at a knee flexion angle between 0 and 7%. Therefore, this load and flexion angle were assumed to be the most limiting for the tibia and were taken as the loading worst case situation in the computations.

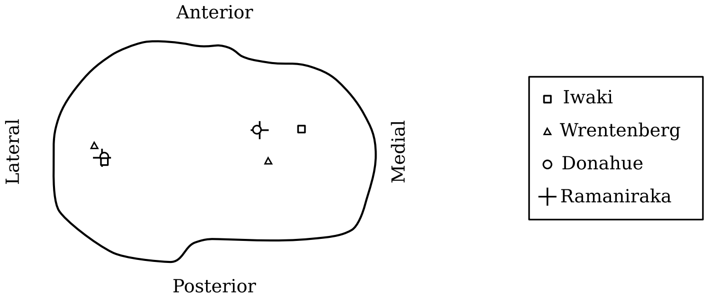

Figure 2.9: Comparison of the femorotibial contact points obtained by Iwaki *et al.* [81], Wretenberg *et al.* [199], Donahue *et al.* [48] and Ramaniraka *et al.* [149]

The femorotibial contact load distribution was obtained from a FE model of the knee (see Figure 2.8) developed by Ramaniraka et al. [149]. It was assumed that a normal physiological load repartition of 40/60% was achieved between the lateral and medial plateau. The computed locations of the maximal contact stress on the tibial plateau were similar to those reported in the literature [48,69,199] (see Figure 2.9). Finally, the transposition of the femorotibial contact pressure from the complete knee model to the osteotomy model was carried out relative to the tibial plateau intrinsic coordinate system [142].

2.2.4 Periosteum Elongation Model

This model was built to obtain an estimate of the jaw forces induced by the opening sequence of the osteotomy. The jaw forces are mainly due to the elongation of the remaining intact cortex, medial collateral and patellar ligaments which exert a stabilizing compression force on the wedge [100]. The contribution of muscle elongation to the jaw force was neglected because the ratio of the elongation length to the whole muscle length was small for most muscles that have a tibial insertion distal to the osteotomy.

The external contour of the tibia was reconstructed from CT images. The periosteum was assumed perfectly dissociated from the tibia (no friction) along a given height and on the entire circumference. The height corresponded to the length of the vertical incision carried out by the surgeon, along which the cortex was detached from the bone with a chisel. A second incision was performed horizontally on the anteromedial side of the tibia corresponding to the opening that the surgeon performed for sawing the bone. These incisions were modeled by free boundaries.

The jaw force was computed assuming that the periosteum had a constant thickness of 0.3 mm. It was considered as homogeneous and linearly elastic. As the mechanical properties of soft tissue vary significantly between individuals [62, 141], averaged values found in the literature were used [143, 191]. The tensile modulus was set to 80 MPa and Poisson ratio to 0.495.

To model the opening of the osteotomy, the element nodes of the periosteum upper boundary were rotated 10° around the bone hinge formed by the remaining cortical bone at osteotomy level. The nodes of the lower boundary were fixed in translation. The entire model was composed of 2036 shell elements (S4R5).

A total force of 486 N was exerted by the elongated cortex. This load was not continuously distributed along the tibia circumference. Stronger closing loads were observed on the posterior side than on the anterior side of the tibia. The order of magnitude of the jaw loads was confirmed experimentally on a cadaveric lower limb (see section 2.2.5). The calculated forces due to periosteum elongation were then applied on the osteotomy global model (see Figure 2.8).

2.2.5 Experimental Determination of the Maximal Jaw Force

A cadaveric lower limb was operated on by a senior surgeon, reproducing the osteotomy performed on patient suffering from varus deformation. The tibia was opened with a spreader forceps designed and manufactured at EPFL that was mounted with a force sensor for the measurement of the total jaw force (see Figure 2.10). The distraction force was applied by the means of a hoist until reaching a distance between the distal and proximal bone parts of 15 mm. The spreader forceps was fixed in this position and the total jaw force was measured for 30 minutes. A total jaw force of 330 N was measured at the initial time of distraction that relaxed at a rate of 0.73 N/min (see Figure 2.11).

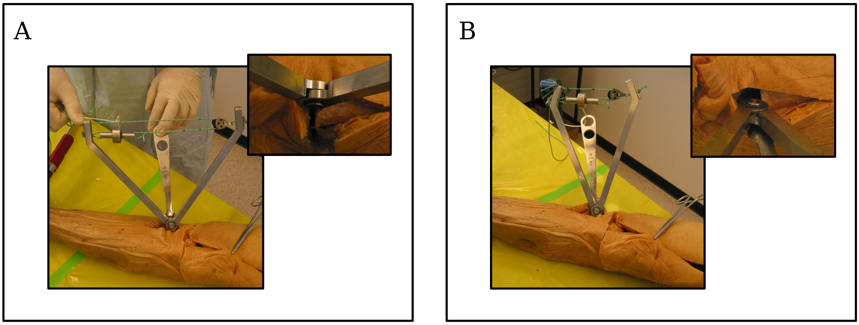

Figure 2.10: The custom spreader forceps was (A) first put in position, (B) then a distraction force was applied by means of a hoist to achieve an opening distance of 15 mm.

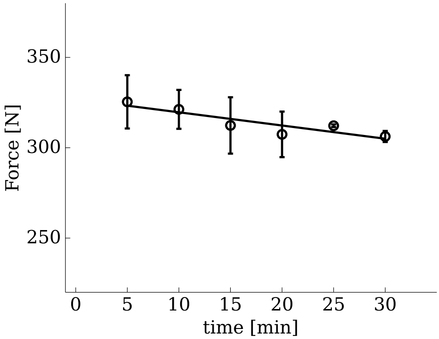

Figure 2.11: Jaw force relaxation during 30 minutes post distraction. Three measurements were carried out at each time point and the mean value ± standard deviation was plotted.

The measured jaw force (330 N) is similar to the total force computed with the numerical model (486 N). Consequently, It may be concluded that our numerical model is an acceptable estimation of the jaw force due to the elongation of the remaining soft tissues.

2.2.6 Effects of Friction Coefficient

The friction coefficient between the wedge and the bone is likely to vary between 0.5 and 0.7 [82, 167] which might impact the numerical results. However, the friction coefficient variation was found to have a negative effect on the stresses and micromotion magnitudes.

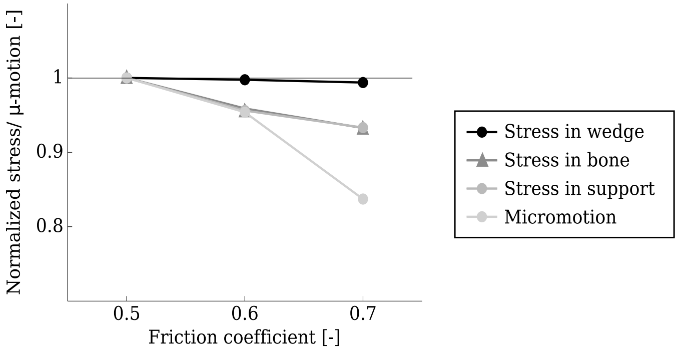

Figure 2.12: Impact of the interface friction coefficient on the maximal stresses and maximal micromotion.

First, an increase of the friction coefficient was found to reduce the tibial head deflection which reduced the maximal stress in the wedge, bone and supporting plate. The physical explanation is that the greater the friction between the wedge and the bone gets, the smaller the sliding distance between the tibial head and the wedge is. As a result, the vertical deflection due to bending of the tibial head is reduced with increasing friction coefficient because the lateral movement of the tibial head relatively to the wedge is increasingly restrained. In other words, the friction between the bone and the wedge restrains one degree of freedom of the tibial head (sliding) which reduces its vertical bending deflection. The reduced tibial head deflection induces smaller maximal stresses in wedge, supporting plate and bone. An increase of the bone/bone and bone/wedge friction coefficient from 0.5 to 0.7 yielded a decrease of the maximal stresses in the supporting plate, bone and wedge of more than 7% (see figure 2.12).

In addition, an increase of the friction coefficient from 0.5 to 0.7 resulted in 19% decrease of the maximal micromotion which is obviously due to a higher resistance against sliding movment (see Figure 2.12). Erring on the side of caution, all the computations presented in the following sections were done with a friction coefficient of 0.5.

2.3 Effects of the Supporting Plate Position

At the beginning of the tibial osteotomy surgery no internal fixation or plaster was used for maintaining the position of the wedge [67]. It was thought that the wedge would be held in place by compressive forces due to elongation of the surrounding soft tissues. But displacement of the wedge with loss of correction was observed [67]. To overcome this complication, an internal fixation composed of a plate and screws was suggested. This practice has spread, and recent clinical studies on open wedge varus osteotomy all report the use of internal or external fixation at least during 4 months postoperatively [6, 66, 100, 174].

Most clinical studies don't propose a specific positioning of the fixation and wedge [66, 100, 174]. Moreover, no comparison between different layouts was found in any of these studies, nor in finite element investigations [164, 165]. But from a biomechanical viewpoint, the spatial distribution of the structural elements composing the osteotomy (wedge, plate, bone) plays a key role. Indeed, these elements ensure the structural stability of the osteotomy. Their relative positions with respect to the applied loads may have an important impact on the stress distribution and micromotion magnitude at the bone-wedge interface. To maximize the graft osteointegration, the load path must be optimized to minimize micromotions at the bone-wedge interface.

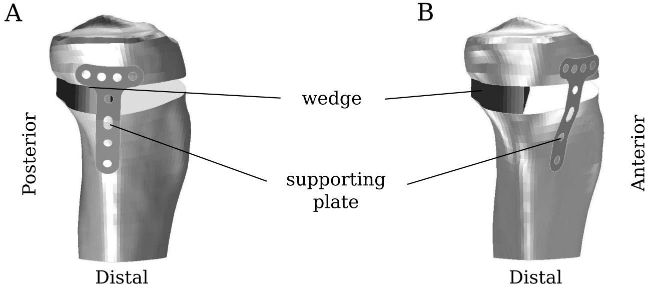

Figure 2.13: View from the medial side of the open wedge tibial osteotomy model with (A) a plate in a medial position and (B) in an anteromedial position.

To assess the impact of the supporting plate position on open wedge tibial osteotomy, two configurations were studied. The first configuration had a supporting plate positioned on the medial axis, and the second one had a supporting plate positioned at half distance between the medial and anterior axis (see Figure 2.13). Both configurations had a wedge that covered one fourth of the osteotomy section and that was placed in a posteromedial position. Its bulk stiffness was assumed to be 3 GPa, which is equivalent to a wedge made of acrylic bone cement (see section 2.5 for the wedge stiffness effects). The stresses and strains in the plate, screws, bone and wedge as well as the micromotions between the wedge and bone were computed. The results obtained are discussed in the following sections.

2.3.1 Micromotions

The computed maximal micromotion at the bone/wedge interfaces increased with increasing load. This tendency was more pronounced when the supporting plate was positioned medially rather than anteromedially (see Figure 2.14). At maximal gait load the maximal micromotion computed in the case of a medial plate position was 1.71 times larger than a configuration with an anteromedial plate (1230 μm and 720 μm respectively). In addition, the critical micromotion magnitude of 100 μm above which fibrous tissue formation is induced [20,85,139,171–173] was exceeded for knee loads above 50 kg for an anteromedial plate position and 30 kg for medial plates. This indicated that anteromedial plate position may be less likely to induce fibrous bone formation than a medial plate position.

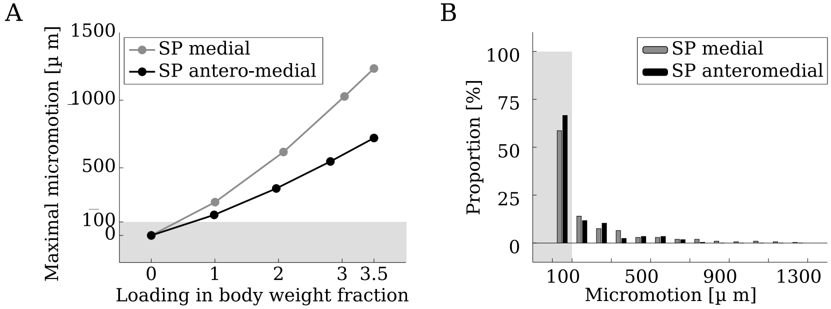

Figure 2.14: (A) The maximal micromotions computed at the interface between bone and wedge as a function of the knee loading for two different supporting plate (SP) positions. (B) The micromotion distribution computed at the wedge/bone interface for maximal gait load in terms of relative wedge/bone contact area that is subject to micromotion within a given interval. The range of micromotion for which a good osteointegration is likely to occur is highlighted in gray.

Although small micromotion magnitudes were computed to take place on the majority of the wedge/bone contact area (see Figure 2.14 B), 33% (anteromedial plate) to 41% (medial plate) of the contact surface moved more than 100 μm.

2.3.2 Stresses

The computed stresses at maximal gait load indicated that an anteromedial supporting plate was more efficient than a medial plate for the open wedge tibial osteotomy. Indeed, larger maximal stresses were observed in the wedge, in the supporting plate and the screws as well as in the host bone when the supporting plate was placed in medial position rather than in anteromedial position.

At maximal gait load (3.5 body weight), the maximal von Mises stress in the bone was 3.4 times higher in a medial plate configuration than in an anteromedial configuration, with magnitudes of 260 MPa and 77 MPa respectively. In the wedge, a factor of 1.4 was found between osteotomy with the plate in a medial position ($\sigma_{\max} = 180$ MPa) and the osteotomy with the plate in an anteromedial position ($\sigma_{\max} = 130$ MPa). Finally, a decrease of the maximal stress in the supporting plate by a factor of 1.4 and in the screws by a factor of 1.1 were observed between a medial plate position (supporting plate $\sigma_{\max} = 2100$ MPa; screws $\sigma_{\max} = 120$ MPa) and an anteromedial plate position (supporting plate $\sigma_{\max} = 1500$ MPa; screws $\sigma_{\max} = 110$ MPa).

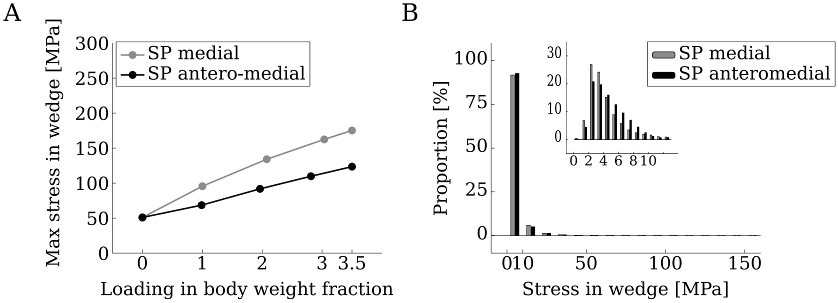

Figure 2.15: (A) Maximal von Mises stresses computed in the wedge as a function of the loading for two different supporting plate (SP) positions. (B) The stress distribution computed in the wedge at the maximal gait load in terms of the relative wedge volumes that are subject to stresses within a given interval.

Although the stresses computed on a majority of wedge nodes were below 10 MPa (see Figure 2.15), the maximal stresses reported in the previous paragraph are representative of the assembly safety. Indeed, these local high stresses may initiate material failure which then propagates inside the material due to subsequent load application. The material failure may then reach the low loaded regions and lead to the failure of the whole part. This process is dependent on the material properties and on the loading spectra. However, it is known that higher local stresses applied on the same material and at the same frequency shorten the mechanical life of the part more than lower local stresses. As a result, the wedge, supporting plate, screws and bone are more likely to have a longer mechanical life when the supporting plate is placed in an anteromedial position rather than in a medial position.

2.3.3 Conclusions

The stresses in the bone, wedge, supporting plate and screws as well as the micromotions at the bone/wedge interface indicated that an anteromedial supporting plate position is more favorable than a medial plate position. However, maximal stresses and micromotion magnitudes computed at maximal gait load were above critical values for material integrity and mineralized bone ingrowth at the interface. Consequently, erring on the side of caution, it is proposed that partial loading shall be prescribed postoperatively so that the maximal micromotion magnitude stays below the critical value. In concrete terms, the use by the patient of crutches during the first six post operative weeks, which corresponds to current clinical practice [117], may limit the load applied to the knee below 50 kg (19% of the maximal gait load). In this case, the micromotion magnitude computed for an open wedge osteotomy with an anteromedial supporting plate are below 100 μm. In addition, the margin of safety[7] computed for the bone, supporting plate and screws were all positive and larger when the supporting plate was placed in an anteromedial position rather than in a medial position. In summary, an anteromedial plate position presented larger safety against mechanical failure of the bone, plate and screws and might present better and quicker wedge osteointegration than an open wedge tibial osteotomy with a medial supporting plate position.

2.4 Effects of Wedge Geometry

The wedge geometry is of small concern when autologous bone is used for open wedge tibial osteotomy. Indeed, in this case, the geometry of the wedge is mostly defined by the available bone at the donor site and is limited to, at most, a few cubic centimeters. On the other hand, when allografts and synthetic bone grafts are used, the wedge size is not limited by its availability. Therefore, different wedge sizes and geometries may be envisaged to optimize the biomechanics of open wedge tibial osteotomy, bearing in mind the economic and practical implications.

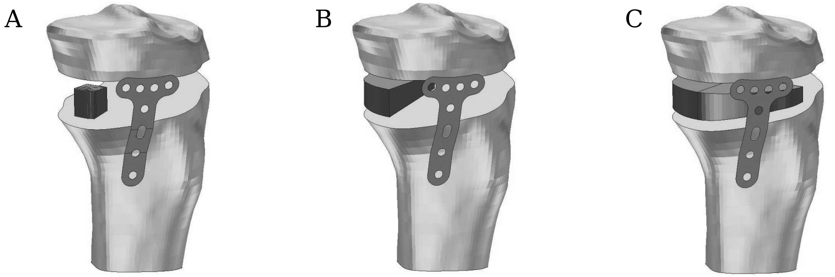

Figure 2.16: Expanded view of the three wedge sizes studied (additional spacing was added between the bone and the wedge for visualization purpose): (A) a cubic wedge of 1 cm edge length; (B) a wedge covering the posteromedial quarter of the osteotomy cross section; (C) a wedge covering the medial half of the osteotomy cross section.

To study the impact of wedge geometry on open wedge tibial osteotomy biomechanics, three different wedge sizes were considered (see Figure 2.16). First, a cube of about 1 cm edge length with a bulk volume of 1.3 cm^3 was placed in a medial position. Second, a wedge covering one quarter of the total osteotomy cross section with a total bulk volume of 7.2 cm^3 was placed in posteromedial position. Third, a wedge covering the medial half of the osteotomy cross section with a bulk volume of 14 cm^3 was considered. All three wedges were assumed to be made of the same elastic material with 0.5 GPa bulk modulus (for a review of the wedge stiffness effect, see section 2.5). Finally, based on the results of the supporting plate position study, a favorable anteromedial plate position was assumed (see section 2.3).

---

[7] The margin of safety is used in engineering to quantify the percentage of capability over the requirements that a structure has. It is given by $MS = \frac{S}{S_{max}} - 1$, where S is the physical parameter current state and S_{max} is its maximal admissible value.

2.4.1 Micromotions

The maximal micromotions computed at the interface between the bone and a quarter wedge were similar in magnitude to those computed for a wedge covering the half osteotomy cross section. In both cases, the micromotions were linearly dependent on the loading intensity. The maximal micromotion magnitudes exceeded the critical value of 100 μm at about 0.5 times the body weight (see Figure 2.17 A). In contrast to the large wedge, the cubic wedge of 1 cubic centimeter exhibited low maximal micromotions magnitude and the critical value was exceeded only at knee loading larger than two times the body weight. In addition, the maximal micromotion magnitude did not appear to be linearly related to the compression load applied to the knee.

This dissimilar behavior between large wedges and the smaller one was confirmed by the distribution of micromotion magnitude (see Figure 2.17 B). On one hand, 90% of the micromotions computed between a wedge of 1 cm edge length were smaller than 100 μm at maximal gait load. On the other hand, this proportion fell to about 69% for both larger wedges.

The dichotomy between large and small wedges regarding the micromotion magnitude was explained by the local deformation of the neighboring bone. Indeed, all the forces supported by the 1 cm edge length wedge were applied on a small bone area, inducing high contact pressures. It induced a local sinking of the bone that entrapped the wedge and prevented it moving sideways. The bone sinking was less pronounced on larger wedges as smaller contact pressures

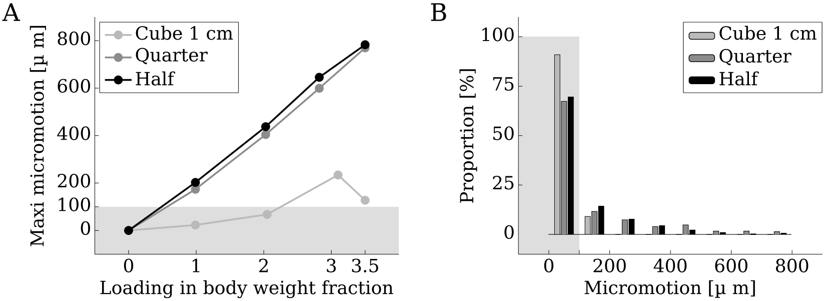

Figure 2.17: (A) The maximal micromotion at the interface between bone and wedge as a function of the knee loading for three different wedge size. (B) The micromotion distribution computed at the wedge/bone interface for maximal gait load in terms of relative wedge/bone contact area that is subject to micromotion within a given interval. The range of micromotions for which a good osteointegration is likely to occur is highlighted in gray.

were at work. In addition, lateral entrapment took place on one side of the wedge only which permitted the wedge to move in the opposite direction.

2.4.2 Stresses

Conversely to the micromotion magnitude, the maximal stress computed in a cubic wedge of 1 cm edge length was higher than those computed for larger wedges (see Figure 2.18 A). The maximal stress at maximal gait load was 1.8 times higher in a 1 cm edge length cube than in a quarter wedge, and 3.2 times higher than in a half wedge. In addition, the maximal von Mises stresses at maximal gait load in the bone and supporting plate were 1.7 and 1.5 times respectively higher in the small wedge than in the quarter wedge, and 2.1 and 2.8 times larger respectively than in the half wedge.

The overall stress level in the small wedge was also higher than that computed in the larger wedges. Indeed, 95% and 99% of the von Mises stresses computed in the quarter and half wedge respectively were below 10 MPa. This proportion fell to 23% for a cubic wedge (see Figure 2.18 B). In addition, the mean von Mises stress computed for a cubic wedge was 19 MPa when it was about 4 MPa and 2.7 MPa in a quarter wedge and a half wedgerespectively .

Bearing in mind that the mechanical strength of porous ceramics and polymer artificial grafts were reported to be between 2 and 8 MPa (see table 2.1), it is likely that a wedge of 1 cm edge length made of these material fails. Indeed, the averaged von Mises stress in a cubic wedge of 1 cm edge length due to muscle tonus and soft tissue elongation only was computed to be higher than the mechanical strength of these materials. However, the use of small wedge made of resistant material such as acrylic bone cement, bioglass or glass ionomer without any wedge failure may be possible and was reported in clinical studies (acrylic bone cement [5,52,66]).

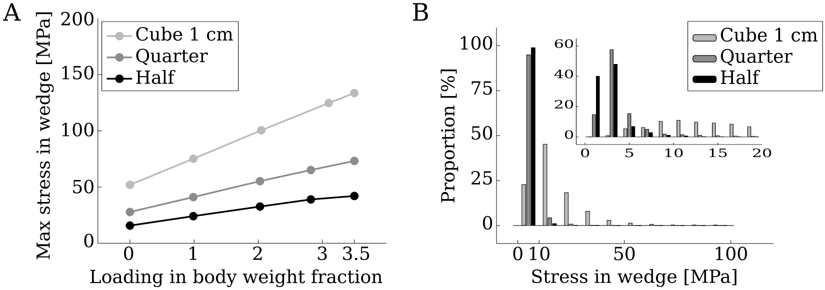

Figure 2.18: (A) Maximal von Mises stresses computed in three different wedge geometries as a function of the loading. (B) The stress distribution computed in the wedge at the maximal gait load in terms of the relative wedge volumes that are subject to stresses within a given interval.

2.4.3 Octahedral Strains

The choice of a small and mechanically resistant wedge may result in worse osteointegration than a larger wedge. Although micromotion magnitudes computed at the interface between a small wedge and bone were smaller than those computed for larger wedges, the overall bone stimulation was less favorable for bone ingrowth. Actually, the differentiation of the interfacial tissue is not only sensitive to micromotions [139, 171] but also to shear strain and hydrostatic strain [77, 144].

To take into account the multidirectional tissue loading and deformation near loaded interface, several mechanical parameters were identified [25–28, 77, 144]. One of these mechanical parameters that is applicable to our monophasic solid continuum model is the cyclic octahedral strain. Carter [27] proposed that high shear, characterized by octahedral strain or stress, encouraged fibrous tissue formation during fracture healing. In this study, correlating experimental data to numerical simulations enabled computing of a critical octahedral strain. Based on the experimental data of Jasty *et al.* [85], Büchler *et al.* [19] found an upper strain limit of 0.82% above which the mechanical environment favor the formation of fibrous tissue. A lower limit at 0.23% was computed, below which formation of mineralized bone is likely to take place. Therefore, the octahedral strains were computed for the different wedge geometries and compared to the above critical values. This procedure gave a better view of the wedge size effect on open wedge tibial osteotomy biomechanics.

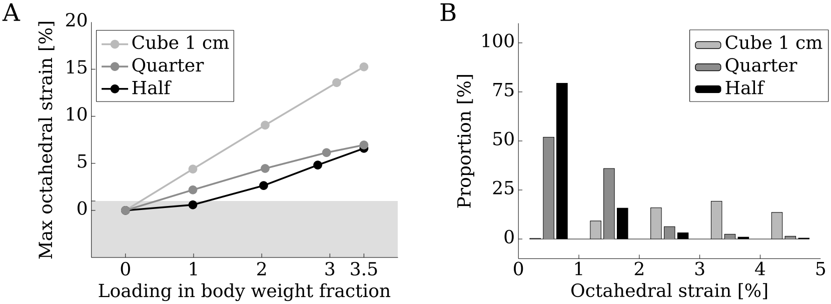

Figure 2.19: (A) Maximal octahedral strain computed in three different wedge geometries as a function of the knee loading. (B) The octahedral strain distribution computed in the wedge at the maximal gait load in terms of the relative wedge volumes that are subject to strains within a given interval.

The octahedral shear strains computed on the smaller wedge were much higher than those computed in the quarter and half wedges (see Figure 2.19 A) for all knee loadings. The octahedral strains' distribution in the wedges also revealed a higher level of shear strain in the small wedge than in larger one. At maximal gait load, most of the cubic wedge volume (98%) was sheared more than 1% (see Figure 2.19 B), whereas most of the quarter and half wedge volume were sheared less than 1%. In addition, this difference in shear strain level in most of the wedges' volume was also computed at partial knee loading. For instance, at a partial knee loading of 50 kg, most of the smallest wedge volume was sheared more than 1% whereas most of the quarter and half wedge volumes were sheared less than 0.5%. In addition, most of the micromotion computed between the half and quarter wedges respectively and the bone were lower than the critical value of 100 μm in this loading state. As a result, partial loading of the knee of less than 50 kg might promote the ingrowth of bone in the quarter and half wedge and at the bone/wedge interface. On the other hand and despite the small micromotion level computed between a cubic wedge and bone, fibrous tissue is likely to form at the wedge/bone interface as high shear strains were computed in most of the cubic wedge volume.

2.4.4 Economic and Handling Aspects

We have seen in the last section that large wedges may present better osteointegrative characteristics than a small cubic wedge. However, the bigger the wedge is, the more expensive it becomes. To evaluate the costs associated with a particular wedge size, I computed the average price of each wedge, based on prices of Tutoplast® Spongiosa Block, Tutoplast® tutobone (Tutogen Medical GmbH, Germany), ChronOs™ (Synthes, Switzerland) and Pro Osteon® (Biomet, Inc., USA). The average price associated with each wedge size was computed as

$$C = \frac{1}{4}\sum_{i=1}^{4}\frac{C_{graft,i}}{V_{graft,i}} \times V_{wedge} \ ,$$

where $C_{graft,i}$ are the 2006 prices of standard grafts made of i-th material, $V_{graft,i}$ are the graft volumes and V_{wedge} is the wedge bulk volume.

Table 2.2: Costs comparison between different wedge sizes.

cube 1 cm	quarter	half
150 €	650 €	1260 €

A cubic wedge of 1 cm edge length is indeed the cheapest solution, with an averaged price of about 150 €. However, it may not be the cheapest solution when the costs associated with the higher likelihood of complications are taken into account. As discussed in previous sections, a quarter wedge may undergo a better osteointegration than a small wedge and induced smaller stresses in bone. Therefore, a wedge size that covers one quarter of the osteotomy cross section seems to be the best compromise in term of likelihood of clinical success to price ratio. Indeed, its price (650 €) is competitive as it is lower than the costs associated with autograft (1000 €) and only slightly higher than the typical price for allografts (370 €-560 €). Finally, a quarter wedge may be handled easily by the surgeon during its installation, thanks to its relatively small size.

On the other hand, a wedge that covers half of the osteotomy cross section may be difficult to install as the available space is limited by surgical instrumentation and intact soft tissue (see Figure 2.20). In addition, the price of a large wedge that covers the half osteotomy cross section seems disproportionately high with regard to the associated clinical benefits. Indeed, small biomechanical differences were computed between a half and a quarter wedge (see figures 2.17 to 2.19), but the price was double (see table 2.2).

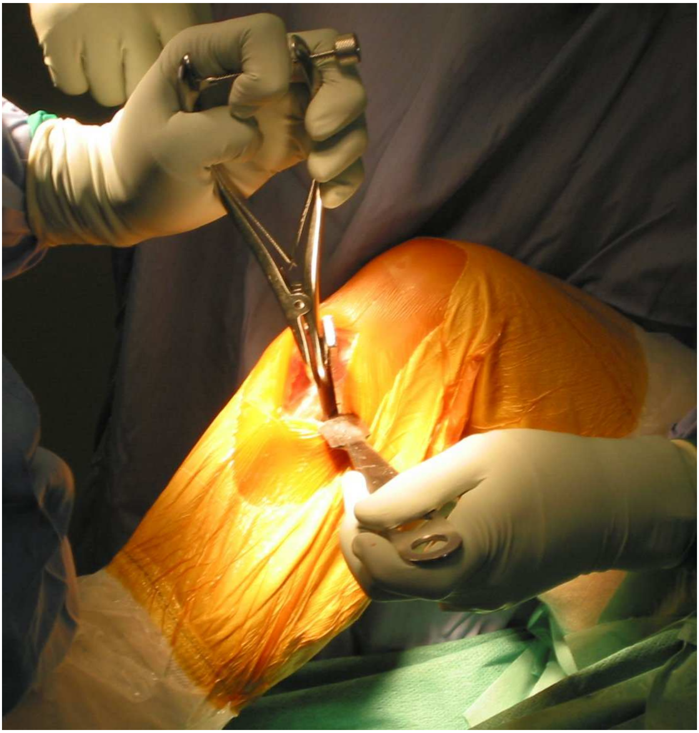

Figure 2.20: The free space available for the wedge implantation is limited by the surgical instruments necessary for maintaining the bone open.

2.4.5 Conclusions

Four parameters were identified as having an important role in the choice of the wedge size: micromotions, stresses, octahedral strain and costs. Each parameter was evaluated for three different wedge sizes and their comparison indicated that an intermediate wedge size might be the best compromise. Indeed, a wedge that covers one quarter of the posteromedial osteotomy cross section was the only wedge size that might simultaneously present good osteointegration and competitive price. Despite low price, a small cubic wedge might present mechanical failure and poor osteointegration. Conversely, a large wedge might present better osteointegration than smaller wedges but might be less easy to install. Finally, the largest wedge was associated with high costs which compromised its competitiveness.

2.5 Effects of Wedge Stiffness

As discussed at the beginning of this chapter, a large choice of wedge materials is at the surgeon's disposal. Beside disparate availability, costs and practical aspects, each of these materials has different mechanical properties. To optimize the osteointegration of the wedge, the impact of its mechanical properties on the osteotomy biomechanics should be assessed.

To do so, the stiffness of a wedge was varied from 0.1 GPa to 18 GPa, which correspond to the stiffness of a highly porous polymer bone substitute and the stiffness of cortical bone respectively. The supporting plate/wedge configuration chosen was based on the results obtained in the previous sections. The best configuration was found to be a wedge covering one quarter of the osteotomy cross section and placed in posteromedial position and a supporting plate positioned anteromedially. Again, the biomechanics of open wedge tibial osteotomy was studied at maximal gait load.

2.5.1 Micromotions

Interestingly, the micromotion magnitudes between the wedge and the bone were hardly impacted by the wedge stiffness (see Figure 2.21). A 180 time increase of the wedge stiffness induced a micromotion reduction of less than 18% at maximal gait load. The discrepancies in micromtotion magnitude were almost inexistent at low knee loads, with a maximal variation of 4% at two fold body weight. Looking at the distribution of micromotions at maximal gait load further confirmed that the effect of wedge stiffness on the micromotion magnitude was small.

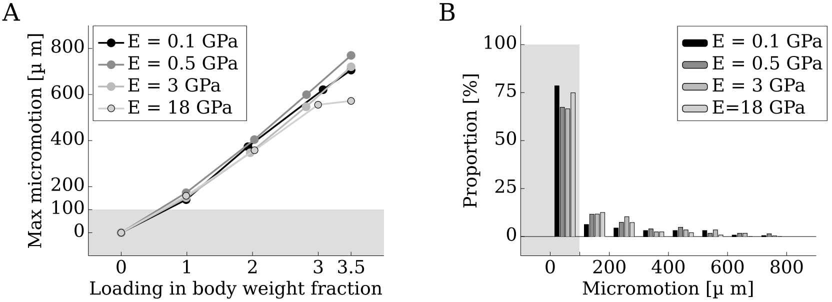

Figure 2.21: (A) The maximal micromotion at the interface between bone and wedge as a function of the knee loading for different wedge stiffness. (B) The micromotion distribution computed at the wedge/bone interface for maximal gait load in terms of relative wedge/bone contact area that is subject to micromotion within a given interval. The range of micromotion for which a good osteointegration is likely to occur is highlighted in gray.

At maximal gait load, more than 65% of the contact surface between the wedge and the bone moved less than 100 μm for all wedge stiffness between 0.1 and 18 GPa. This proportion increased with decreasing knee load, to reach 100% at 50 kg knee loading (0.65 body weight fraction) for all wedge stiffness.

2.5.2 Stresses

Conversely to micromotion, the maximal von Mises stresses computed on the wedge were significantly impacted by the wedge stiffness. As could be anticipated, the stiffer the wedge was, the higher the maximal von Mises stress (see Figure 2.22 A). At maximal gait load, the maximal stress in the wedge increased of 7.4-fold due to a change of the wedge stiffness from 0.1 GPa to 18 GPa. The same increase of wedge stiffness induced a 1.4-fold increase of maximal stress in the bone and a 1.2-fold decrease of the supporting plate maximal stress. However, the effect of the wedge stiffness on the global load splitting between bone, wedge and supporting plate was small. In fact, an increase of the wedge stiffness from 0.1 to 18 GPa induced an increase of the total load supported by the wedge of only 1.4% of the total knee load. As a result, it can be concluded that wedge stiffness had little impact on the global loading of the wedge, but impacted the local maximal stress magnitude.

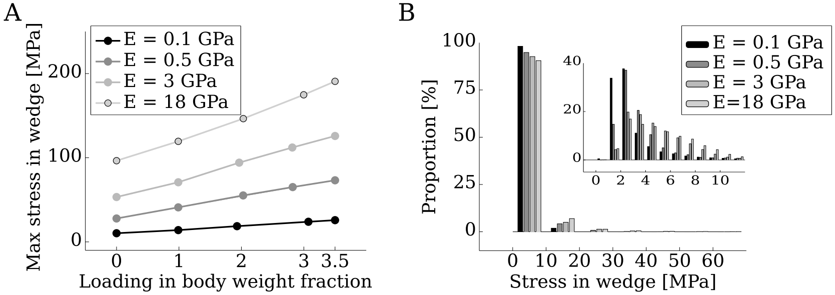

Figure 2.22: (A) Maximal von Mises stress computed in four different wedge stiffnesses as a function of the loading. (B) The stress distribution computed in the wedge at the maximal gait load in terms of the relative wedge volumes that are subject to stresses within a given interval.

The small impact of the wedge stiffness on the global wedge loading was further confirmed by the stress distribution as a large majority of the wedge volume was loaded under 10 MPa for all the tested wedge stiffnesses (see Figure 2.22 B). For instance, 98% of the most compliant (0.1 GPa) wedge volume was under 10 MPa against 90% for the stiffest wedge (18 GPa). As discussed in section 2.3, the maximal stress is important because it may initiate the material failure which then propagates during subsequent loading. Because a compliant wedge induced smaller local maximal stresses than a stiffer one, larger margins of safety against mechanical failure were computed for bone and wedge.

2.5.3 Octahedral Strains

We saw in section 2.5.1 that the wedge stiffness had little impact on the micromotion between the wedge and the bone. A partial knee loading of 50 kg limited the micromotion magnitude below the critical value of 100 μm. To favor bone ingrowth from the wedge/bone interface into the wedge, the shear strain in the wedge should be limited to below 0.83% [19].

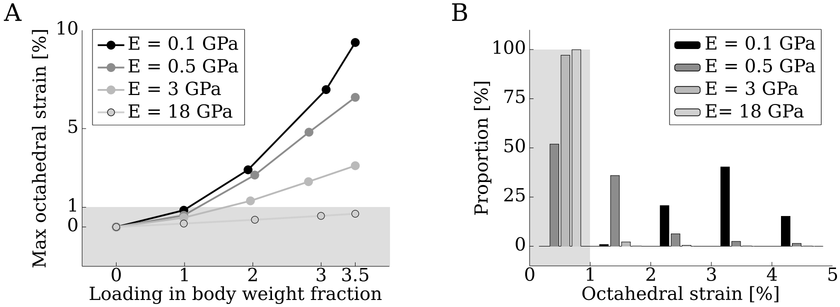

Figure 2.23: (A) Maximal octahedral strain computed in four different wedge stiffness as a function of the knee loading. (B) The octahedral strain distribution computed in the wedge at the maximal gait load in terms of the relative wedge volume that was subject to strains within a given interval. The range of micromotion for which a good osteointegration is likely to occur was highlighted in gray.

The octahedral shear strains were thus computed for wedges of different stiffnesses. As can be seen in Figure 2.23 A, the maximal shear strain in compliant wedges was much higher than in stiff wedges. Moreover, the proportion of volume that experienced shear strain larger than 0.83% at maximal gait load was also higher in compliant wedges than in stiff ones (see Figure 2.23 B). Actually, most of the volume of a wedge stiffer than 0.5 GPa was sheared lower than 0.83%. This indicated that such wedges may present good osteointegration. Conversely, a compliant wedge (0.1 GPa) deformed too much and might favor ingrowth inside its bulk volume of fibrous tissue.

2.5.4 Conclusions

Wedge stiffness largely impacted the local maximal stresses in bone and wedge. However, it had little effect on the global load splitting between the wedge, bone and supporting plate. In addition, very small variations in micromotion magnitudes were computed at the wedge/bone interface. On the other hand, the wedge stiffness impacted the magnitude of the maximal shear strain inside the wedge as well as the proportion of the wedge volume that experienced shear strain higher than 0.83%.

As a result, a compliant wedge of 0.1 GPa bulk elastic modulus induced moderate local stresses in the bone and wedge, but might favor the formation of fibrous tissue ingrowth. Conversely, a 18 GPa stiff wedge induced high local stresses but might favor the ingrowth of bone.

Therefore, an optimum wedge stiffness, with a margin of safety against wedge and bone failure, and that favor osteointegration would be between 0.5 and 3 GPa.

2.6 Discussion

In this chapter, I developed a biomechanical model of open wedge tibial osteotomy to test *in silico* the effects of supporting plate position, wedge size and wedge stiffness. The goal was to find an optimized configuration with regard to the graft osteointegration and mechanical resistance.

The supporting plate was placed in two different locations to study its effect on the stresses and micromotions at the implant/bone interface. In all structural components of the osteotomy, i.e. the bone, wedge, supporting plate and screws, the computed von Mises stresses were higher when the supporting plate was placed in a medial position rather than in an anteromedial position. The micromotions computed at the wedge/bone interface were higher when the plate was placed medially rather than anteromedially. Accordingly, the anteromedial plate position, which corresponds to current clinical practice [66, 67, 174], might present higher mechanical safety and better graft osteointegration than a medial plate position.

The effect of wedge size on osteotomy biomechanics and economy was studied. It was found that the best compromise in term of wedge size would be a wedge that covers the posteromedial quarter of the osteotomy cross section. Such wedge size was shown to present moderate local and global stresses, moderate micromotions and shear strains as well as a competitive price. Indeed, a small wedge of 1 cubic centimeter was shown to induce high stresses and strains in the bone and wedge itself. Although it was the cheapest solution, such a small wedge placed medially was shown to present low mechanical safety against failure and poor wedge osteointegration. On the other hand, a large wedge covering the medial half of osteotomy cross section was considered to be too expensive. The small biomechanical improvements in comparison to a quarter wedge were largely outweighted by a doubling of the costs associated with the wedge alone. In addition, the surgeon might have more difficulties installing a half wedge than a quarter wedge.

The wedge stiffness was varied to study its effect on the osteotomy biomechanics. Based on the previous two studies on wedge size and plate position, the most favorable configuration was taken, i.e. a quarter wedge placed posteromedially with an anteromedial supporting plate position. It was shown that in such a configuration, a wedge stiffness between 0.5 and 3 GPa might favor a rapid graft osteointegration and provide sufficient mechanical safety against failure of the bone as well as the wedge.

On one hand, wedge stiffness corresponding to the stiffness of cortical bone (18 GPa) was shown to induce high local stress on bone and wedge. A 2.6-fold local maximal stress increase due to a wedge stiffness increase from 0.5 GPa to 18 GPa was computed in the wedge and a 1.5-fold increase in the bone. The high local stresses induced by a stiff wedge might initiate bone and wedge failure which then might propagate during subsequent knee loading. In surgery, two frequent complications due to an open wedge tibial osteotomy using allograft were the loss of correction (22% of the complication) and undisplaced fracture of the tibial head (11% of the complications) [41, 67]. It is tempting to speculate that the local high stresses computed in the wedge and bone increased the likelihood of wedge settlement leading to loss of correction and initiation of tibial plateau fracture. The use of a more compliant wedge should reduce the occurrence of these complications, which was actually observed in one clinical study which used wedges made of acrylic bone cement [66]. In such a configuration, the maximal local stresses computed in the acrylic bone cement - that has an elastic bulk modulus of about 3 GPa [63] - were 1.6-fold smaller than in a bicortical wedge.

On the other hand, a wedge stiffness of 0.1 GPa might present poor graft osteointegration. Indeed, most of the graft volume was sheared more than the critical value above which fibrous tissue might form at partial knee loading corresponding to 20% of the maximal gait load. Therefore, the use of crutches during the first six postoperative weeks which corresponds to the current clinical practice [117] may not be sufficient to prevent fibrous tissue ingrowth when too compliant grafts are used.

The computations presented in this chapter were possible thanks to some assumptions. The maximal gait load was assumed to be the most constraining load that was exerted on the operated tibia during the first postoperative weeks. Indeed, Lanyon *et al.* [103] measured maximal strains in the tibia during this phase which also corresponds to high muscles activity [192]. All muscles that are active at maximal gait load have a tibial insertion distal to the osteotomy (the semimembranosus muscle has a proximal insertion but is inactive at 45% gait cycle). As a result, the whole 3.5 body weight loading passed through the osteotomy elements.

The loads induced by the surgical intervention were approximated by a linear elastic model of the periosteum. The numerical model gave a rough estimate of the loads due to the elongation of the periosteum as it did not take into account viscoelastic behavior of soft tissues [64,96,163] nor damage due to high applied strains [143]. However, the computed jaw force was of the same order of magnitude as the force necessary to maintain open an osteotomized cadaveric lower limb.

It should be remembered that these jaw forces have little impact on the micromotion magnitudes and cyclic strains as their magnitudes were computed relative to the preloaded state due to soft tissues elongation. The stresses computed in the supporting plate were also not affected as it was introduced after the application of the soft tissue preload. Only the total stresses and strains in the wedge and bone were directly impacted by these assumptions which should be viewed as an additional safety margin against their mechanical failure.

Finally, it was assumed that the muscle and ligament insertions weren't located at their exact positions. The whole tibia cross section was blocked at the tibia diaphysis. The muscles that are active at maximal gait load (quadriceps femoris, iliotibial tract I and II) have their principal force direction along the tibial axis [16, 17, 50] which permitted translation of their insertion along this direction. The local bone deformation due to the local application of muscle forces played little role on the stress distribution computed on the wedge, supporting plate and on the bone near the osteotomy.

Although beyond the scope of this work, the experimental validation of the stress analysis may be envisaged by performing loading tests on a cadaveric model of the open wedge tibial osteotomy. The theoretical stresses at the wedge/bone interface could then be compared with those measured using pressure sensitive films [3]. Fatigue tests could also be envisaged to identify the configuration with the longest life time and thus minimizing mechanical stresses. Finally, *in vivo* experiments on animals may lead to erroneous results as the mechanical environment and geometrical configuration of the open wedge osteotomy on human tibia may be difficult to reproduce.

2.7 Conclusions

Although autologous bone grafting comes with major complications, it is still today's most commonly used bone grafting procedure. The reason is simply that no competitive alternative is available. Lack of mechanical properties, poor osteoinduction and non-existent osteogenesis are the principal drawbacks of its competitors.

Bone tissue engineered grafts are promising solutions that might present better clinical scores than autografts in the near future. To achieve this goal, artificial bone grafts must have good *(i)* osteointegration, *(ii)* osteoconduction, *(iii)* osteoinduction and *(iv)* osteogenesis properties. All four requirements are dependent on bone biology and have a close relationship with bone and graft mechanical environment. Therefore, a detailed understanding of the mechanical environment is crucial for the development of a competitive bone substitute.

Each surgical intervention involving bone graft is associated with a particular mechanical environment. An optimized grafting procedure requires particular graft physical characteristics. At large scale, the mechanical properties of the graft play an important role in its osteointegration. In the particular case of open wedge tibial osteotomy, a graft covering one fourth of the osteotomy section appeared to be the best compromise. Based on the results obtained from numerical simulation, the graft stiffness had little influence on the micromotions at the graft/bone interface. However, stiff grafts induced high local stress in the neighboring bone and in the graft itself. Conversely, compliant wedges were subject to high shear strain which favors the ingrowth of fibrous tissue. Therefore, a graft of moderate stiffness between 0.5 and 3 GPa appeared to be the best compromise. The supporting plate position was found to influence greatly the peak stress in the plate itself, in the host bone and in the graft. An anteromedial plate position largely reduced the stress in these elements at maximal gait load.

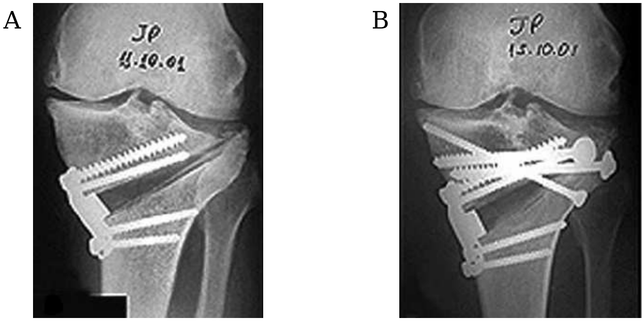

Figure 2.24: (A) Anteroposterior view of the left knee 4 weeks post-operatively, showing a grossly displaced osteotomy, loss of correction and the fracture line extended into the lateral plateau. (B) Anteroposteror view after indirect reduction and percutaneous fixation with large-fragment screws. Figures from [133].

In conclusion, an optimized wedge, supporting plate configuration for open wedge tibial osteotomy was proposed. Based on the results of the numerical study, a partial loading of the knee below 20% of the maximal gait load (about 50 kg) should favor a good osteointegration of a relatively compliant wedge (between 0.5 and 3 GPa). The use of two crutches during the first six weeks postoperatively should be prescribed to the patient so that the maximal knee load can be limited under 50 kg. This limitation should also provide sufficient safety margins against mechanical failure of the bone, wedge and supporting plate which might lower the occurrence of complications such as loss of correction due to wedge settlement and undisplaced fracture of the tibial head.

The biomechanical model developed in this chapter is a useful tool for the development of new bone grafts. It brought new insight on the biomechanics involved in open wedge tibial osteotomy and could perhaps contribute to avoiding technical tricks such as the one reported by Paccola *et al.* [133] (see Figure 2.24). Indeed, it is likely that the fracture of the tibial plateau reported in [133] was due to the stiff metallic block that was placed in an antetomedial position. As discussed in the previous section, such a configuration may induce high local stresses in the bone structure that could be avoided by placing a compliant wedge in a posteromedial position.

CHAPTER 3

Porous Construct for Artificial Bone Substitute

The study of open wedge tibial osteotomy presented in the previous chapter considered the wedge as a bulk solid material with elastic properties. This simplification was made *a priori* to identify the mechanical environment of the wedge. However, it did not take into account phenomena that might take place at an intermediate length scale and could impact the wedge's mechanical behavior and its osteointegration.

In this chapter, the wedge is no longer considered as a solid bulk material but as a *construct* which refers to a porous material (see Figure 3.1) impregnated with bone cells and saturated with a fluid. The combination of these three components may provide the necessary characteristics for its use as an efficient bone substitute. Indeed, the porous material may ensure the structural stability, the bone cells may enhance the construct osteoinduction and osteogenesis and finally, the saturating fluid provide a dynamic media that is likely to transport of biochemicals, wastes, nutriments and cells throughout the construct.

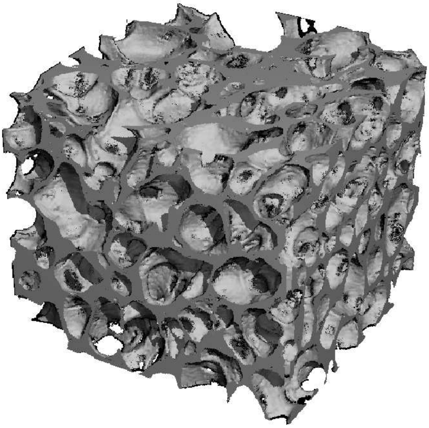

Figure 3.1: The 3D skeleton reconstructed from micro CT images of the PLLA-5%βTCP bone substitute developed at EPFL.

At an intermediate length scale, the systematic screening that was initiated in chapter 2 at a larger length scale is pursued to identify the effects of fluid and porous solid mechanics on the construct osteoinduction and integration. The aim of this systematic screening is to identify target parameters that may favor the construct osteointegration and osteoinduction. The chapter is divided into three parts that focus respectively on the fluid, on the porous solid and finally on fluid movement due to the solid skeleton deformation.

The first concern is to identify an adequate fluid that may serve as a cell delivery system to impregnate the construct with bone cells and favor the cell proliferation. Indeed, the fluid may greatly impact the cell viability and might in certain cases contribute to the construct's mechanical behavior. It is thus essential to first search for a fluid that most suits the biological requirements before studying the construct's mechanical behavior. A simplified bioengineering approach is adopted to measure the cell viability associated with two different cell delivery systems.

Then, the mechanical behavior may be identified for a particular construct composed of fluid and the PLLA-5%βTCP porous material developed by Dr. L. Mathieu at EPFL [119]. The aim of this identification is double. First, it defines the range of clinical applications in which the new construct may be employed by defining its limiting fatigue stress. Second, the identification of a viscoelastic constitutive law provides detailed information on the construct's mechanical behavior that may be used to determine the suitability of the PLLA-5%βTCP construct in a particular clinical application.

Finally, the fluid motion inside a dynamically loaded construct could be evaluated thanks to the identification of the PLLA-5%βTCP and fluid mechanical properties carried out in the first two parts of this chapter. The goals of this third part are first to evaluate the fluid motion inside the PLLA-5%βTCP construct and second, to propose ideal mechanical and fluid conductivity properties that may be targeted to optimize the construct osteoinduction and osteointegration. Poroelastic theory is used to compute the average fluid volume exchange between the construct and its environment and the average fluid-induced shear stress. These two parameters are assumed to play a significant role in the construct osteointegration and osteoinduction as they represent the average transport of nutriment, wastes, biochemical and cells throughout the construct and the average mechanical stimulation applied on the embedded bone cells. Consequently, the fluid volume exchange should be maximized and the fluid-induced shear stress should stay within a given interval that is favorable to the bone cell activity.

3.1 Biological Aspects of an Artificial Bone Graft

An ideal bone graft is a graft that is progressively replaced by new bone produced by the host's cells. Such a process may be possible if *(i)* the host's bone cells are recruited inside the graft, if *(ii)* the recruited bone cells begin to appose new bone on the graft's skeleton and if *(iii)* the bone graft resorbs progressively.

First, the cell recruitment inside the construct is triggered by the presence of specific proteins, in specific concentrations and concentration gradients. The osteoinduction process is a complex mechanism that is not fully understood to date. Nevertheless, some key proteins have been identified. For instance, it is shown that a graft loaded with the transforming growth factor β 1 (TGF-β1) enhances the recruitment of mesenchymal stem cells inside the graft [75]. In addition, TGF-β1 is identified in many studies as playing a key role in bone formation processes [34, 114, 130]. Similarly, bone morphogenic proteins (BMPs) are also shown to play important roles in mesenchymal cell recruitment [97]. Therefore, these proteins among others should be present inside the construct and produced or released gradually.

The second step of graft integration is more complicated as several biological processes have to take place in sequence. First, the mesenchymal stem cells have to differentiate into bone forming cells (osteoblasts). This complex process has been shown to be triggered by numerous proteins [34, 114, 116, 130] such as TGF-β1,2 and BMPs but can also be sensitive to runt-related transcription factors (RUNXs), zinc finger-containing transcription factors (Osterix), β-catenin (CTANN1) [205] and others. Second, once the mesenchymal cells have differentiated into osteoblasts, proper chemical and mechanical stimulation should be applied to the cells so that they begin to produce bone. Once again, the production of numerous proteins leading to chemical cascade reactions takes place. To name a few, the major proteins that regulate the synthesis of bone are TGF-β1,2, prostaglandins (PTGs), insulin-like growth factor-I (IGF-I), fibroblast growth factors (FGFs), vascular endothelial growth factor (VEGF), connective tissue growth factor (CTGF) and parathyroid hormone (PTH) [33, 129, 132, 159, 190].

One of the solutions to initiate the appropriate biological cascades that lead to bone formation could be to include bone cells inside the graft, prior to the graft implantation. The inclusion of fetal bone cells, which are rich in tissue repair factors, inside the graft may produce the necessary proteins for the recruitment and differentiation of the host's mesenchymal stem cells. The principal advantage of cell inclusion over incorporating growth factors in the construct is that cells would produce the osteogenic signals continuously whereas embedded growth factor would disappear gradually. The subsequent mechanical load might then be sufficient to stimulate the differentiated cells and the embedded fetal cells to start forming new bone.

Fetal bone cells were chosen as they are a promising alternative source of allograft bone cells. Indeed, they have been shown to produce markers of differentiated osteoblasts [122], and to produce a mineralized matrix [123] when chemically stimulated. Although the immunological advantages of fetal cells are still debated [45, 49, 65, 131], they are successfully used in skin constructs [70] and in liver transplantation [188]. Moreover, fetal transplantation is the gold standard in neurology [35, 151, 156]. Therefore, it may be hypothesized that allogenic fetal bone cells may be a good candidate for providing osteoinduction to the artificial construct. In addition, the use of fetal bone cells should present several advantages to other cell sources as they are available in large quantities and proliferate more rapidly than adult bone cells [122]. Finally, it is important to note that one single donor of fetal bone tissue may be the source of billions of cells stored in a cell bank and ready for clinical use [146].

3.2 Cell Delivery Systems

The impregnation of an artificial bone graft with bone cells might be achieved by suspension of the cells in a fluid carrier that is then injected inside the porous construct. Two solutions were envisaged: the porous artificial graft skeleton is impregnated with cells that were either suspended in (*i*) a fibrin gel or (*ii*) a standard tissue culture medium. Each solution has its advantages and drawbacks which are discussed in the following sections.

3.2.1 Fibrin Gel as Cell Carrier

Fibrin gel was, *a priori*, an appealing solution. First, from a practical point of view, the graft's impregnation with bone cells embedded in fibrin gel could be achieved quickly as the gelling time is of the order of one minute. Second, the component of fibrin gels, which are fibrin and thrombin, have been shown to have interesting biological properties. Indeed, thrombin is known to stimulate osteoblast proliferation [2,58], chemotaxis [92,107] and to inhibit osteoblast *apoptosis* [135]. In addition, thrombin increases angiogenesis via the production of VEGF by *megakaryocytes* [121] and up-regulates inflammatory cytokines at bone repair sites [194]. Finally, Bluteau *et al.* [14] showed that mouse osteoblasts (MC3T3-E1) cultured on fibrin gel (Tissuecol®, Baxter AG, Vienna, Austria) with low thrombin concentration produce VEGF.

On the other hand, fibrin gel as a cell carrier could present several drawbacks. First, it is expensive (70 €/ml) as it is derived from human plasma. The cost associated with the use of fibrin gel for the impregnation of a quarter wedge was estimated at 380 € per wedge, which would double the synthetic graft price. Besides this major drawback, the presence of thrombin is shown to promote tumor progression and metastasis in animals [115], and could present similar effects in humans. In addition, Bensaïd *et al.* [12] showed that the number of mesenchymal stem cells embedded in a fibrin gel (and not on the gel surface as in Bluteau's study [14]) was constant during the first 9 days which corresponds to the time necessary for fibrin dissolution. As a result, the mesenchymal cells began to proliferate only after total gel dissolution.

I repeated Bensaïd's experiment to assess the effect of fibrin gel on the embedded fetal cells. First, human fetal bone cells were obtained from a cell bank created by the Orthopedic Cell Therapy Unit in CHUV. The bone cells were harvested from biopsies done on fetal femur following voluntary interruption of pregnancy after 13 to 16 weeks gestation and in accordance with the Ethics Committee of University Hospital in Lausanne (Ethical Protocol 51/01). The fetal cells were maintained in culture by passaging once a week and culturing at 37°C in humidified, 5% CO_2 atmosphere and under normal culture conditions DMEM (Invitrogen, Carlsbad, CA), 10% FCS (Sigma-Aldrich, St. Louis, MO), 2mM of L-Glutamine (Invitrogen, Carlsbad, CA). Fetal cells between passage 4 and 6 were finally embedded in Tissucol® (1 IU[1]/ml thrombin + 27.5 mg/ml fibrin) at a final concentration of $2 \cdot 10^5$ cells/ml. To do so, the cells were first suspended in the thrombin solution and then mixed with fibrinogen using the duplojet® system. The gels were poured into PTFE moulds of 8 mm diameter that were then removed after one hour. The gel samples were then put in a 6-well plate with 5 ml of standard culture medium that was replaced every three days.

The fetal cell population inside the fibrin gel was estimated by DNA mass as it is a reliable method for assessing cell proliferation in 3D culture [127]. After rinsing the remaining fibrin gel in PBS, it was digested in a lysis buffer supplemented with 1% β-mercaptoethanol. DNA extraction was carried out with DNAeasy Kit (Qiagen, Chatsworth, CA) according to the manufacturer's instructions. The DNA quantification using fluorophores (Hoechst 33258, Sigma-Aldrich, St. Louis, MO) and multilabel plate reader (Wallac Oy,Turku, Finland) was carried out every 3 days for 9 days. The gel mass was measured at these time points and the experiment was repeated in triplicate.

A pronounced decrease of cell number was observed at day 3 and day 6 (see Figure 3.2). Simultaneously, the dissolution of fibrin gel took place progressively and total gel dissolution was observed at day 6. Once the fibrin gel was totally dissolved, the remaining fetal cells again began to proliferate, indicating that the presence of the fibrin gel strongly inhibited fetal cell proliferation.

---

[1] International Unit

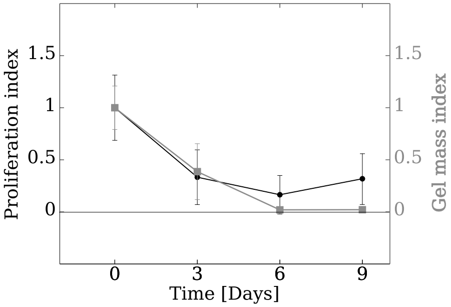

Figure 3.2: Proliferation curve (in black) of fetal cells inside Tissucol fibrin gel normalized to the quantity of cells at day 0 plotted together with the normalized gel mass evolution (in gray). ($n = 3$).

In a subsequent experiment, the presence of dead and live cells were checked at day 0, 3 and 6 using fluorophore labeling and confocal microscopy (TCS-SP2 AOBS, Leica Microscope, Germany). Fluorescein diacetate (Sigma-Aldrich, St. Louis, MO) at a final concentration of 12.5 μg/ml was used to label live cells and propidium iodide (Sigma-Aldrich, St. Louis, MO) at a final concentration of 10 μg/ml was used to label dead cells. Figure 3.3 shows that the amount of dead cells increased between day 0 and 6. At day 0, about 90% of the cells at the periphery were alive. Few cells could be observed at the sample center which was probably due to the high opacity of the gel at this location. In addition, the fluorophore might not have reached the sample center due to the high distance and low diffusion rate inside the dense fibrin gel. Therefore, I assumed that the border was representative of the whole sample for day 0 and 3. At day 6, the dissolution of fibrin gel was complete and the remaining cells were in clusters. It appeared that at the center of these clusters, cores of dead cells were surrounded by a layer of live cells. The external sample contour was still clearly marked by live cells indicating that cells had more chance to survive at the sample periphery than at its center. In addition, some cells succeeded in escaping the gel (see arrow on Figure 3.3 B) and started proliferating on the cell culture dish. Few dead cells were found in these new cell colonies indicating that fetal cells proliferated better outside the fibrin gel than embedded within.

In conclusion, Tissucol® fibrin gel might not be appropriate for the delivery of fetal bone cells as it inhibited cell proliferation and induced cell death. Therefore, I chose to use a normal cell culture media as the cell delivery system. The drawbacks and advantages of this procedure are discussed in the following section.

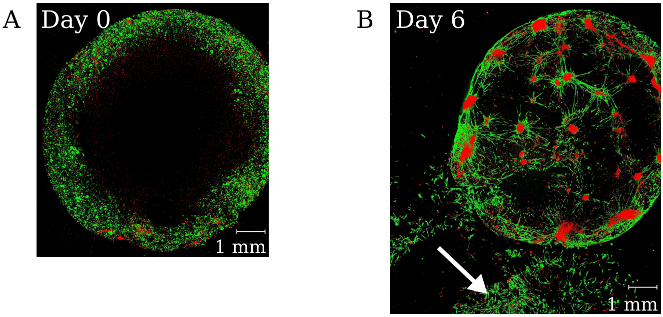

Figure 3.3: Projection of images taken every 15 μm of fetal cells loaded in fibrin gel (A) at day 0 and (B) at day 6.

3.2.2 Culture Medium as Cell Carrier

The main advantage of using a normal culture medium as a cell carrier is that it is designed to provide all the nutriments that the cells need for growth and proliferation, based on years of cell culture experience. In addition, the related cost is small in comparison with fibrin gel as 500 ml of clinical grade culture medium costs less than 30 €. Finally, a better exchange of fluid between the construct and the environmental fluid may be achieved when low viscosity fluid is used rather than a gel as mixing is enhanced.

Based on the results presented in the previous section, fetal bone cells cultured in a standard culture medium proliferate better than in a fibrin gel and show a higher viability. However, the impregnation process with a culture medium may be less effective. Therefore, two seeding processes were studied to optimize the number of cells entering the construct, the cell viability and the impregnation time. The first method consisted of pipetting cells suspended in culture medium on top of the construct skeleton. The second method used a custom device developed at the Laboratory of Biomechanical Orthopedics EPFL-HOSR for construct impregnation (see Figure 3.4 B). In both methods, a solution of 2 million fetal bone cells per millilitre were used to impregnate cylindrical porous samples (ChronOs, Synthes, Switzerland) of 8 mm diameter and 8 mm height. In the first method, the solution was pipetted onto the sample top. After 5 minutes of infiltration, the sample was turned up-side-down and the cell solution was pipetted on the other end of the sample. The samples were then left 1 hour at 37°C allowing the cell to attach to the construct skeleton. Finally, the culture medium was added to completely cover the samples and incubated at 37°C, 100% humidity and 5% CO_2. 24 hours later, the samples were rinsed in *PBS*, cut in half along their longitudinal plane and the fluorophores were added to enable live/dead labeling (fluorescein diacetate/propidium iodide). The sample top and the longitudinal section were then observed using inverted confocal microscopy.

The second impregnation method used an adjusted silicon tube that confined the sample radially. Syringes that permitted the control of the impregnation process were fitted on both ends of the tube (see Figure 3.4) . The cell suspension solution was loaded in the lower syringe and was pushed upward for a bottom/top sample impregnation, allowing the entrapped air to

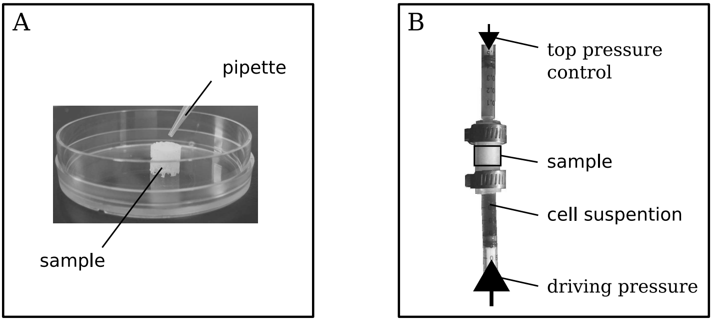

Figure 3.4: The two impregnation techniques used: (A) pipetting and (B) custom impregnation device.

escape by buoyancy force. Meanwhile, the pressure at the sample top was controlled by the top syringe to force the solution to enter the void pores. The sample was then left inside the impregnation device for 30 minutes and the silicon tube was removed. Finally, the culture medium was added to completely cover the sample and the sample was stored at 37°C until observation was carried out 24 hours later.

The time required for impregnation of one sample was similar in both methods. On one hand, the pipetting process was fast, but an infiltration time of two times five minutes was required for the cell suspension solution to enter the construct. On the other hand, the mounting and unmounting of the custom impregnation device required about ten minutes in total, but the impregnation process itself was fast (about one minute) and user friendly. Indeed, the custom impregnation device could be prepared in advance, stored in a sterile environment, and used later for the impregnation. In both cases, impregnation took about one hour.

Both methods were then compared for their ability to carry cells inside the construct. To do so, the cell volumes were reconstructed in three dimensions from the confocal microscopy images using IMARIS software (Bitplane AG, Switzerland). The sample cross sections were divided into horizontal strips of 100 μm height, 470 μm thickness and 8 mm width (see Figure 3.5). The total number of cells within these strips were determined by counting the number of unitary cell volume of 2500 μm^3 that could be encompassed in the reconstructed volumes. The cell concentration was finally determined by dividing the total number of cells by the total volume of each strip.

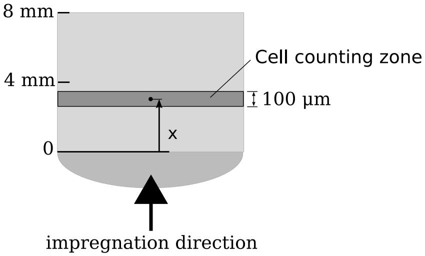

Figure 3.5: Reconstruction zone for cell number analysis.

The cell concentration across the sample central-vertical cross section varied with the impregnation method. First, the pipetting method induced a very high cell concentration ($9.6 \cdot 10^3$ cell/μl) on the sample end that rapidly decreased with increasing distance from the sample end (see Figure 3.6 A). At the sample center, i.e. at 4 mm distance from sample end, very few cells could be found (41 cell/μl). When the custom impregnation device was used, a smaller difference between the sample bottom and center was observed. Due to the direction of impregnation from bottom to top, more cells were located on the sample bottom (1782 ± 337 cell/μl) than at its center (372 ± 119 cell/μl) and top (452 ± 165 cell/μl).

The ratio of live to dead cells was also dependent on the impregnation method. The pipetting method induced a higher proportion of live to dead cell ratio than the custom impregnation device for distances smaller than 1 mm from sample bottom (see Figure 3.6 B). However, for distances larger than 1 mm, higher live/dead cell ratio (about 5) was observed when the custom impregnation method was used rather than pipetting method. As a result, the pipetting method induced smaller cell damage in the highly populated extremities. On the other hand, the custom impregnation device was more harmful for the cells than pipetting, but a sufficient live population was safely brought to the sample center.

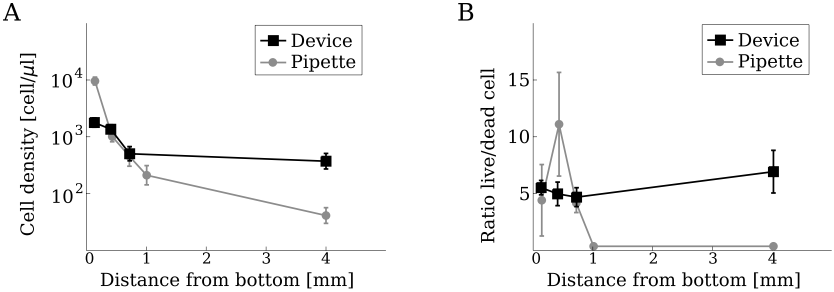

Figure 3.6: Cell density (A) and live/dead cell ratio (B) as a function of the distance from sample bottom for two impregnation methods (n=3): the pipetting method called **Pipette** and the custom impregnation device called **Device**.

In conclusion, the pipetting method might be used for impregnation of a sample thinner than 2 mm, where the impregnation of thicker sample might be efficiently achieved by the custom impregnation device. Indeed, the pipetting method did not succeed in delivering a substantial quantity of cells to a distance greater than 1 mm. Although the custom impregnation device was more deleterious for the cells than the pipetting method, it established a nearly constant cell concentration throughout a thick sample. Therefore, the custom impregnation device provides a suitable process for the impregnation of thick artificial bone grafts.

3.2.3 Conclusions

First, it has been shown that fibrin gel might not be the preferred delivery system for fetal bone cells. Indeed, it was found that a population of fetal bone cells embedded in fibrin gel decreased as long as the gel was present. Only once the fibrin gel had been completely dissolved did the cells again begin to proliferate. Therefore, a normal culture medium was chosen as the cell carrier.

The next question was how to successfully impregnate large constructs and two methods were compared. The experimental data discussed in the previous section showed that the pipetting method was not capable of impregnating a construct thicker than 2 mm. On the other hand, a successful delivery of fetal cells inside a porous construct could be achieved with the use of a custom impregnation device. A concentration corresponding to one fifth of the initial cell suspension concentration was found at the center of a 8 mm thick sample. In addition, more than 80% of these cells were alive 24 hours post-impregnation. This method was efficient and rapid and is a potential candidate for clinical applications.

3.2.4 Perspectives

The optimization of the impregnation method was carried out in the framework of a tissue engineering project. Initially, it was foreseen that the impact of mechanical loads applied to the constructs on the expression of genes associated to the bone cell activity (RUNX2, osteocalcin, osteopontin, osteonectin, bone sialoprotein, ALP activity and collagen $1\alpha1$) would be measured. After overcoming contamination issues linked with the compression test bench (see section 3.3.1 for a description of the bench), very few intact RNA materials could be extracted from the samples. Many attempt were carried out including various tissue disruption methods such as stainless steel beads in Trizol (Invitrogen, Carlsbad, CA) and mortar and pestle in liquid nitrogen or Trypsin-EDTA (Invitrogen, Carlsbad, CA) but none of them was capable of increasing the amount of harvested RNA. Consequently, gene expression quantification by real time reverse transcriptase-polymerase chain reaction could not be achieved. Thus, the effect of mechanical load on the genes expression of fetal bone cells embedded in a PLLA construct remains an open issue. Accordingly, the following tests were carried out on PLLA constructs saturated with a culture medium but free of fetal bone cells.

3.3 Mechanical Behavior of the PLLA Bone Construct

As discussed in sections 2.1.1 and 3.1, the graft material should be gradually remodeled and replaced by newly formed bone. Therefore, the graft's material has to resorb and degrade slowly. Typically, the material's resorption should take about one year to allow its gradual replacement by newly formed bone. The degradation process is dependent on many factors; in particular the material's porosity and composition. For instance, hydroxyapatite degrades slowly (insignificant changes after 39 weeks [98] and 3.5 years [72] of implantation) and tricalcium phosphate degrades rapidly (80% volume loss after 22 to 24 weeks [153, 184]). Studies on PLLA shows that the material's degradation *in vivo* is slow for massive parts like rods and thick plates. For instance, interference screws [8], lag screws [88] and plates [179] were totally resorbed after 5 to 8 years implantation. A mass loss of between 10 and 25% after one year of implantation was observed on rods implanted in animals [73, 120] and was preceded by a 60% molecular mass loss [73]. The mechanical stiffness and strength are found to degrade on a shorter time scale. Indeed, Matsusue *et al.* [120] showed that the bending strength of 3.2 mm PLLA rods was half of the value before implantation after 12 weeks only. In addition, the bending strength decreased by 80% from its initial strength after 16 weeks of implantation.

The mechanical properties of PLLA clearly evolved with time when implanted *in vivo*. In addition, similar evolution as that observed *in vivo* was obtained by maintaining PLLA parts in PBS at 37°C and 100% humidity [73]. Therefore, the mechanical evolution of the PLLA foam was tested *in vitro* in a controlled atmosphere mimicking the physiological environment.

3.3.1 Mechanical Testing of PLLA Bone Construct

Dynamic compression forces were applied on PLLA-5%βTCP constructs by the means of a custom machine developed in collaboration with M. Martin from the Ecole d'Ingénieur du Canton de Vaud and the Laboratory of Biomechanical Orthopedics EPFL-HOSR (see Figure 3.7). This machine applied the compression forces simultaneously onto four samples through a load splitting mechanism driven by a voice coil[2] (BEI Technologies Inc., Vista, CA). A smooth and accurate mechanical loading was obtained by feedback loop using a *PID* controller coupled to a load cell. In addition, the displacement of the compression pistons was measured to monitor the gradual settlement of the samples. Finally, the temperature of the compression well located closest to the motor was measured to monitor its evolution and ensure that the temperature stayed at 37°C throughout the experiment.

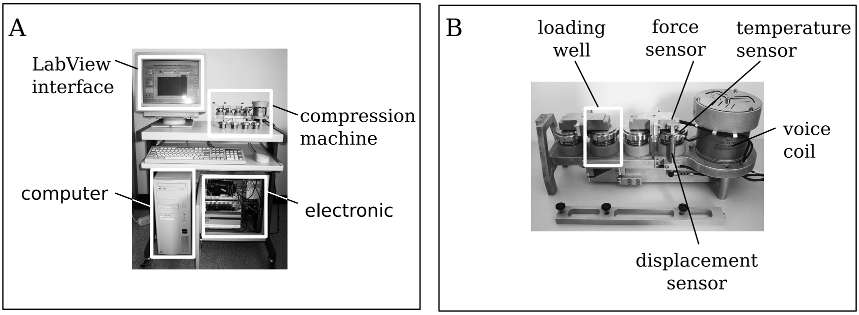

Figure 3.7: (A) The compression test bench is composed of a PC that controls a compression machine through a series of electronic devices. (B) The compression machine is driven by a voice coil that applies a required load on four samples in parallel. Force, displacement and temperature sensors where used to control and monitor the machine.

One cylindrical PLLA-5%βTCP foam sample of 8 mm diameter, 8 mm height was placed in each compression well (see Figure 3.8). A compression piston was put on top of each sample, then a cover closing the wells was added. The average sample mass was measured to be 101 ± 2 mg.

---

[2] A voice coil is a linear motor composed of a permanent magnet and a coil in which electrical current is supplied.

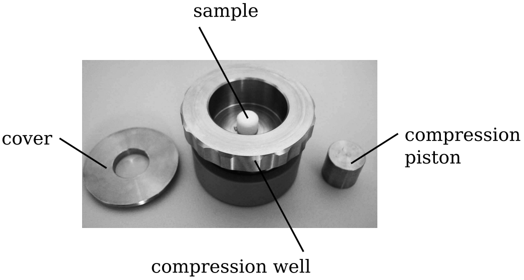

Figure 3.8: Detailed view of one of the four compression wells used for the sample mechanical loading.

The loading conditions were the following. A cyclic compression of 0.2 MPa amplitude and 0.2 MPa mean compression was applied at a frequency of 1 Hz. After 5 minutes of dynamic compression, the samples were unloaded during the next 55 minutes. Compression fatigue tests were carried out in controlled atmosphere mimicking the physiological environment, i.e. the samples were in PBS and kept at 37°C, 100% humidity and 5% CO_2.

The loading/unloading cycles were applied until visible damage on one of the four loaded samples was observed. At day 24, some debris was found floating in the compression well of one of the four loaded samples. This particular sample lost 20% of its height and its upper surface was clearly damaged. Consequently, the experiment was interrupted after 24 days of dynamic compression and 172'800 loading cycles.

The level of compression stress and number of cycles per hour applied on the sample were based on preliminary experiments. Indeed, the application of higher compression loads as well as a higher number of cycle per hour induced a premature sample breakdown. For instance, an uninterrupted application of 0.2 ± 0.2 MPa dynamic compression induced the rupture of two of the four samples after about 150'000 cycles (less than 2 days). In addition, the application of dynamic stress of 0.5 ± 0.5 MPa induced the rupture of 1 sample of the four within 1 hour of uninterrupted loading (3600 cycles). Consequently, experiments that targeted a longer loading period had to limit the compression load magnitude and the number of cycles.

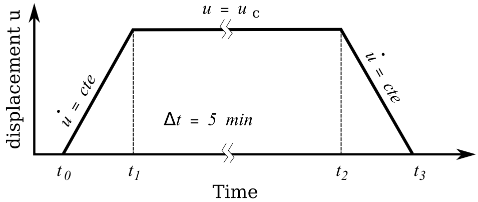

Figure 3.9: Displacement profile applied on the sample top during displacement/force test.

Every three days of dynamic loading, the samples were removed from the compression machine for accurate mechanical testing. Force/displacement measurements were carried out on a calibrated test bench (Instron, Canton, MA) at room temperature and the samples were kept immersed in PBS. A three phase loading protocol was applied (see Figure 3.9). First, the samples were compressed at a constant displacement rate of 0.008 mm/s until a maximal force of 20 N was reached. Second, the force relaxation at constant strain was measured over 5 minutes. Finally, the samples were unloaded at 0.008 mm/s. These force/displacement tests were repeated on a control group composed of four samples that were stored in PBS, at 37°C, 100% humidity and 5% CO_2 and that were not subject to mechanical stimulus.

One hour and a half later, a second strain profile was applied to the samples. A higher displacement rate of 0.08 mm/s was applied during loading and unloading phases. Again, the compression was stopped once a total force of 20 N was reached and a short relaxation phase of 10 s was left between the loading and unloading phases.

Results

First, the nominal compression stress was computed by dividing the compression force by the nominal sample cross section area.

$$\mathbf{P}_{zz} = \frac{F}{\pi R^2} \tag{3.1}$$

Assuming homogeneous strain state within the sample, the strain in the direction of compression was computed as

$$\varepsilon_{zz} = \frac{h_t - h}{h} \tag{3.2}$$

where, h_t is the the sample height at time t and h is the nominal sample height. The nominal sample height was measured on the Instron compression machine. Figure 3.10 presents a typical loading and unloading stress/strain curve for two different deformation rates. Large variations were observed from one sample to another. However, some similarities were found. First, most samples exhibited a non-linear relation between stress and strain, even at relatively small strains.

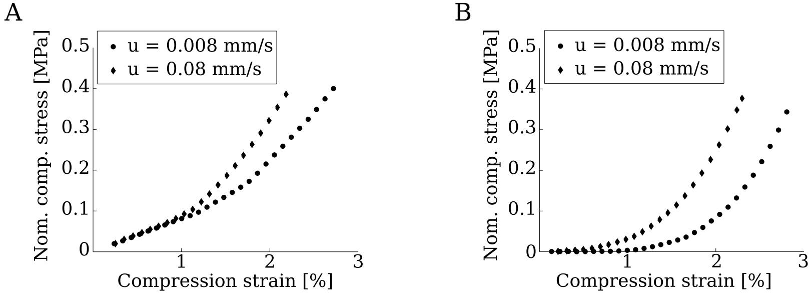

Figure 3.10: Typical stress/strain curve during (A) the loading phase and (B) the unloading phase.

Second, a strain rate dependent stiffening effect was observed on most of the samples, indicating that the PLLA-5%βTCP foam samples are viscoelastic with a short term memory effect. In addition, time evolution of the compression force under constant strain clearly indicated a stress relaxation behavior (see Figure 3.11). Third, the sample height was observed to decrease with an increasing number of applied compression cycles. Indeed, a progressive settlement of 0.2% per day on average was observed in loaded samples that showed no evidence of damage (see Figure 3.12). In addition, the samples never recovered their original height, even 6 months post-loading. On the other hand, the unloaded samples did not exhibit height settlement. Therefore, the PLLA-5%βTCP samples were subject to progressively increasing plastic deformation due to long term cyclic loading.

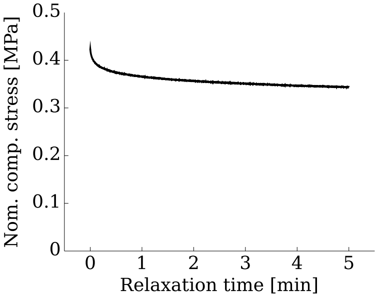

Figure 3.11: Typical relaxation curve of PLLA-5%βTCP foam.

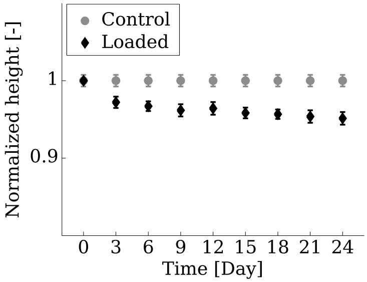

Figure 3.12: Sample height time evolution for loaded and unloaded (control) samples (n=4).

In conclusion, the mechanical behavior of PLLA-5%βTCP foam appeared to be viscoelastic at 1 hour time scale. On a longer time scale equivalent to several days, plastic deformation progressively took place due to cyclic loading. The viscoelastic behavior of the PLLA-5%βTCP constructs is studied in the framework of continuum mechanics in the following sections.

3.3.2 Construct Continuum Description

The PLLA-5%βTCP foam constructs were considered as a continuous medium. By doing so, the construct microscopic structure is not taken into account explicitly and its average effect is described by macroscopic variables. These variables are pertinent only at a length scale much larger than the material heterogeneities (or microscopic structure) scale. In addition, the physical properties describing the continuum are assumed to vary continuously from one point to another and are thus fundamentally different from the local "true" variables describing the microscopic structure.

The definition of the minimal length scale at which a continuum description is pertinent depends on the typical heterogeneity length scale and on the desired degree of refinement of the model. For instance, a rough description is obtained when the macroscopic length scale measures 10 times the characteristic length of a continuum particle. For a finer description, the object's characteristic length should be between 100 and 1000 times the typical heterogeneity length scale.

In the particular case of PLLA-5%βTCP foam constructs, the continuum theory can only give a rough representation of the construct mechanical behavior. Indeed, the construct average pore size computed from μ-CT images was found to be 20 times smaller than the sample dimensions. Unfortunately, the sample dimensions are constrained for this experiment because of cost and practical issues. Nevertheless, the constitutive law developed in the following section gives a rough but useful mechanical description of the construct.

A continuum medium is defined by its kinematics, dynamic, and constitutive laws relating the kinematics with dynamics. The basics of classical continuum mechanics are summarized in the following sections.

Kinematics

In a Lagrangian description, the initial position of every particle of an object $\mathcal{B}$ is identified by a unique vector $\mathbf{x}$. The actual position at time t of each particle $\mathbf{x}$ is given by a mapping $\mathbf{y} = \mathbf{y}(\mathbf{x},t)$ called the deformation. The object's displacement is then defined as

$$\mathbf{u}(\mathbf{x},t) = \mathbf{y}(\mathbf{x},t) - \mathbf{x}, \tag{3.3}$$

its velocity is given by

$$\frac{\partial \mathbf{u}}{\partial t} = \dot{\mathbf{u}} = \dot{\mathbf{y}} \tag{3.4}$$

and its acceleration is

$$\frac{\partial^2 \mathbf{u}}{\partial t^2} = \ddot{\mathbf{u}} = \ddot{\mathbf{y}} \ . \tag{3.5}$$

The object's deformation gradient $\mathbf{F}$ is a tensor defined by

$$\mathbf{F} = \nabla \mathbf{y} \ . \tag{3.6}$$

where $\nabla(\cdot)$ denotes the material gradient of $(\cdot)$. To obtain an objective[3] description of the object deformation, the right Cauchy-Green strain tensor is defined.

$$\mathbf{C} = \mathbf{F}^T \mathbf{F} \tag{3.7}$$

---

[3] A principle or a quantity is called objective if it is frame indifferent, or in other words invariant under changes of observers [71].

An equivalent strain tensor that is useful because it is trivial in the undeformed state is the Green-Lagrange strain tensor

$$\mathbf{E} = \frac{1}{2}(\mathbf{C} - \mathbf{I}) \tag{3.8}$$

where **I** is the identity matrice. Finally, the rate of the deformation gradient is given by

$$\dot{\mathbf{F}} = \frac{\partial}{\partial t}\mathbf{F} = \nabla \dot{\mathbf{y}} = \nabla \dot{\mathbf{u}} \tag{3.9}$$

and the corresponding Green-Lagrange strain rate tensor is

$$\dot{\mathbf{C}} = \dot{\mathbf{F}}^T \mathbf{F} + \mathbf{F}^T \dot{\mathbf{F}} \,. \tag{3.10}$$

Dynamics

The dynamics of a continuum medium is given by the mass and momentum balance equations. It was assumed that no mass exchange took place between the object $\mathcal{B}$ and its environment and that no mass was produced inside the same object. Consequently, mass is conserved for all subdomains of $\mathcal{B}$. Using the localization theorem, it is concluded that the mass density in the nominal description is only a function of its position.

The balances of linear and angular momentum are a generalization of Newton's first and second principles of motion in the context of continuum mechanics [71]. The linear momentum balance states that the sum of inertial forces is equal to the sum of external body forces and contact forces. Using the Reynolds transport theorem together with Cauchy's stress theorem yields an integral form of the linear momentum conservation. Finally, applying the localization theorem[4] allows the so called Cauchy's equation of motion to be written which is in fact the local linear momentum balance.

$$\rho_0 \ddot{\mathbf{u}} = \nabla \cdot \mathbf{P} + \mathbf{f}\rho_0 \tag{3.11}$$

The inertial force is thus equal to the sum of the divergence of the nominal stress tensor **P**, also called the Piola-Kirchhoff I stress tensor and the body forces, expressed here as the product of the acceleration field **f** and the nominal mass density ρ_0. A similar procedure is necessary to derive the local balance of angular momentum which may be expressed in nominal form as

$$\mathbf{F}\mathbf{P}^T - \mathbf{P}\mathbf{F}^T = 0 \tag{3.12}$$

or in material form

$$\mathbf{S} = \mathbf{S}^T \,. \tag{3.13}$$

The balance of angular momentum implies that the material stress tensor **S**, also called Piola-Kirchhoff II, is symmetric.

---

[4] The postulate of local state stipulates that the evolution of an homogeneous system is characterized by the same set of variables as those describing the equilibrium state, regardless of rate of change or gradient of these variables.

Thermodynamics

When describing the mechanical behavior of a solid continuum, the mass and momentum balance equations are not sufficient. Indeed, the total stress tensor appearing in the momentum balance will be related to the solid kinematics. These relations are called constitutive equations and are often based on arbitrary hypotheses that best fit experimental observations. However, thermodynamics gives a general framework for the development of constitutive laws.

Thermodynamics studies the energetic evolution of a given system and is composed of two principles. The first principle is conservation of energy which adds equations to the system of equations composed of the mass and momentum balance equations. The second principle is of different nature as it is expressed as an inequality. Therefore, it only imposes certain restrictions on the constitutive laws.

First Principle The conservation of energy for a solid continuum in the absence of heat source or heat exchange may be written in material and local form as

$$\rho_0 \dot{e} = \frac{1}{2}\mathbf{S} : \dot{\mathbf{C}} \tag{3.14}$$

where e is the specific internal energy.

Second Principle For closed system, the non-negativity of the specific entropy s simplifies to

$$\rho_0 \frac{\partial s}{\partial t} \geq 0 \tag{3.15}$$

Using the definition of the specific free energy ψ

$$\psi = e - Ts \tag{3.16}$$

where T is the absolute temperature, the first principle (3.14) may be substituted into the second principle. Finally, assuming an isothermal process yields to the Clausius-Duhem inequality for a continuous solid.

$$\frac{1}{2}\mathbf{S} : \dot{\mathbf{C}} - \frac{\partial \psi}{\partial t} \geq 0 \tag{3.17}$$

This last equation establishes the framework for the development of a constitutive law by postulating the existence of free energy functions ψ that shall satisfy the inequality (3.17).

The PLLA-5%βTCP Construct Constitutive Law

The experimental data discussed in section 3.3.1 suggested that the mechanical behavior of the artificial bone substitute developed at the EPFL is viscoelastic with short and long memory effects. In this section we propose to model the mechanical behavior of the construct by a constitutive equation of the type

$$\mathbf{S} = \mathbf{S}_e(\mathbf{C}) + \mathbf{S}_v\left(\mathbf{C}, \dot{\mathbf{C}}\right) + \int_0^\infty \mathcal{F}\,(\mathbf{C}(t-s))\, ds \tag{3.18}$$

where $\mathbf{S}_e$ is the elastic stress component, $\mathbf{S}_v$ is the stress due to short term viscous memory effect and the last term represents the long term viscous memory effect. The constitutive equation (3.18) was proposed by Pioletti to model soft tissue and in particular human knee ligaments and tendons [140] and is adapted in this study to model polymer foam.

The constitutive law (3.18) must fulfill four basic requirements: *(i)* be compatible with thermodynamic principles, *(ii)* be stable, *(iii)* present no internal stress at the initial undeformed state and *(iv)* fit the experimental results.

First, thermodynamic principles require that the Clausius-Duhem inequality (3.17) is globally verified. In other words, the total energy dissipated by the material has to be non-negative. A stronger statement may be that the dissipations associated with the viscous short and long term memory are individually non-negative. As a result, each term of equation (3.18) may be considered separately with respect to the Clausius-Duhem inequality. It should be noted that such a statement is a restriction of the constitutive law set that simplifies its identification but could result in difficulties in fulfilling the other three requirements.

Second, the stability of the constitutive equation requires that the associated free energy function ψ is convex. It is sufficient to demonstrate that the free energy function associated with the elastic response, the viscous long term memory and the viscous short term memory are individually convex. Therefore, the convexity of each potential was considered independently from each other.

The third requirement assumed that no internal stresses were present at the initial undeformed state.

$$\mathbf{S}(\mathbf{I},t=0)=\mathbf{S}_e(\mathbf{I})+\mathbf{S}_v(\mathbf{I}\left(\dot{\mathbf{C}}(t=0)\right)+\int_0^\infty \mathcal{F}\ (\mathbf{C}(-s))\,ds=0$$

Again, the contribution of each term was considered separately.

Last but not least, a requirement was to obtain a good fit between experimental data and the developed viscoelastic law. This was checked by computing the correlation coefficient between the fitted constitutive law and the set of experimental data of section 3.3.1. For clarity, the identification of the elastic, viscous short and long term memory constitutive laws are discussed separately. However, the identification of the constitutive law parameters was computed by considering the elastic and viscous contributions together.

Elastic Response The Clausius-Duhem inequality (3.17) simplifies for purely elastic material to [106]

$$\mathbf{S}_e=\frac{\partial\psi_e}{\partial\mathbf{C}} \quad \Leftrightarrow \quad \mathbf{P}_e=\frac{\partial\psi_e}{\partial\mathbf{F}}\ . \tag{3.19}$$

Consequently, a constitutive law derived from an elastic potential ψ_e automatically satisfies the thermodynamic restriction. The elastic potential ψ_e must be convex to present stability and to be physically meaningful. The definition of a convex function is a function which second derivative matrix with regard to its variables is positive definite.

$$\frac{\partial^2\psi_e}{\partial\mathbf{C}^2}>0 \tag{3.20}$$

The assumption that the elastic stresses are zero at the initial undeformed state yields

$$\mathbf{S}_e(\mathbf{I})=\mathbf{P}_e(\mathbf{I})=0\ . \tag{3.21}$$

Finally, a third order elastic law as a function of its principal stretches λ_i was found to fit the experimental data well. The corresponding free energy function is

$$\psi_e(\lambda_1,\lambda_2,\lambda_3)=\sum_{i=1}^{3}(a\lambda_i^4+b\lambda_i^3+c\lambda_i^2+d\lambda_i+e)\ , \tag{3.22}$$

with

$$a=\frac{\Delta E_{1\%}}{4\kappa}\ ,\qquad b=-\frac{\Delta E_{1\%}}{\kappa}\ ,\qquad c=\frac{E_0}{2}+\frac{3\Delta E_{1\%}}{2\kappa}\ ,$$
$$d=-E_0-\frac{\Delta E_{1\%}}{\kappa}\ ,\qquad e=\frac{E_0}{2}+\frac{\Delta E_{1\%}}{3\kappa}\ .$$

where E_0, $\Delta E_{1\%}$ and κ are constants. The constants E_0 and $\Delta E_{1\%}$ are the elastic modulus in the undeformed state and the hardening of the elastic modulus at 1% compressive stretch respectively and are defined as

$$E_0=\left.\frac{\partial P_i}{\partial\lambda_i}\right|_{\lambda_i=1}\ , \tag{3.23}$$

$$\Delta E_{1\%}=\left.\frac{\partial P_i}{\partial\lambda_i}\right|_{\lambda_i=0.99}-E_0\ , \tag{3.24}$$

where P_i is the i-th principal nominal stress. The constant κ takes the value of 0.0003. The elastic potential (3.22) is indeed convex as

$$\frac{\partial^2\Psi_e}{\partial\lambda_i\partial\lambda_j}=\left(\frac{3\Delta E_{1\%}}{\kappa}\lambda_i^2-\frac{6\Delta E_{1\%}}{\kappa}\lambda_i+E_0+\frac{3\Delta E_{1\%}}{\kappa}\right)\delta_{ij}>0\quad\forall\,E_0,\Delta E_{1\%}>0$$

holds, where δ_{ij} is the Kronecker delta. The elastic constitutive equation derived from the potential (3.22) may be written in nominal form as

$$\mathbf{P}_e(\lambda_1,\lambda_2,\lambda_3)=\left[\frac{\Delta E_{1\%}}{\kappa}\lambda_i^3-\frac{3\Delta E_{1\%}}{\kappa}\lambda_i^2+\left(E_0+\frac{3\Delta E_{1\%}}{\kappa}\right)\lambda_i\right.$$
$$\left.-\left(E_0+\frac{\Delta E_{1\%}}{\kappa}\right)\right]\delta_{ij}\ . \tag{3.25}$$

Finally, the elastic constitutive expression (3.25) fulfills the unstressed state in the initial undeformed state as $\mathbf{P}_e(1,1,1)=0$.

The elastic constitutive law (3.25) was defined by the stretch in the three principal directions. Such a formulation has the advantage of accessing directly the relation between stretch and stress. On the other hand, such a formulation requires the computation of the eigenvalues of $\mathbf{F}$ (spectral decomposition), which may be time consuming in a 3D numerical application. In the case of plan strain, an explicit equivalent formulation as a function of the three deformation invariants $I_1=tr(\mathbf{C})$, $I_2=sec(\mathbf{C})$, and $I_3=det(\mathbf{C})$ may be derived from equation (3.25) [43].

Viscous Short Term Memory To define the complementary law governing the viscous short term memory effect, the existence of a dissipative potential $W_v(\dot{\mathbf{C}})$ is postulated such that

$$\frac{\partial W_v}{\partial \dot{\mathbf{C}}} = \mathbf{S}_v \, . \tag{3.26}$$

The Clausius-Duhem inequality for an isothermal process simplifies to

$$\Phi = \frac{1}{2}\mathbf{S}_v : \dot{\mathbf{C}} \geq 0 \tag{3.27}$$

where Φ is the so called intrinsic dissipation. substituting the definition (3.26) into equation (3.27) gives the thermodynamic restriction on the dissipative potential.

$$\frac{1}{2}\frac{\partial W_v}{\partial \dot{\mathbf{C}}} : \dot{\mathbf{C}} \geq 0 \tag{3.28}$$

The above inequality is fulfilled for all potentials that are convex, positive and nil at the origin [106]. A dissipative potential that fulfills the thermodynamics restriction and the stability requirement in addition to fitting well with the experimental results is

$$W_v = \frac{\eta_s^2}{2}(I_1 - 3)^2 \, tr(\dot{\mathbf{C}}^2) \, . \tag{3.29}$$

The associated short term memory stress is then

$$\mathbf{S}_v = \eta_s^2 (I_1 - 3)^2 \dot{\mathbf{C}} \quad \Leftrightarrow \quad \mathbf{P}_v = \eta_s^2 (I_1 - 3)^2 \mathbf{F}\dot{\mathbf{C}} \, . \tag{3.30}$$

Indeed, the Clausius-Duhem inequality is met because $\eta_s^2 \geq 0$, $(I_1 - 3)^2 \geq 0$ and $\dot{\mathbf{C}} : \dot{\mathbf{C}} \geq 0$ holds for all η_s, $\mathbf{C}$ and $\dot{\mathbf{C}}$. In addition, the stress state associated with the undeformed configuration is zero as $I_1 - 3 = 0$ when $\mathbf{C} = 0$. Finally, the dissipation potential is stable as it is convex.

$$\frac{\partial^2 W_v}{\partial \dot{\mathbf{C}}^2} = 2\eta_s^2 (I_1 - 3)^2 \mathbf{I} \geq 0 \tag{3.31}$$

Viscous Long Term Memory The long term memory contribution to the total stress was assumed to be governed by the principle of fading memory. A general approach to developing the free energy potential associated with the long term memory effect in linear viscoelasticity is described in Coleman and Noll's fundamental paper [36]. In particular, Fabrizio and Morro [53] showed that the fading memory stress

$$\mathbf{S}_{v.long} = \int_0^\infty \dot{\mathbf{G}}(s)(\mathbf{C}(t-s) - \mathbf{I}) \, ds \tag{3.32}$$

with an exponential relaxation function

$$\mathbf{G}(s) = \mathbf{G}_\infty + \mathbf{G}_0 e^{-\frac{s}{\tau}} \, , \qquad \tau > 0 \, , \tag{3.33}$$

fulfills the thermodynamics restriction for all $\mathbf{G}_0 \geq 0$. Fading memory total stress may thus be modeled as a sum of n fading memories of the form (3.32, 3.33). A series of two terms seemed sufficient to fit the experimental data. It was assumed that the loading history before the start of the compression test had negligible impact on the global stress during the compression test which restricts the integration limits between 0 and t. Rewriting the viscous long term memory stress in nominal form, the equations (3.32, 3.33) became

$$\mathbf{P}_{v.long} = \int_0^t \left(-\frac{a_1}{\tau_1} e^{-\frac{s}{\tau_1}} - \frac{a_2}{\tau_2} e^{-\frac{s}{\tau_2}} \right) \mathbf{F}(t-s)(\mathbf{C}(t-s)-\mathbf{I})\, ds\,. \tag{3.34}$$

The above constitutive law fulfills the zero stress condition in an undeformed state as $\mathbf{C}-\mathbf{I}$ is zero in that case.

Parameters Identification The particular viscoelastic constitutive law described by equations (3.25, 3.30, 3.34) was then fitted to the experimental data of section 3.3.1. To do so, the sample deformations were assumed to be homogeneous. Consequently, the nominal stress in the compression direction is given by

$$\begin{aligned} \mathbf{P}_c = & \left[\frac{\Delta E_{1\%}}{\kappa} \lambda_c^3 - \frac{3\Delta E_{1\%}}{\kappa} \lambda_c^2 + \left(E_0 + \frac{3\Delta E_{1\%}}{\kappa} \right) \lambda_c - \left(E_0 + \frac{\Delta E_{1\%}}{\kappa} \right) \right] \\ & + 2\eta_s^2 (I_1 - 3)^2 \lambda_c^2 \dot{\lambda}_c \\ & - \int_0^t \left(\frac{a_1}{\tau_1} e^{-\frac{s}{\tau_1}} + \frac{a_2}{\tau_2} e^{-\frac{s}{\tau_2}} \right) \lambda_c(t-s)(\lambda_c^2(t-s) - 1)\, ds \end{aligned} \tag{3.35}$$

The zero nominal stress condition at the free boundary was used to derive a second equation that linked the radial deformation with the axial deformation. The parameters E_0, $\Delta E_{1\%}$, η, a_1, a_2, τ_1 and τ_2 were then computed by least-square optimisation of the viscoelastic constitutive equation (3.35) to the experimental data of section 3.3.1.

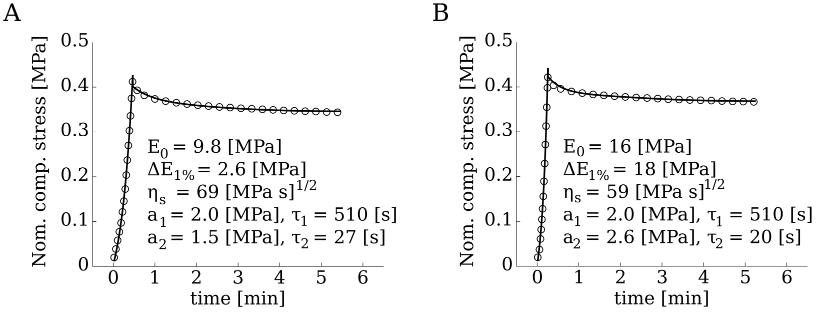

Figure 3.13: Compression/relaxation test on two PLLA-5%βTCP constructs fitted with a viscoelastic constitutive law. (A) sample before mechanical stimulation; (B) sample after 21 days of mechanical stimulation.

The constitutive law accurately fitted the experimental data and succeeded in modeling the long term memory effect (see Figure 3.13) as well as the short term memory effect (see Figure

3.14). The correlation coefficients between the experimental data set and the fitted curves were higher than 0.95 for all eight samples and all time points.

On the other hand, high variability of the parameters was observed. Although the mass of each sample was within a 2% interval, there was a high variation of the local 3D architecture due to the gaz foaming process used for manufacturing the samples. In particular, the pore diameter standard deviation computed from μ-CT images was 45% of the sample mean pore diameter and about 3% of the sample diameter. It is therefore likely that the variation of the 3D architecture has a non negligible impact on the sample mechanical properties. The high variability is inherent to the manufacturing process and to the small sample dimension with regards to the mean pore size. The use of larger samples would thus decrease the variability between samples. Nevertheless, most of the parameters were stable with the exception of the viscous hardening property (see Figure 3.15).

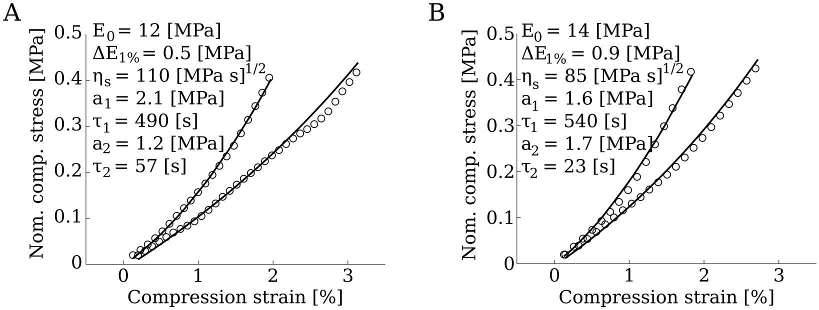

Figure 3.14: Compression test on two PLLA-5%βTCP constructs at strain rate 0.001 s^{-1} and 0.01 s^{-1}.

Another limitation of the constitutive law (3.35) is its isotropy. In actual fact, the pore geometry observed by μ-CT revealed a transverse isotropy of the material microstructure whose principal direction coincided with the foaming processing. Therefore, the macroscopic mechanical properties might also exhibit a transverse symmetry. However, the samples were tested only along the cylindrical axis that corresponded with the first principal direction. Indeed, the choice of cylindrical samples that permitted an axisymmetry boundary condition and eased the impregnation process, made it difficult to test the mechanical behavior in the transverse direction. Consequently, the values reported in table 3.1 are representative of the first principal direction only and dedicated tests are still needed to assess the severity of the sample anisotropy.

Finally, the physical parameters of the loaded group were not significantly different from the control group and at any point in time (see Figure 3.15). In addition, no aging of the material was observed as the physical parameters stayed constant throughout the 24 days of experiment. Furthermore, the plasticity observed on the loaded samples (see Figure 3.12) did not impact the physical parameters describing the samples.

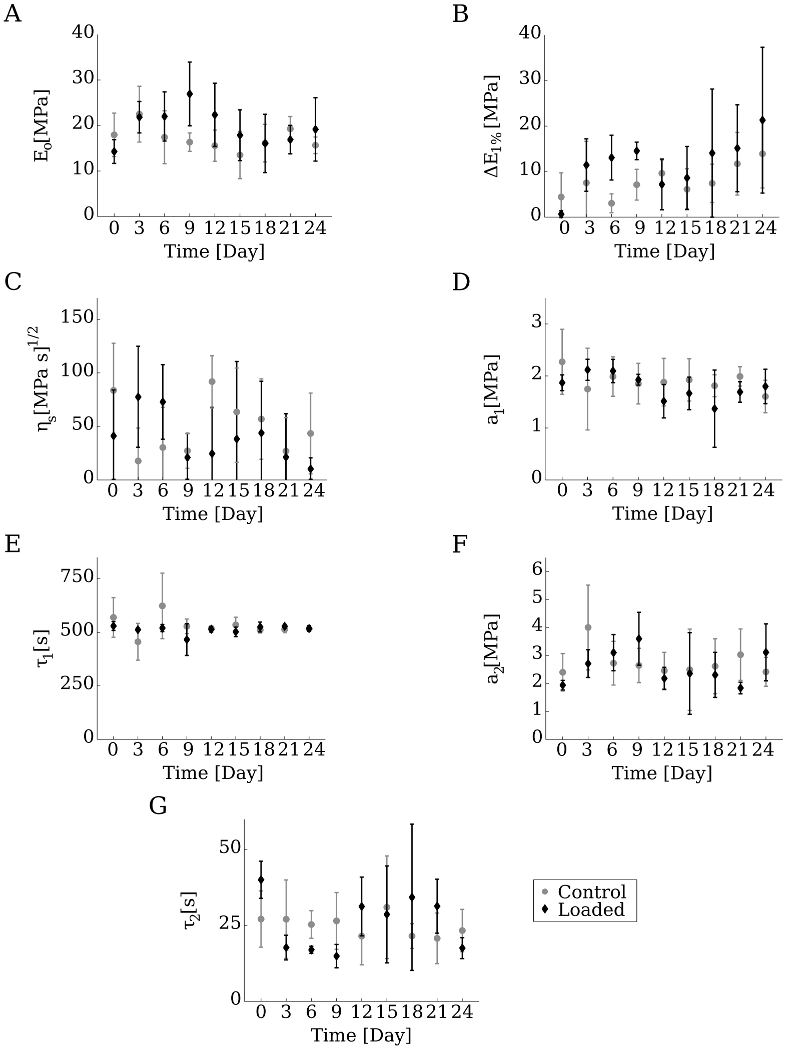

Figure 3.15: Evolution of the viscoelastic parameters during a period of 24 days, averaged on four samples of the loaded and control group. (A) elastic modulus at zero strain; (B) elastic hardening at 1% strain; (C) viscous hardening; (D) Long term relaxation; (E) Long term time constant; (F) Intermediate term relaxation; (G) Intermediate term time constant.

3.3.3 Conclusions

The mechanical tests carried out on the PLLA-5%βTCP foam samples showed that this material could resist at least 170'000 compression cycles of 0-0.4 MPa applied at 1 Hz. The number of cycles decreased to about 3'000 cycles when a dynamic compression amplitude of 0-1 MPa was applied. From a clinical perspective, the new porous polymer should be used in applications where the applied compression is smaller than 0.4 MPa.

A continuum mechanical model was developed to characterize the mechanical behavior of PLLA-5%βTCP foam constructs. A viscoelastic constitutive law was identified that took into account thermodynamical restrictions and stability requirements. The 7 viscoelastic parameters of the constitutive law were then computed by fitting the theoretical law to experimental data using least-square optimization algorithm. The proposed viscoelastic law accurately described the constructs mechanical behavior as the correlation coefficients between experiment and theory were higher than 0.95 for all samples, regardless of their loading history.

No aging phenomenon could be detected during the 24 days of experiments. Indeed, the samples submitted to intermittent dynamic compression during 24 days exhibited similar viscoelastic parameters to unloaded samples. Despite a large variation of the strain rate dependent stiffening (or short term memory effect), the average elastic and long term viscous properties appeared to be stable over 24 days. In addition, the samples were found to settle at an average rate of 0.2%/day due to repeated dynamic loading. Finally, the average parameters of table 3.1 together with the constitutive law (3.35) describe the viscoelastic behaviour of PLLA-5%βTCP foams submitted to compression load lower than 0.4 MPa.

Table 3.1: Average viscoelastic parameters computed from data obtained from 8 samples and 9 time points ($n = 72$).

Parameter	Symbol	Value
Elastic modulus at zero strain	E_0	18 ± 6.0 MPa
Elastic hardening at 1% strain	$\Delta E_{1\%}$	9.8 ± 8.8 MPa
Viscous hardening	η_s	$44 \pm 46 \sqrt{\text{MPa s}}$
Long term relaxation	a_1	1.8 ± 0.4 MPa
Long term time constant	τ_1	520 ± 62 s
Intermediate term relaxation	a_2	2.6 ± 1.0 MPa
Intermediate term time constant	τ_2	25 ± 12 s

3.4 Fluid Motion in PLLA Bone Construct

The constitutive law presented in the previous section is a useful and accurate model for the description of the construct when considered as a bulk material. However, the presence of fluid inside the porous construct is essential for the biomechanics of the construct. Indeed, the fluid transports wastes, nutriments, biochemical signals and cells throughout the constructs which promotes construct osteoinduction and osteogenesis [110, 159, 190]. Fluid motion also exerts a mechanical stress on the cells attached to the porous construct. This stress, when its magnitude is between 0.01 and 3.5 Pa [10, 31, 47, 61, 80, 87, 90, 132, 150, 169, 181, 193, 200], might further enhance the production by the cells of osteogenic proteins.

Nutriments, wastes and biochemical signals appears to be transported by advection rather than diffusion or dispersion. Indeed, the *Peclet number Pe* which is the ratio of the advection forces to the diffusion and dispersive forces [11] is found to be much larger than 1 in the particular case of PLLA construct and cancellous bone.

$$Pe = \frac{L_c V_c}{D_{eff,c}} \sim 8 \cdot 10^5 \gg 1$$

L_c is the characteristic length taken as the construct radius (15 mm), V_c is the characteristic fluid velocity (0.1 mm/s) and $D_{eff,c}$ is the characteristic effective diffusion and dispersion coefficient[5] for bovine serum albumine in porous structure ($1.8 \cdot 10^{-12}$ m^2/s) [196]. Consequently, diffusion and dispersion are disregarded in the following discussion.

In a continuum approach, there are several ways to model the fluid motion inside a porous medium due to mechanical loads. Three methods may be used: the homogenization method [74], the averaging method on a representative elementary volume (REV) [11] and the continuum mechanics applied to porous media [39]. The first two methods start at a microscopic level and either by asymptotic or averaging (or smoothing) methods give a macroscopic description of the media. They present the advantage that macroscopic effects may be traced back to microscopic phenomenon and *vice versa*. However, numerous assumptions are required to obtain usable macroscopic equations. Nevertheless, these methods have been applied successfully to numerous domains including fluid motion in bone [180], double diffusion and growing poroelastic medium [168] or porous media with n-wetting-phases [11].

The continuum approach is built on the first and second thermodynamic principles. The major advantage of such an approach is that fundamental thermodynamic principles are fulfilled *a priory*. In addition, they define a general framework for the development of constitutive equations that may be especially useful for open systems such as porous media [39]. On the other hand, the current state of the continuum is described by macroscopic variables that have no meaning at microscopic length scale. In other words, the explicit link with the microscopic architecture is lost. However, this link may be searched *a posteriori* for a parameter of interest with help of the averaging method. In particular, the averaged shear stress exerted by the fluid motion relative to the solid skeleton may be retrieved from Darcy's law (see Appendix C).

Although the continuum approach of porous material is similar to classical solid mechanics, some important differences exist. It is thus necessary to review the kinematics, dynamics and thermodynamics of porous media whilst highlighting the changes from classical mechanics.

---

[5] The diffusion coefficient taking into account dispersion in porous media is defined as: $D_{eff} = \frac{D}{T}$, where T is the tortuosity defined by (C.3)

3.4.1 Continuum Mechanics of Porous Media

A linear theory of porous media was first proposed by Biot [13] who extended the Terzaghi work on one dimensional settlement of soil column [186]. Later, Coussy [39] formulated a more general approach of porous media in a thermodynamically consistent framework. This later approach is adopted in the following discussion.

Kinematics

The basic concept of continuum porous mechanics is to superimpose in space and time two continua that represent the fluid and the solid phases. The kinematics of the porous media is legitimately given by the solid skeleton kinematics which is identical to the classical solid continuum mechanics discussed briefly in section 3.3.2. On the other hand, the fluid kinematics does not correspond to the skeleton kinematics but is associated with the skeleton particle. Therefore, special derivative rules have to be introduced to capture the material derivative of fields associated with the fluid but identified by skeleton particles [39]. The kinematics of the fluid particles is thus related to the skeleton particles. The fluid mass flux is given in Euler variables by

$$\mathbf{q}_t(\mathbf{y},t) = \rho^f \phi \mathbf{v}^r \tag{3.36}$$

where $\mathbf{v}^r(\mathbf{y},t)$ is the fluid velocity relative to the skeleton motion and ϕ is the construct porosity. The corresponding Lagrangian fluid mass flux is

$$\mathbf{q}(\mathbf{x},t) = J\mathbf{F}^{-1}\mathbf{q}_t \ , \tag{3.37}$$

where J is the Jacobean of the deformation gradient $\mathbf{F}$. Note that $\mathbf{q}$ is not linked to the actual fluid particle velocity that was located in $\mathbf{x}$ in the reference configuration as the description is related to a skeleton particle. Finally, the absolute fluid acceleration at time t in Euler variables is derived from the fluid relative velocity.

$$\mathbf{a}^f(\mathbf{y},t) = \frac{\partial \mathbf{v}}{\partial t} + \mathbf{v}\nabla\mathbf{v} \tag{3.38}$$

Where, $\mathbf{v} = \dot{\mathbf{y}} + \mathbf{v}^r$.

Dynamics

Classical solid continuum dynamics have to be rewritten to take into account the forces relative to the fluid motion. The mass balance and momentum balance equation of a fully saturated porous media are summarized hereafter.

Balance of Mass First, it is assumed that there is no creation of mass within the solid skeleton and that no exchange of mass is taking place between the solid and fluid phases. Consequently, the local fluid mass balance in Lagrange variables simplifies to [39,40]

$$\frac{\partial m}{\partial t} + \nabla \cdot \mathbf{q} = 0 \qquad m = J\rho^f \phi - \rho_0^f \phi_0 \ , \tag{3.39}$$

where m is the fluid mass per initial unit volume that is exchanged with the outside (>0 if mass added, <0 if mass extracted) and ϕ_0 is the reference porosity. Mass balance applied to the porous media as a whole gives in Lagrange variables

$$\frac{\partial}{\partial t}\left(J\rho^{tot}\right)+\nabla\cdot\mathbf{q}=0\ , \tag{3.40}$$

where ρ^{tot} is the present bulk mass density given by $\rho^{tot}=(1-\phi)\rho^s+\phi\rho^f$. From the fluid and the bulk mass balance equations (3.39,3.40), the skeleton mass balance may be calculated which gives a relation between the actual and reference (index $_0$) porosity and skeleton mass density

$$J\rho^s(1-\phi)=\rho_0^s(1-\phi_0)\ . \tag{3.41}$$

Balance of Linear Momentum The local balance of linear momentum of a saturated porous medium considered as a whole is given in Lagrange variables by [40]

$$(1-\phi_0)\rho_0^s\ddot{\mathbf{u}}+(m+\phi_0\rho_0^f)\mathbf{a}^f-\nabla\cdot\mathbf{P}-(\rho_0^{tot}+m)\mathbf{f}=0\ . \tag{3.42}$$

where $\mathbf{P}$ is the total Piola-Kirchhoff I stress tensor, $\mathbf{f}$ is the vector field of external volumetric forces applied to the porous medium and $\mathbf{a}^f$ is the absolute fluid acceleration[6]. The linear momentum balance equations for porous media (3.42) have a similar structure to the classical solid mechanics balance equations (3.11). However, new terms have appeared to take into account the fluid inertia and mass variation due to fluid exchange with the environment. It is important to note that the Piola-Kirchhoff I stress tensor in equation (3.42) represents the sum of the the fluid pressure and of the stresses due to the solid skeleton deformation.

Balance of Angular Momentum The balance of angular momentum is given in Lagrange variables by the following local equation

$$\mathbf{y}\times\left[(1-\phi_0)\rho_0^s\ddot{\mathbf{u}}+(m+\phi_0\rho_0^f)\mathbf{a}^f-\nabla\cdot\mathbf{P}-(\rho_0^{tot}+m)\mathbf{f}\right]-\frac{1}{2}\left(\mathbf{F}\mathbf{P}^T-\mathbf{P}\mathbf{F}^T\right)=0 \tag{3.43}$$

Using the linear momentum balance equation (3.42), the above equation simplifies to

$$\mathbf{F}\mathbf{P}^T=\mathbf{P}\mathbf{F}^T\ . \tag{3.44}$$

Similarly to classical solid mechanics, the balance of angular momentum is equivalent to a symmetric Piola-Kirchhoff II stress tensor.

$$\mathbf{S}=\mathbf{S}^T\ . \tag{3.45}$$

---

[6] Note that the fluid absolute acceleration $\mathbf{a}^f$ may be expressed in Lagrange variable as

$$\mathbf{a}^f(\mathbf{x},t)=\ddot{\mathbf{u}}+\frac{\partial}{\partial t}\left(\frac{\mathbf{F}\mathbf{q}}{m+\phi_0\rho_0^f}\right)+\frac{\mathbf{q}}{m+\phi_0\rho_0^f}\left[\dot{\mathbf{F}}+\nabla\left(\frac{\mathbf{F}\mathbf{q}}{m+\phi_0\rho_0^f}\right)\right]\ .$$

Thermodynamics of Porous Media

The first and second thermodynamic principles provide additional equations and restrictions to the development of a constitutive law relating the dynamic quantities to the kinematic ones.

First Principle In the particular case of an isothermal processes, the local form of the first principle in Lagrange variables simplifies to

$$\dot{e}_v = \frac{1}{2}\mathbf{S} : \dot{\mathbf{C}} + \mathbf{q} \cdot \mathbf{F}^T \cdot (\mathbf{f} - \mathbf{a}_T^f) - \nabla \cdot \left[\left(e_m^f + \frac{p}{\rho^f} \right) \mathbf{q} \right] , \tag{3.46}$$

where e_v is the internal energy per unit volume, e_m^f is the fluid internal energy per unit fluid mass and p represents the fluid pressure. In comparison to the classical solid first principle given by equation (3.14), two additional terms have appeared due to the presence of fluid. The first term represents the fluid inertia power where $\mathbf{a}_T^f$ is the absolute fluid acceleration corrected to take into account the tortuosity effect (see Coussy *et al.* [39] for more details). The second term is the power brought (or extracted) by the fluid mass exchanged with the environment.

Second Principle The Clausius-Duhem inequality extended for porous media in an isothermal state is given by [39]

$$\Phi_1 + \Phi_2 \geq 0 , \tag{3.47}$$

where $\Phi_1$is the intrinsic volume dissipation and Φ_2 is the dissipation due to fluid mass transport. The intrinsic volume dissipation may be written in Lagrange variables as

$$\Phi_1 = \frac{1}{2}\mathbf{S} : \dot{\mathbf{C}} + g_m \frac{\partial m}{\partial t} - \frac{\partial \Psi}{\partial t} \tag{3.48}$$

where g_m is the fluid mass free enthalpy and Ψ the volume free energy. The dissipation due to fluid mass transport is given by

$$\Phi_2 = \frac{\mathbf{q}}{\rho^f} \left[-\nabla p + \rho^f \mathbf{F}^T \left(\mathbf{f} - \mathbf{a}_T^f \right) \right] . \tag{3.49}$$

Fluid Conduction Law Although not required by the Clausius-Duhem inequality (3.47), both dissipation Φ_1 and Φ_2 may be assumed to be greater or equal to zero.

$$\Phi_1 \geq 0 , \qquad \Phi_2 \geq 0 \tag{3.50}$$

Similarly to the viscoelastic law identification, the above assumption restricts the set of constitutive equations. However, it greatly simplifies its derivation.

The dissipation due to the fluid mass transport Φ_2 of equation (3.49) is a product of a force and a flux. Consequently, the simplest conduction law that fulfills the positivity of Φ_2 linearly relates the force to the flux, which yields the generalized Darcy's Law in Lagrange variables

$$\frac{\mathbf{q}(\mathbf{x},t)}{\rho^f} = \mathbf{K} \left[-\nabla p + \rho^f \mathbf{F}^T \left(\mathbf{f} - \mathbf{a}_T^f \right) \right] , \tag{3.51}$$

where $\mathbf{K}$ is the Lagrangian permeability and is related to the Eulerian permeability by $\mathbf{K}_t = J\mathbf{F}^{-1}\mathbf{K}\mathbf{F}^{-T}$.

State Equations According to the local state postulate, the density of free energy is expressed by

$$\Psi = \Psi(\mathbf{C}, m, \chi_1, \chi_2, .., \chi_n) \tag{3.52}$$

where χ_i are some additional internal variables that are required for the description of the continuum. In addition, the set of variable $(\mathbf{C}, m)$ constitutes a normal set of variables. Since the inequality $\Phi_1 \geq 0$ must always be satisfied, the following state equations are obtained

$$\mathbf{S} = \frac{\partial \Psi}{\partial \mathbf{C}} \qquad g_m^f = \frac{\partial \Psi}{\partial m} \; . \tag{3.53}$$

Therefore, when the density of free energy is described only by the external variables **C** and *m*, the dissipation is always equal to zero. The material is then called *poroelastic* and Clausius-Duhem is fulfilled.

Linear Poroelasticity

Similarly to the approach used in section 3.3.2, a specific form of the free energy function may be postulated from which the state equations are then derived. The free energy function describing Biot's linear poroelasticity is a second order development of $\Psi(\mathbf{C}, m)$ which assumes small pore pressure perturbation and small solid skeleton deformation. The classical expression is given as a function of **E** rather than **C** and is reproduced hereafter.

$$\Psi = tr(\mathbf{S}_0^T \mathbf{E}) + g_{m,0} m + \frac{\lambda_u}{2} tr^2(\mathbf{E}) + \mu tr(\mathbf{E}^2) - \frac{m}{\rho_0^f} M b tr(\mathbf{E}) + \frac{1}{2} M \left(\frac{m}{\rho_0^f} \right)^2 \; , \tag{3.54}$$

where $\mathbf{S}_0$ and $g_{m,0}$ are respectively the stress and mass enthalpy in the reference configuration. The constant *M* denotes the so called Biot's modulus and *b* is the Biot's coefficient. The undrained Lamé coefficients are identified by the letters λ_u and μ. The fluid enthalpy is classically given for an isothermal process by

$$g_m = g_m(p) \qquad \frac{1}{\rho^f} = \frac{\partial g_m}{\partial p} \; . \tag{3.55}$$

A first order development in *p* of the fluid free enthalpy gives

$$g_m = g_{m,0} + \frac{p - p_0}{\rho_0^f} \; . \tag{3.56}$$

Using equation (3.56) together with the state equations (3.53) yields Biot's equation for linear poroelastic materials.

$$\begin{aligned} \mathbf{S} \; &= \mathbf{S}_0 + \lambda_u tr(\mathbf{E})\mathbf{I} + 2\mu \mathbf{E} - bM \frac{m}{\rho_0^f} \mathbf{I} \\ p \; &= p_0 + M \left(-btr\mathbf{E} + \frac{m}{\rho_0^f} \right) \end{aligned} \tag{3.57}$$

The physical linearization postulated in equation (3.54) requires that the variation of stresses $-bM\frac{m}{\rho_0^f}$ and of pressure $M\frac{m}{\rho_0^f}$ due to the variation of fluid mass exchange *m* are smaller than the variation of stress and pressure due to the solid skeleton deformation [39].

Finally, using the second equations of (3.57) with the first equation gives another form of the skeleton constitutive equation which relates the total stress to the strain and the pore pressure p.

$$\mathbf{S} = \mathbf{S}_0 + \lambda tr(\mathbf{E})\mathbf{I} + 2\mu\mathbf{E} - b(p - p_0)\mathbf{I} \tag{3.58}$$

The drained Lamé coefficient λ is defined as $\lambda = \lambda_u - Mb^2$. The Clausius-Duhem inequality (3.47) together with stability condition requires that [39]

$$M > 0\,, \qquad 3\lambda + 2\mu > 0\,, \qquad \mu > 0\,, \tag{3.59}$$

or in terms of the drained elastic modulus and the drained Poisson's ratio

$$M > 0\,, \qquad E > 0\,, \qquad -1 < \nu < 1/2\,. \tag{3.60}$$

3.4.2 Fluid Motion in a Cylindrical Sample

The equation system formed by the constitutive laws (3.58), the mass and momentum balance equations (3.39, 3.42) and Darcy's law (3.51) was solved for a cylindrical sample of radius R and height H under axial dynamic compression $F(t)$ (see Figure 3.16). The sample was assumed to have homogeneous properties which were the drained Lamé constant λ, μ and the intrinsic isotropic permeability k for the solid skeleton. The saturating fluid was assumed to be Newtonian with a viscosity η and mass density ρ^f. Finally, coefficients describing the fluid/solid system were Biot's modulus M and Biot's coefficient b.

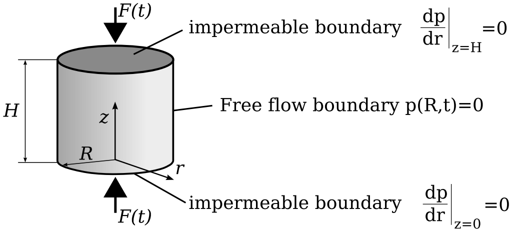
F(t)
impermeable boundary $\left.\frac{dp}{dr}\right|_{z=H}=0$
H
z
Free flow boundary p(R,t)=0
R
r
impermeable boundary $\left.\frac{dp}{dr}\right|_{z=0}=0$
F(t)

Figure 3.16: Boundary conditions of the poroelastic problem.

The sample's upper and lower boundaries were considered impermeable and a free flow condition was assumed at the sample outer edge. In addition, vertical displacements were blocked at the sample bottom but radial displacements were allowed. The stress condition at the upper edge specified that the integral over the cylinder top surface of the total axial stress was equal to the applied force. Finally, the sample was assumed to be undeformed and stress-free in the initial state (at $t = 0$).

Small deformations and axisymmetry were assumed together with the following hypothesis for the solid skeleton deformation and fluid pressure expressions

$$\mathbf{u} = u(r,t)\mathbf{e}_r + w(z,t)\mathbf{e}_z \qquad \text{and} \qquad p = p(r,t)\,. \tag{3.61}$$

The inertial loads were neglected and the external body forces were assumed to be zero. Using the constitutive equation (3.58) together with the momentum balance equation (3.42) obtains the reduced solid skeleton equations of motion.

$$-(\lambda+\mu)\nabla(\nabla\cdot\mathbf{u})-\mu\nabla^2\mathbf{u}+b\nabla p=0 \tag{3.62}$$

The fluid equation of motion was obtained by combining the fluid mass balance equation (3.39), Darcy's law (3.51) and the fluid constitutive equation (3.57).

$$\frac{\eta}{kM}\frac{\partial p}{\partial t}+\frac{\eta b}{k}\frac{\partial}{\partial t}\nabla\cdot\mathbf{u}=\nabla^2 p \tag{3.63}$$

The system composed of equations (3.62) and (3.63) was solved for the boundary problem portrayed in Figure 3.16. The detailed dderivatioderivation for analytical resolution of this poroelastic problem is reported in appendix B. The general results are recalled hereafter

$$p_{tot}(r,t)-p_0=\sum_{n=1}^{\infty}p_n(t)J_0(k_n r) \tag{3.64}$$

where J_0 is the J-Bessel function of order 0, and p_n are the n-th components of the vector $\mathbf{p}$. The fluid velocity relative to the solid skeleton was computed using Darcy's law and the above result.

$$v^r(r,t)=\frac{k}{\eta\phi}\sum_{n=1}^{\infty}p_n(t)\frac{J_1(k_n r)}{k_n}\ , \tag{3.65}$$

where ϕ is the current porosity defined by the skeleton mass balance equation (3.41). In the case of an incompressible skeleton, the current porosity is given by

$$\phi=1-\frac{1-\phi_0}{J}\ . \tag{3.66}$$

Finally, the averaged shear stress induced by the motion of the fluid relative to the solid skeleton was derived from averaging theory applied to a two phase poroelastic medium[7]

$$\bar{\tau}=\frac{\eta}{k}\frac{\phi\phi^S}{\Sigma_{fs}}v^r\ , \tag{3.67}$$

where ϕ^S is the surface porosity and Σ_{fs} is the specific contact area between the fluid and the solid. Like the volume porosity, the surface porosity ϕ^S is dependent on the porous medium deformation. Assuming an incompressible solid skeleton, the current surface porosity in the plane defined by the normal vector $\mathbf{n}$ is given by

$$\phi^S=1-\frac{1-\phi_0^S}{\parallel J\mathbf{F}^{-T}\mathbf{n}\parallel}\ . \tag{3.68}$$

---

[7] See Appendix C for a detailed derivation of the average fluid-induced shear stress.

3.4.3 Application to a PLLA-5%βTCP Construct

The general solutions (3.64) and (3.65) were applied to the particular case of a PLLA-5%βTCP construct saturated with culture medium and stimulated mechanically by a dynamic compressive force. A total peak compression force of 50 N was applied to the sample top which corresponded to a homogeneous stress of 1 MPa over the entire sample top. By doing so, the computed value could be viewed as normalized values per unit MPa loading. Indeed, linearity between the applied force and the total stress as well as the pore pressure was computed in this configuration for compression stresses lower than 20 MPa.

The physical parameters used for the computation of the poroelastic problem are shown in table 3.2. These parameters were either determined experimentally or estimated from existing published data. In particular, the culture medium density and compressibility were assumed to be similar to those of water at room temperature. Consequently, the mass density was assumed to be 1000 kg/m^3 and the compressibility 3.2 GPa [134]. The solid skeleton was assumed incompressible with respect to the bulk volume compressibility. Indeed, the bulk elastic modulus of PLLA is about 9 GPa which is much greater than the bulk volume stiffness measured to be about 20 MPa. As a result, Biot's coefficient was assumed to be equal to one meaning that the fluid pressure does not locally deform the solid skeleton. Finally, a value of 0.3 was assumed for the Poisson's ratio which is the averaged value reported by Gibson and Ashby for open pore polymer foams [60].

Table 3.2: Baseline configuration of PLLA-5%βTCP construct.

Physical parameter	Symbol	Value
Drained elastic modulus	E	20 ± 6 MPa
Poisson's ratio	ν	0.3
Intrinsic permeability	k	$7.6 \pm 4 \cdot 10^{-12}$ m^2
Porosity	ϕ	78 ± 3 %
Surface porosity	ϕ^S	29 ± 3 %
Specific area	Σ_{fs}	27 ± 1 mm^{-1}
Culture medium viscosity	η	$1.2 \pm 0.3 \cdot 10^{-3}$ Pa· s
Culture medium density	ρ^f	1000 kg/m^3
Culture medium compressibility	K_s	3.2 GPa

All the other parameters were determined experimentally. The methods used as well as the final results are summarized in the following paragraphs.

Drained Elastic Modulus The drained elastic modulus E was determined by fitting the linear poroelastic law (3.57) to the compression test at a deformation rate of 0.008 mm/s (see section 3.3.1). An averaged linear elastic modulus of $E = 20 \pm 6$ MPa was computed based on 72 measurements. The correlation coefficients between the fitted curves and the experimental data were greater than 0.93.

Intrinsic Permeability Experimental determination of the intrinsic permeability was carried out on an existing test bench from the Laboratory of Composite and Polymer Technology at EPFL and was adapted for 8 mm constructs. In short, one porous sample was confined in an adjusted silicon tube (Masterflex AG, Gelsenkirchen, Germany) and tightened radially by a ring clamp. A water flow was generated through the sample by an injection unit (Plastech T.T. Ltd, Cornwall, UK). The pressure adjacent to the sample was measured by an accurate pressure sensor which permitted the pressure drop due to the sample to be calculated by subtracting the initial pressure from the pressure measured during the application of fluid flow. Finally, the average flow rate was determined by measuring the water volume that was collected in a graduated Becher as a function of the time measured with a stopwatch.

The applied flow rates were chosen so that the following condition was fulfilled for every sample

$$Re\sqrt{Da} \ll 1 \;, \qquad St \leq 1 \tag{3.69}$$

where *Re* is the Reynolds number, *Da* is Darcy's number and *St* is the Strouhal's number which were given by the following expressions for this particular test configuration

$$Re\sqrt{Da} = \frac{\dot{V}}{A}\frac{\rho^f \phi}{\eta \Sigma_{fs}}\left(\frac{\phi}{\Sigma_{fs} R}\right) \simeq 0.01 \ll 1 \;, \qquad St = \frac{fRA}{\dot{V}} \simeq 0.0 \leq 1 \;.$$

Indeed, the Reynolds number was always smaller than 2 and the Darcy's number was smaller than $5 \cdot 10^{-5}$. In addition, the Strouhal number was zero as the fluid flow across the sample was kept constant. As a result, the intrinsic permeability could be computed for each sample and each flow rate from the Darcy's law as

$$k = \eta \frac{\dot{V}}{A}\frac{H}{\Delta p} \;, \tag{3.70}$$

where $\dot{V}$ is the volume rate of water that flowed across the sample section A. The water viscosity η at 20°C was assumed to be 1.0 mPa·s [108], and Δp is the hydrodynamic resistance across the sample height H.

The permeability tests were conducted for 12 different samples and at 4 different flow rates for each sample which represents 48 measurements. In addition, permeability tests were carried out before and after the mechanical stimulation which were found to induce no significant permeability change. Moreover, the stimulated samples exhibited permeability values similar to the unloaded sample. Therefore, an averaged intrinsic permeability of $k = 7.6 \pm 4 \cdot 10^{-12}$ m^2 could be used for the poroelastic computations.

Porosities and Specific Contact Area The volume porosity ϕ, specific contact area Σ_{fs} and surface porosity ϕ^S were computed from μ-CT images (Scanco Medical AG, Bassersdorf, Switzerland) of five different PLLA-5%βTCP constructs. A dedicated algorithm [68] was applied to compute different morphometric parameters including the volume porosity and the specific area. The surface porosity was computed on individual μ-CT images by applying thresholds and pixel counting algorithms. The averaged values were *(i)* volume porosity: 78 ± 3 %; *(ii)* surface porosity: 29 ± 3 %; *(iii)* specific contact area 27 ± 1 mm^{-1}.

Culture Medium Viscosity The culture medium viscosity was measured at room temperature using standard concentric Couette cylinders [38]. Its principle is to measure the shear stress transmitted by the culture medium from an inner rotating cylinder to an outer static cylinder. The measurements were done on a commercial rheometer (TA Instruments, Leatherhead, UK) at different shear strain rates. The culture medium had a constant viscosity of 1.2 ± 0.3 mPa·s for strain rate larger than 10%/s which is similar to water viscosity.

3.4.4 Results

An harmonic compression load applied at 1 Hz and with a peak force equivalent to an average stress of 1 MPa induced a maximal pressure difference of about 40 Pa within a 8 mm diameter construct (see Figure 3.17). The maximal pore pressure was located at the construct axis of symmetry and its magnitude oscillated at the same frequency as the compression load but with a $\pi/2$ phase shift. The transient pore pressure was computed to have a negligible magnitude and vanished after a characteristic time of 23 μs. In conclusion, the resistance due to the fluid did not play a significant role in the overall mechanical response of the construct.

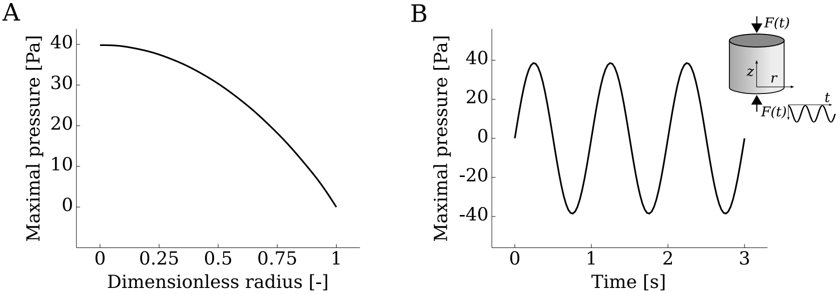

Figure 3.17: (A) The maximal pore pressure profile as a function of the construct radius. (B) The maximal pore pressure, i.e. at the center of the sample, as a function of time.

According to Darcy's law, pressure difference induces a fluid motion. As a result, fluid was expelled from the construct during the compression phase and fluid was sucked into the construct during compression release. The total fluid volume that was exchanged with the environment at each cycle was equal to 3.7% of the total fluid content.

The relative motion between the fluid and the solid skeleton induced a shear stress between the two media. The fluid-induced shear stress was maximal at the construct periphery and zero at its symmetry axis (see Figure 3.18). The maximal fluid induced shear stress at the construct periphery was computed to be equal to 0.16 Pa and oscillated at the same frequency as the applied force with a $\pi/2$ phase shift.

The impact of each construct physical parameter on the fluid volume exchange and on the fluid-induced shear stress was computed and is discussed in the following paragraphs.

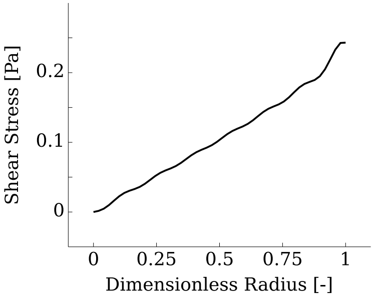

Figure 3.18: Fluid-induced shear stress across the construct section at maximal fluid velocity.

Stiffness Effect

The construct bulk elastic modulus had an important impact on the fluid dynamic inside the porous construct. On one hand, compliant constructs induced the transport of a large fluid volume across the construct which generated large fluid-induced shear stresses (see Figure 3.19). For instance a construct with a bulk elastic modulus of 5 MPa exchanged 16% of its fluid volume during one cycle which induced a maximal shear stress of 1.0 Pa. On the other hand, a stiff construct deformed less which induced a small fluid volume transport. As a result, small shear stresses were generated at the fluid/solid skeleton interface.

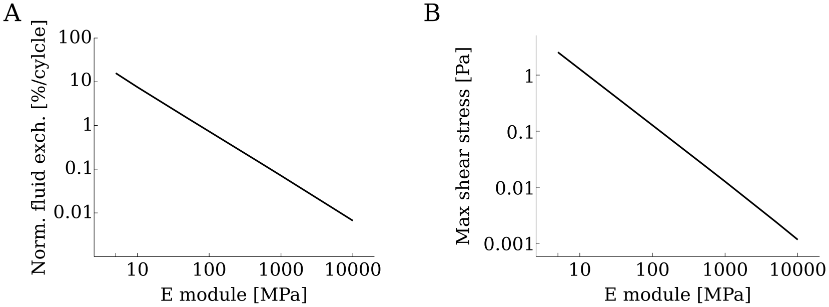

Figure 3.19: Effects of the construct elastic modulus on (A) the fluid proportion exchanged with the environment during one cycle and (B) on the maximal fluid-induced shear stress.

Fluid Viscosity Effect

The fluid viscosity had little impact on the fluid exchange between the construct and the environment. Indeed, a fluid viscosity increase of 4 orders of magnitude from $1.2{\cdot}10^{-4}$ to 1.2

Pa·s induced an increase in the fluid volume exchange of only 5%. On the other hand, the fluid-induced shear stress was directly proportional to the fluid viscosity.

Permeability Effect

Similarly to the effect of fluid viscosity, the intrinsic permeability did not impacted volume of fluid exchanged with the construct environment. The volume of fluid exchanged stayed unchanged over a 1'000-fold increase of the intrinsic permeability. On the other hand, the fluid-induced shear stress was inversely proportional to the intrinsic permeability. In other words, a 10-fold increase of the intrinsic permeability induced a 10-fold decrease of the fluid-induced shear stress.

Poisson Ratio Effect

The Poisson's ratio impacted both the fluid volume exchange and the fluid-induced shear stress. For an incompressible construct, i.e. $\nu = 0.5$, the fluid exchange and the fluid induced shear stress were zero. The fluid volume exchange increased with decreasing Poisson's ratio and reached 10% of the total construct fluid volume for a Poisson's ratio equal to zero (see Figure 3.20). The shear stress also increased with decreasing Poisson's ratio, and reached a value of 0.64 Pa for $\nu = 0$.

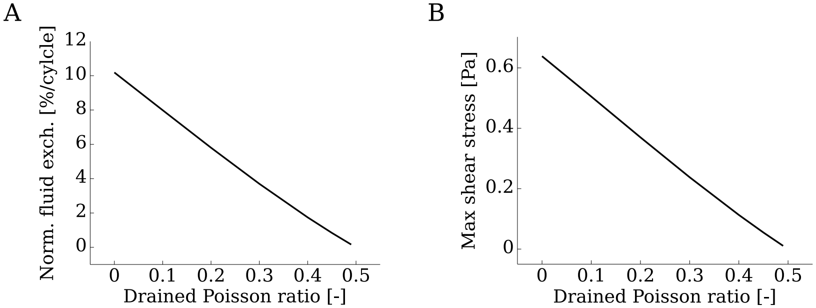

Figure 3.20: Effects of the construct's Poisson ratio on (A) the fluid proportion exchanged with the environment during one cycle and (B) on the maximal fluid-induced shear stress.

Excitation Frequency Effect

The excitation frequency had no impact on the volume exchange per cycle with the environment. However, as the number of cycles per unit time was proportional to the frequency, the volume of fluid exchanged per unit time was proportional to the excitation frequency. Therefore, the fluid-induced shear stress was directly proportional to the excitation frequency.

It should be remembered that the fluid conductivity was assumed to be governed by Darcy's law whose domain of validity is defined by condition (3.69). In particular, the Strouhal's number limits the domain of the excitation frequency to

$$f_{max} \leq \frac{v_{max}}{R} \,. \tag{3.71}$$

For the particular configuration defined in table 3.2, the maximal excitation frequency was about 130 Hz.

Porosity Effect

The porosity at constant permeability and constant stiffness had no effect on the fluid induced shear stress. On the other hand, increasing construct porosity induced a small decrease of the proportion of fluid that was exchanged with the environment (see Figure 3.21). For instance, a construct with an open pore porosity of 60% exchanged 6.4% of its total fluid volume in one cycle whereas a construct with a porosity of 90% exchanged only 2.7% of its fluid.

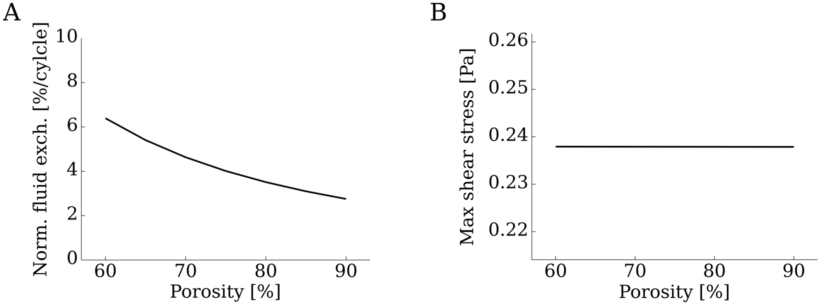

Figure 3.21: Effects of the construct porosity at constant permeability and constant construct stiffness on (A) the fluid proportion exchanged with the environment during one cycle and (B) on the maximal fluid-induced shear stress.

In the above considerations, the porosity was considered independently of its effect on the construct stiffness. To study the impact of the porosity on the fluid motion inside a construct which solid skeleton is made of the same material, a relation between the porosity and the construct stiffness must be introduced. For open pore foams and for the cancellous bone of long bones, a quadratic relation between the overall foam stiffness and the porosity was proposed [60,154].

$$E = E_0(1-\phi)^2 \tag{3.72}$$

Using this relation, the fluid volume exchange and fluid-induced shear stress was computed to increase with increasing porosity (see Figure 3.22). For instance, the fluid volume exchange would increase from 1.9% to 14% when the porosity of the same porous material increases from 60% to 90%. This is due to the large decrease in the construct stiffness that passes from 66 MPa at 60% porosity to 4.1 MPa at 90% porosity.

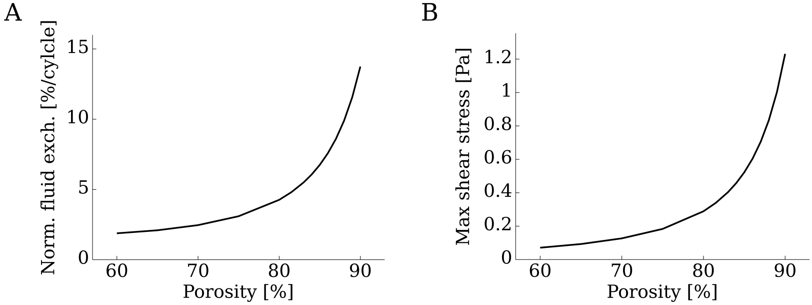

Figure 3.22: Effects of the construct porosity taking into account construct stiffening on (A) the fluid proportion exchanged with the environment during one cycle and (B) on the maximal fluid-induced shear stress.

Radius Effect

The construct radius had little effect on the fluid volume exchange with its environment (see Figure 3.23). A small sample of 1 mm radius exchanged 3.8% of its total volume with the environment whereas a sample with a radius 20-fold larger exchanged 3.3% of its total fluid content. On the other hand, the maximal fluid-induced shear stress increased with increasing sample radius. A 20-fold increase of the construct radius from 1 to 20 mm was computed to induce a 17-fold increase in maximal shear stress peaking at 1.1 Pa for the largest construct.

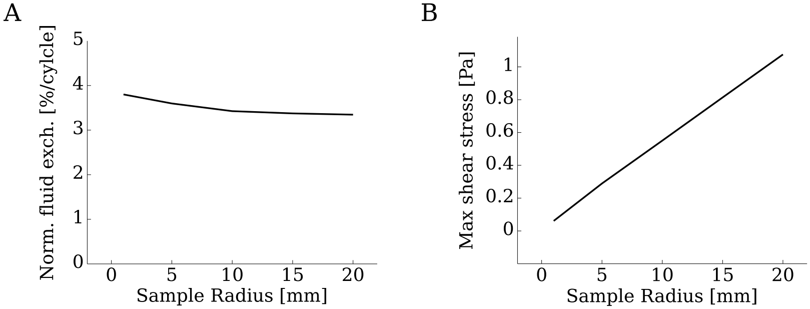

Figure 3.23: Effect of the construct radius on (A) the fluid proportion exchanged with the environment during one cycle and (B) on the maximal fluid-induced shear stress.

3.4.5 Discussion on Fluid Motion

Linear poroelastic theory applied to a PLLA-5%βTCP construct showed that the fluid contribution to the construct stiffness was negligible. Indeed, the pore pressure was computed to be 25'000-fold smaller than the average stress applied on the construct surface. In addition, the characteristic time for fluid relaxation was computed to be about 20 μs which clearly indicated that the viscoelastic behavior observed and modeled in the section 3.3 was intrinsic to the solid skeleton and not due to the fluid motion inside the construct.

The fluid motion was computed to be sufficient to exchange waste, nutriment, biochemicals and cells between the construct and its environment. It was found that 3.7% of the total fluid volume enclosed in the construct was expelled and sucked in during each compression cycle of 1 MPa peak stress applied at 1 Hz. Recalling from section 3.3.1 that the construct could support long term dynamic loading of 0.4 MPa peak stress, the equivalent of the total fluid volume entrapped in the construct was exchanged with the environment after less than 70 cycles (1 minute 10 seconds). Although the fluid exchange took place at the construct periphery it may initiate and favor construct colonization by transporting the host mesenchymal cells by advection inside the construct.

The fluid motion has not only an advective role but might also stimulate the bone cells embedded in the porous construct. It is known that fluid-induced shear stress between 0.01 to 3.5 Pa stimulates the activity of osteoblasts in 2D [31, 83, 87, 90, 132, 150, 193, 200] and 3D [61, 169] culture *in vitro*. In the particular case of PLLA-5%βTCP construct saturated by a culture medium, the fluid motion due to dynamic mechanical compression of 0-0.4 MPa at 1 Hz was computed to exert shear stresses on the fluid/solid interface in the range of 0-0.08 Pa. Although the maximal shear stress magnitude is relatively low, it is likely that most of the embedded cells are experiencing an adequate mechanical stimulation to begin secreting growth factors and extra-cellular bone matrix.

Interestingly, the fluid viscosity was found to have negligible impact on the proportion of fluid exchanged but to have a proportional impact on the fluid-induced shear stress. In addition, the fluid viscosity is expected to increase within a short period of time after the implantation. Indeed, it is likely that the culture medium is gradually replaced by bone marrow and bone intertrabecular fluid that have a viscosity 10 to 100-fold greater than the culture medium [18, 113]. The fluid-induced shear stress would probably increase in the same proportion within the first weeks after implantation.

On a longer time scale, construct degradation and the ingrowth of newly formed bone would impact the construct permeability and overall stiffness. However, no data has been published concerning the mechanical and fluid conductivity evolutions of PLLA-5%βTCP foam loaded with fetal cells. Nevertheless, it is likely that a significant increase of stiffness and decrease of permeability takes place during six months post-operation.

It may thus be hypothesized that the fluid-induced shear stress may first increase during the first weeks after implantation due to the gradual replacement of the culture medium by the peri-implant viscous fluid. Then, the fluid induce shear stress and the fluid exchange between the construct and its environment would probably gradually decrease due to the synthesis of mineralized extra cellular matrix inside the construct.

The viscous effects intrinsic to the solid skeleton were not explicitly taken into account in the poroelastic model. However, they are likely to have an impact on the fluid motion inside the porous construct (see table 3.3). On one hand, the short term memory effect has a negative impact on the fluid volume exchange and on the fluid-induced shear stress as it has a stiffening effect. Indeed, stiffer porous materials were calculated to induce less fluid motion than compliant ones. On the other hand, the impact of long term memory is likely to increase the fluid volume exchange and fluid-induced shear stress because it tends to decrease the effective stiffness of the porous material. Accordingly, the net impact of the viscous short and long term memories on the fluid motion is dependent on their relative importance as they have opposing effects.

The parametric analysis carried out on the construct permitted the effects of each physical parameter on the fluid induced shear stress and the fluid volume exchanged between the construct and the environment to be identified. The synthesized view presented in table 3.3 leaded to an optimization flowchart that may be used for the development of new bone substitute whose goal is to maximize the fluid exchange and generate adequate fluid-induced shear stress (see Figure 3.24).

In a first iteration, the fluid volume exchange between the construct and its environment may be maximized by taking the minimal stiffness and Poisson's ratio within the range of values defined by the clinical application.

The construct porosity must also be as small as possible because it increases the proportion of fluid exchanged with the environment. However, the porosity impacts the construct's rate of resorption which should be chosen to achieve a total resorption within a duration of about one year. In addition, the solid skeleton bulk stiffness and the overall construct stiffness are related to the porosity [60]. Therefore a compromise in terms of the porosity will be needed to achieve an adequate resorption rate and overall construct stiffness.

Then, the fluid-induced shear stress may be optimized by choosing the appropriate permeability for a given range of fluid viscosity. At this stage, the fluid-induced shear stress has to be computed for the particular loading and boundary conditions that are dependent on the clinical application. A permeability value may than be targeted to obtain a maximal fluid-induced shear stress that falls within the range of 0.01 to 3.5 Pa. As the permeability and fluid viscosity have no impact on the fluid exchange, the optimum value found in the previous step stays unchanged.

Table 3.3: Synthesized view of the effect of several construct physical parameters on the fluid volume exchange and the fluid-induced shear stress. Bulk elastic modulus E, bulk Poisson's ratio ν, viscous short term memory V_{short},viscous long term memory V_{long}, fluid viscosity η, permeability k, porosity ϕ (without stiffening effect), excitation frequency f, sample radius R.

Symbols	$E \nearrow$	$\nu \nearrow$	$V_{\mathrm{short}} \nearrow$	$V_{\mathrm{long}} \nearrow$	$\eta \nearrow$	$k \nearrow$	$\phi \nearrow$	$f \nearrow$	$R \nearrow$
Fluid exchange	$\searrow$	$\searrow$	$\searrow$	$\nearrow$	$=$	$=$	$\searrow$	$\nearrow$	$\simeq$
Shear stress	$\searrow$	$\searrow$	$\searrow$	$\nearrow$	$\propto$[8] $\nearrow$	$\propto$[8] $\searrow$	$=$	$\nearrow$	$\nearrow$

---

[8] the symbol $\propto$ means dependence in a proportional manner

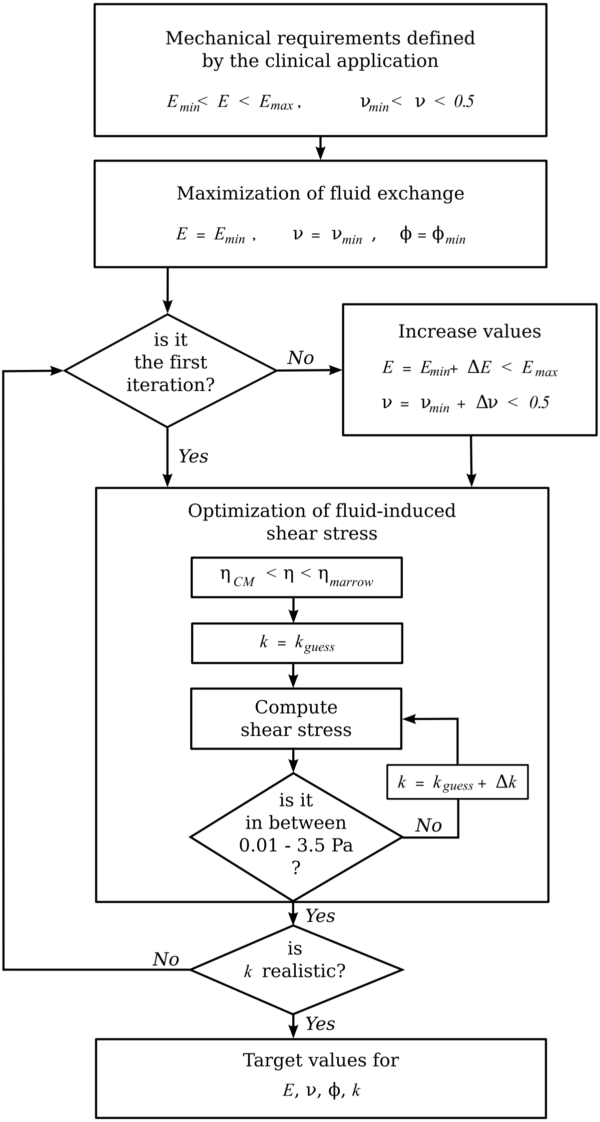
Mechanical requirements defined by the clinical application
$E_{min} < E < E_{max}$, $\nu_{min} < \nu < 0.5$
Maximization of fluid exchange
$E = E_{min}$, $\nu = \nu_{min}$, $\phi = \phi_{min}$
is it the first iteration?
No
Yes
Increase values
$E = E_{min} + \Delta E < E_{max}$
$\nu = \nu_{min} + \Delta\nu < 0.5$
Optimization of fluid-induced shear stress
$\eta_{CM} < \eta < \eta_{marrow}$
$k = k_{guess}$
Compute shear stress
$k = k_{guess} + \Delta k$
is it in between 0.01 - 3.5 Pa ?
No
Yes
is k realistic?
No
Yes
Target values for
E, ν, ϕ, k

Figure 3.24: Flow chart to optimize the construct physical parameters.

However, the outcome of the fluid-induced shear stress optimization may yield an unrealistically high permeability. Indeed, the permeability is governed by many parameters such as the pore interconnectivity, the surface and volume porosities and the specific surface area which may be difficult to control during manufacturing. In that case, the construct stiffness and Poisson's ratio may be increased within the optimal range defined by the clinical application. Accordingly, the target permeability value is decreased. It should be noted that increasing the construct stiffness and Poisson's ratio decreases the fluid exchange between the construct and its environment.

In the particular case of open wedge tibial osteotomy, the optimal wedge stiffness was computed to be in the range of 0.5 to 3.2 GPa (see section 2.5). According to the parametric analysis, the construct stiffness should be minimized to maximize the wedge fluid volume exchange with its environment. Therefore a wedge stiffness of 0.5 GPa should be targeted.

The Poisson's ratio did not play a significant role in the biomechanics of the open wedge tibial osteotomy. Consequently, a minimal value may be targeted as it maximizes the fluid volume exchange. However, the control of the Poisson's ratio is not an easy task and specific processing procedures are necessary to obtain negative Poisson's ratio materials [57, 60]. Therefore, a minimum Poisson's ratio of 0.1 may be reasonably targeted.

The porosity was shown to play a small but significant role in the fluid volume exchange between the construct and its environment. As discussed above, the porosity also impacts the construct's resorption rate and stiffness which should be chosen to achieve specific goals. Nevertheless, the porosity may be defined *a priori*. In this case, a minimal porosity above 50% may be targeted. Although not consensual, this minimal value appears to be associated with good *in vivo* osteointegration [56, 91, 102, 203].

With these values, a maximized fluid volume exchange could be achieved with the porous construct when used as a wedge in open wedge tibial osteotomy. It was computed that in such configuration the fluid volume exchange per loading cycles was 2.7% of the total wedge volume. Consequently, the equivalent of the total wedge volume was exchanged with the environment every 40 cycles of gait. In addition, the fluid-induced shear stress due to the culture medium motion was computed to have a maximal magnitude of 0.02 Pa at the wedge periphery. The shear stress is likely to increase by a factor 10 or 100 during the first postoperative weeks due to an increase of the fluid viscosity. Therefore, a maximal fluid-induced shear stress smaller than 2 Pa is likely to take place *in vivo* which is within the range of 0.01 and 3.5 Pa at all time points. Finally, the maximal pore pressure inside the wedge was computed to be less than 1.3 kPa which is unlikely to produce any damage on the bone cells embedded in the construct. In conclusion, a construct that has an elastic modulus of 0.5 GPa, a Poisson's ratio of 0.1, a porosity of 50 %

Table 3.4: Optimized wedge properties for its use in the open wedge tibial osteotomy.

Parameter	Symbol	target value
E-modulus	E	0.5 GPa
Poisson's ratio	ν	0.1
Porosity	ϕ	>50 %
Permeability	k	$1 \cdot 10^{-10}$ m^2

and a permeability of $1{\cdot}10^{-10}$ m^2 is likely to present a favorable mechanical environment for the embedded bone cells (see table 3.4). It is interesting to note that the values which optimize the construct fluid conductivity are similar to those of the cancellous bone [42].

3.5 Conclusions

This chapter focused on the second level of the multi-scale study. The systematic screening of the construct biomechanical properties initiated in chapter 2 was pursued to optimize the construct osteointegration, osteoinduction, osteoconduction and osteogenesis properties. The chapter was divided into three parts that concentrated on three different aspects: *(i)* the definition of the suitable fluid carrier to ensure a good cell viability *(ii)* the identification of the mechanical characteristics of a PLLA-5%βTCP porous material developed at EPFL and *(iii)* the evaluation of fluid motion inside the porous construct due to mechanical loading. The results obtained in each part are summarized and discussed hereafter.

The goal of the first part was to enhance the artificial bone construct osteoinduction and osteogenesis by including fetal bone cells inside the porous material. Two cell delivery systems were compared. First, the construct impregnation was achieved by injecting a two component fibrin gel loaded with fetal cells inside the construct. This solution was only partially satisfactory as the number of fetal cells embedded in the gel decreased as long as the gel was present. The second cell delivery system was more satisfactory as it used culture medium as cell carrier which was shown to ensure good cell viability. In addition, the impregnation of thick samples was efficiently achieved by a custom apparatus developed at the Laboratory of Biomechanical Orthopedics EPFL.HOSR. The method was rapid, cheap and user-friendly and may be a potential candidate for use in the operating theater.

Despite many efforts, the activity of the cells embedded in the PLLA-5%βTCP constructs could not be measured. In fact, not enough intact RNA could be extracted from the constructs which prevented the quantification of the expression of specific genes. Consequently, the hypothesis that fluid motion due to mechanical loading enhances the osteoinduction and osteogenesis of PLLA-5%βTCP construct could not be verified experimentally. Nevertheless, many researchers have shown that bone cell culture in 2D and 3D structures are sensitive to fluid motion [61, 83, 150, 181]. Therefore, the hypothesis that fluid-induced shear stress enhance the bone cell activity was maintained although no experimental validation was available for the particular case of fetal bone cells embedded in PLLA-5%βTCP porous material.

The second objective of this chapter was to determine the mechanical behavior and evolution of the PLLA-5%βTCP porous material. To do so, the limiting fatigue stress was first determined by carrying out mechanical tests on a porous sample in a controlled atmosphere mimicking physiological conditions. It was found that the porous samples supported about 3'000 cycles of 0-1 MPa applied at 1Hz and more than 170'000 cycles at 0-0.4 MPa before visible signs of structural damage could be observed. In addition, the samples' mechanical behavior could be described by a non-linear elastic constitutive law with long and short term memory effects that were intrinsic to the solid skeleton. Plastic deformations were found to take place gradually at an average rate of 0.2% per day or $2.7{\cdot}10^{-5}$ % per loading cycle. Finally no aging effect could be identified.

These mechanical tests revealed that the major advantage of the PLLA-5%βTCP porous material is its ability to support large deformation of 2-3% for a relatively high number of cycles. In contrast to ceramic artificial bone substitutes that exhibit brittle fracture at about 1% strain, the deformability and ductility of PLLA-5%βTCP constructs are major advantages. In addition, compliant constructs induce larger fluid motion than stiff constructs which ensures a larger fluid volume exchange between the construct and its environment. This phenomenon is important as it may favor the transport of bone growth factors, bone cells and wastes throughout the construct which is essential for its osteointegration, osteoinduction and osteogenesis.

The potential applications for the PLLA-5%βTCP porous material are thus regions subject to large deformation and low mechanical stress. For instance, PLLA-5%βTCP may be an efficient osteoinductive material in non-weight bearing applications such as a filler of void space caused by cysts, impacted fractures, finger or wrist *arthrodesis*, reconstruction of mandibular defects and *sinus lift*. It could also be used in weight-bearing applications such as spine fusion, vertebrectomies, open wedge tibial osteotomy and madibular distraction with strong mechanical structures that support all mechanical loads.

As already pointed out in the previous paragraph, the fluid motion inside the porous bone substitute appears to be an important factor that could favor and shorten the substitute osteointegration. In the first approach, two parameters were assumed to play a significant role which were *(i)* the relative fluid volume exchange between the wedge and its environment and *(ii)* the average fluid-induced shear stress exerted on the solid skeleton. Using linear poroelastic theory, the effect of the construct physical parameters on these two parameters were systematically studied. Based on the results, an algorithm was proposed to identify the target physical parameters of a porous bone substitute so that the fluid exchange was maximized and that the fluid induced shear stress stayed within given intervals.

The systematic parameter analysis permitted a clear and synthesized overview of the role of each physical parameter to be developpeddevelopedless, further experimental and theoretical work is still needed to integrate evolution laws within a time dependent model to test different scenarii and assess the long term role of each parameter. For instance, this could be achieved within the theoretical framework presented in section 3.4.1 by introducing internal variables that characterize the average molecular weight of the polymers [71], the free volume within the polymer mesh [177] or the mass of mineralized extra cellular matrix. The ultimate goal could be to identify the degradation parameters that should be targeted to obtain a smooth transition between artificial bone and new bone. Indeed, this point was still problematic in 2006 as most of the commercially available artificial bone substitutes presented either rapid and unpredictable resorption (tricalcium phosphate ceramic, calcium phosphate cement, coralline hydroxyapatite, massive PLLA), or slow resorption (artificial hydroxyapatite, polymethyl methacrylate cement, some bioglass and glass ionomers).

CHAPTER 4

The Interaction Between Fluids And Cells

Chapter 3 focused on the fluid motion induced by mechanical loads applied to a porous construct saturated with fluid. In the mechanical framework defined by the open wedge tibial osteotomy of chapter 2, a method was proposed to optimize the construct fluid conductivity and mechanical properties to enhance its osteointegration and osteoinduction.

In particular, the fluid-induced shear stress was estimated at an intermediate length scale (10 mm) thanks to averaging methods and continuum mechanics applied to a porous media. It was proposed that the average fluid-induced shear stress should be in the range of 0.01 Pa to 3.5 Pa to stimulate the bone cells embedded in the construct to produce bone extracellular matrix. Indeed, bone cells (osteoblasts and osteocytes) clearly respond to steady and dynamic fluid induced shear stress [10, 22, 31, 47, 83, 87, 90, 99, 110, 125, 159, 193]. Although the bone cells are also sensitive to mechanical stretching [93, 94, 187], fluid-induced shear stress seems to play a dominant role in bone remodeling [200, 201].

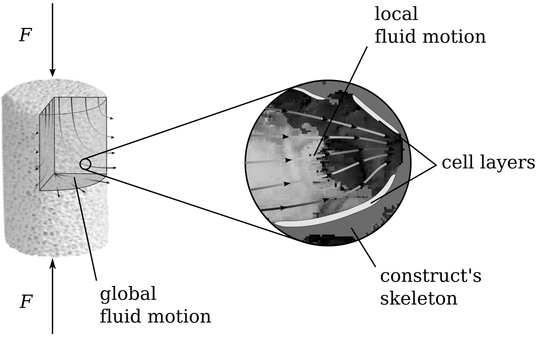

Figure 4.1: Fluid motion induced by mechanical loading locally stimulates layers of bone cell.

The steady state fluid-induced shear stress, which is the parameter used in most studies for describing the mechanical stimulus, is a good measure of the effective mechanical stress exerted by a fluid moving at low frequency. However, it may be misleading for describing the effective mechanical stress that a cell layer experiences when the fluid is moving at high frequency due for example to muscle vibrations [37] or environmentally induced vibrations (cars, boring machine, chainsaw).

At high frequency, a dynamic mechanical interaction between the cell layer and the fluid is likely to take place (see figure 4.2). The transient deformation of the cell layer due to the fluid-induced shear stress changes the fluid boundary conditions. The fluid flow pattern is then changed which impacts the interfacial shear stress and may in turn impact bone cell stimulation.

This chapter focuses on the effects of cell/fluid interaction between bone cells and the local fluid motion inside the pore of an artificial bone construct. Its goal is to optimize the local construct architecture to achieve adequate bone cell stimulation. To reach this goal and despite natural variation of the geometry, the simplest geometrical configuration was chosen to highlight the sensitivity of the mechanical parameters. A one dimensional time dependent model was applied which is described in the following section.

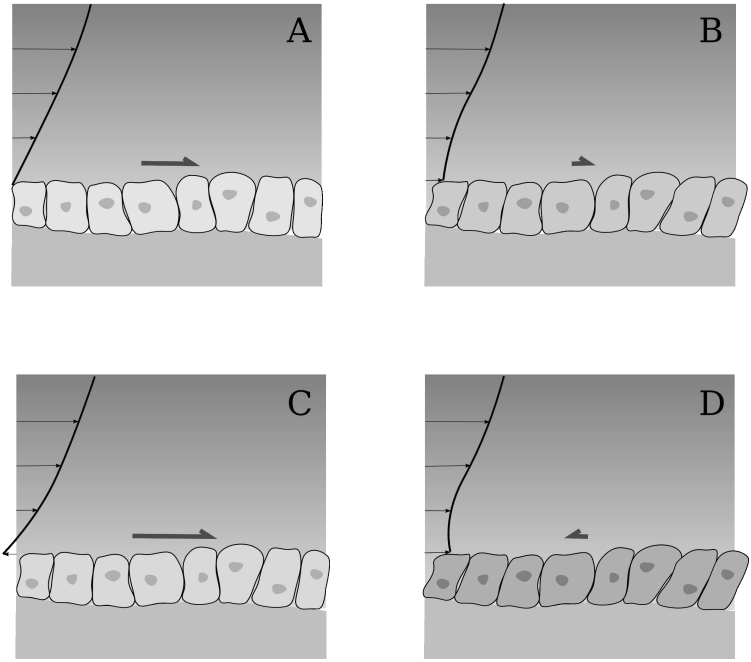

Figure 4.2: Graphic illustrating the cell/fluid interaction: (A) the fluid flow exerts a shear stress (red arrow) on a cell layer that (B) causes the cells to deform which modifies the fluid motion near the cell membrane. The fluid-induced shear stress is reduced and (C) the cells deforms back towards their initial position. Again, this movement changes the fluid flow pattern near the cell membrane and the fluid-induced shear stress. (D) the cell/fluid interaction goes on.

4.1 A One Dimensional Cell/Fluid Model

A Newtonian incompressible fluid of dynamic viscosity η and mass density ρ_f was confined in an infinitely long canal of height H. Located at its lower boundary was a semi infinite elastic solid of height h that represented a monolayer of cells. The solid lower edge was fixed in all translations to a rigid wall, and was uniformly in contact with the fluid at its upper edge. The system was initially at rest. At $t > 0$, the upper wall of the canal was set in motion parallel to the lower rigid wall with an harmonic velocity of $v_0 \sin \omega_0 t$. Figure 4.3 presents the cell/fluid system. The monolayer of cells was assumed to be homogeneous, isotropic and linearly elastic.

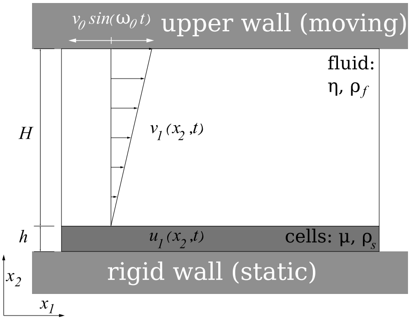

Figure 4.3: Simplified configuration of a cell layer stimulated by an oscillating fluid flow.

4.1.1 Assumptions & Governing Equations

The physical modeling of the cell/fluid interaction was derived from classical continuum mechanics, together with four assumptions numbered (A1) to (A4). First, the interaction problem was considered in a one dimensional, time dependent framework, i.e. the fluid velocity $\mathbf{v}$ and pressure p as well as the solid displacement $\mathbf{u}$ were assumed to be a function of the cross flow direction x_2 and time t.

$$\mathbf{v} = \mathbf{v}(x_2, t) \qquad p = p(x_2, t) \qquad \mathbf{u}(x_2, t) \tag{A1}$$

Fluid

The motion of Newtonian incompressible fluids is described by the mass continuity equation

$$\nabla \cdot \mathbf{v} = 0 \tag{4.1}$$

together with the Navier-Stokes equations.

$$\rho_f \left[\frac{\partial \mathbf{v}}{\partial t} + (\mathbf{v} \cdot \nabla)\mathbf{v} \right] = -\nabla p + \eta \triangle \mathbf{v} + \mathbf{f} \tag{4.2}$$

The equations (4.2) were first simplified by neglecting all external forces

$$\mathbf{f} = 0\ . \tag{A2}$$

Defining the dimensionless (stared *) variables

$$\mathbf{v} = \mathbf{v}^* V, \quad \mathbf{x} = \mathbf{x}^* L, \quad t = t^* T, \quad p = p^* \frac{\eta V}{L} \tag{4.3}$$

allows the Navier-Stokes equations to be written in dimensionless form

$$Re \cdot St \frac{\partial \mathbf{v}^*}{\partial t^*} + Re(\mathbf{v}^* \cdot \nabla^*)\mathbf{v}^* = -\nabla^* p^* + \triangle^* \mathbf{v}^*\ , \tag{4.4}$$

where *Re* is the Reynolds number and *St* the Strouhal number. As the majority of biological fluid flows are taking place at very low Reynolds and Strouhal's numbers

$$Re \leq 1 \quad \text{and} \quad Re \cdot St \leq 1\ , \tag{A3}$$

the convective and inertial terms of the Navier-Stokes equations (4.4) were neglected. The assumption $Re \cdot St \leq 1$ restricted the domain of validity of the fluid description. In the case of fixed geometry, the excitation frequency was therefore restricted to

$$f < f_{crit} \quad \text{where} \quad f_{crit} = \frac{\eta}{\rho_f H^2}\ . \tag{4.5}$$

The governing equations for the fluid motion were finally assumed to be

$$\nabla \cdot \mathbf{v} = 0 \tag{4.6a}$$

$$\eta \triangle \mathbf{v} = \nabla p\ . \tag{4.6b}$$

The non-slip condition in the x_2-direction and the no-flow (impermeable) condition in the x_1-direction were used at the upper fluid boundary.

$$v_1(H+h,t) = v_0 \sin(\omega_0 t) \quad v_2(H+h,t) = 0 \quad \forall\, t > 0 \tag{4.7}$$

Finally, the system was assumed to be at rest for $t = 0$ which gave the following initial conditions.

$$v_1(x_2,0) = v_2(x_2,0) = p(x_2,0) = 0 \quad \forall\, x_2 \in [h, h+H] \tag{4.8}$$

Cell Layer

The equilibrium of forces in a linearly elastic homogeneous isotropic cell layer is described by the Navier equations, which were expressed in terms of the deformation field **u** [147]

$$(\lambda + \mu)\nabla(\nabla \cdot \mathbf{u}) + \mu \triangle \mathbf{u} + \mathbf{f} = \rho_s \frac{\partial^2 \mathbf{u}}{\partial t^2}\ , \tag{4.9}$$

where λ and μ are the Lamé coefficients. Similarly to the fluid domain, the volume forces were assumed zero in the solid domain, i.e. $\mathbf{f} = 0$. Finally, the lower edge of the cell layer was fixed in all translations to a rigid and static wall

$$u_1(0,t) = 0 \quad u_2(0,t) = 0 \qquad \forall\, t > 0 \tag{4.10}$$

and the cell layer was considered at rest for $t = 0$

$$u_1(x_2,0) = 0 \quad u_2(x_2,0) = 0 \qquad \forall\, x_2 \in [0,h]\ . \tag{4.11}$$

Interaction Between Cell Layer and Fluid

The continuity of forces and velocities at the interface Γ_{fs} between the two media created the coupling between the cell layer and the fluid. More precisely, the kinetic coupling between the elastic layer and the fluid was computed as

$$\mathbf{v} = \frac{\partial \mathbf{u}}{\partial t} \qquad \forall\, x_2 \in \Gamma_{fs} \quad \text{and} \quad t > 0\,. \tag{4.12}$$

The dynamic coupling was given by continuity of stresses at the interface

$$\boldsymbol{\sigma}_f \mathbf{n}_f = \boldsymbol{\sigma}_s \mathbf{n}_s \qquad \forall x_2 \in \Gamma_{fs} \quad \text{and} \quad t > 0\,. \tag{4.13}$$

where $\boldsymbol{\sigma}_f$ and $\boldsymbol{\sigma}_s$ are the fluid and cell layer stress tensors respectively. The unitary normal vector at the interface of the fluid and solid were denoted by $\mathbf{n}_f$ resp. $\mathbf{n}_s$. Finally, the constitutive law for a Newtonian incompressible fluid was recalled from [32]

$$\boldsymbol{\sigma}_f = -p\boldsymbol{I} + \eta\left(\nabla\mathbf{v} + \nabla\mathbf{v}^T\right)\,, \tag{4.14}$$

and the constitutive equation for a linear elastic medium was written in terms of solid displacement $\mathbf{u}$

$$\boldsymbol{\sigma}_s = \lambda\,(\nabla\cdot\mathbf{u})\,\boldsymbol{I} + \mu\left(\nabla\mathbf{u} + \nabla\mathbf{u}^T\right)\,. \tag{4.15}$$

4.2 The Analytical Solution

4.2.1 The Interfacial Shear Stress

The assumptions (A1-A3) applied to the solid and fluid equations (4.6,4.9) yielded a one dimensional time dependent cell/fluid interaction problem. The initial and boundary conditions (4.7-4.8,4.10-4.13) allow the solid displacement $\mathbf{u}$, fluid velocity $\mathbf{v}$ and pressure p to be expressed as a functions of x_2, t and of the unknown shear stress at the interface $\tau(t)$. After substitution and simplification[1], it was possible to reduce the problem to one equation for $\tau(t)$

$$\begin{aligned} v_0 \sin\omega_0 t - \frac{H}{\eta}\tau(t) = &-\frac{d}{dt}\left\{\sum_{n=1}^{\infty}\frac{2}{k_n^3 a h \mu}\int_0^t \ddot{\tau}(s)\sin\left[k_n a(t-s)\right]ds\right\} \\ &-\frac{2}{h\mu}\sum_{n=1}^{\infty}\frac{\dot{\tau}(0)}{k_n^2}\cos\left(k_n a t\right) + \frac{h}{\mu}\dot{\tau}(t) \end{aligned} \tag{4.16}$$

where a is the shear stress wave propagation velocity in the cell layer given by $a = \sqrt{\frac{\mu}{\rho_s}}$, with $k_n = \frac{\pi}{2h}(2n-1)$, and n a positive integer. In order to determine the shear stress function $\tau(t)$, the Laplace transform was applied to (4.16).

$$\mathcal{L}\left\{\tau(t)\right\} = \frac{v_0 \dfrac{\omega_0}{\omega^2 + \omega_0^2}}{\sum_{n=1}^{\infty}\left(-\alpha_n \dfrac{\omega^3}{\omega^2 + \omega_n^2}\right) + \beta\omega + \gamma} \tag{4.17}$$

---

[1] For more details, see Appendix D

with

$$\omega_n = k_n a \quad \alpha_n = \frac{2a^2}{\omega_n^2 h\mu} \quad \beta = \frac{h}{\mu} \quad \gamma = \frac{H}{\eta} \tag{4.18}$$

The Laplace transform was chosen because it is applicable to harmonic function and has convenient derivation, integration and convolution properties. The series of equation (4.17) converged as $n \to \infty$ to

$$\sum_{n=1}^{\infty}\left(-\alpha_n \frac{\omega^3}{\omega^2+\omega_n^2}\right) = \frac{a}{\mu}\tanh\left(\frac{h}{a}\omega\right) + \frac{h}{\mu}\,. \tag{4.19}$$

However, substituting (4.19) in (4.17) led to a function rather difficult to inverse Laplace transform into the space-time domain. Therefore, the sum (4.19) was limited to the first term.

$$\sum_{n=1}^{\infty}\left(-\alpha_n \frac{\omega^3}{\omega^2+\omega_n^2}\right) \approx -\alpha_1 \frac{\omega^3}{\omega^2+\omega_1^2} \tag{A4}$$

The assumption (A4) introduced a limited error as the ratio of the series' first term (A4) to the infinite series (4.19) is upper and lower bounded.

$$\frac{96}{\pi^4} = \Delta(0) > \Delta = \frac{-\alpha_1 \dfrac{\omega^3}{\omega^2+\omega_1^2}}{\frac{a}{\mu}\tanh\left(\frac{h}{a}\omega\right) + \frac{h}{\mu}} > \Delta(\infty) = \frac{8}{\pi^2} \tag{4.20}$$

The approached solution for $\tau(t)$ using assumption (A4) was obtained by inverse Laplace transform[2]

$$\tau(t) = \tau \sin(\omega_0 t + \delta) + g(t)\,, \tag{4.21}$$

where the function $g(t)$ is the transient response of the system. As the function $g(t)$ was found to tend rapidly toward zero for $t > 0$, the transient behavior of the system was neglected. Consequently, only the first part of equation (4.21) is further discussed. Equation (4.21) showed that the interfacial shear stress oscillates at the same frequency as the excitation, but delayed of a phase shift δ. A dimensionless shear stress amplitude τ^* was introduced by normalizing the shear stress amplitude τ by the steady state fluid induced shear stress $\tau_0 = \dfrac{v_0\eta}{H}$

$$\tau^* = \frac{\pi^2\mu H}{(\pi^2-8)h\eta}\frac{\omega_0^2+\omega_1^2}{\sqrt{\omega_0^6 + J_2\omega_0^4 + J_1\omega_0^2 + J_0}} \tag{4.22}$$

with

$$\begin{aligned} J_2 &= \frac{\pi^4}{2\left(\pi^2-8\right)^2}\frac{\mu}{h^2\eta^2\rho_s}\left[2H^2\mu\rho_s - \eta^2\left(\pi^2-8\right)\right] \\ J_1 &= -\frac{\pi^6}{16(\pi^2-8)^2}\frac{\mu^2}{h^4\eta^2\rho_s^2}\left(8H^2\mu\rho_s - \eta^2\pi^2\right) \\ J_0 &= \left[\frac{\pi^4 H\mu^2}{4\left(\pi^2-8\right)h^3\rho_s\eta}\right]^2 \end{aligned} \tag{4.23}$$

---

[2] For a complete derivation, see Appendix E

The dimensionless shear stress τ^* measures the modulation of the dynamic shear stress with respect to the steady state shear stress. It may also be viewed as an amplification or damping factor of the steady state shear stress that takes into account dynamical effects. The dimensionless shear stress τ^* is thus equal to one for steady state flow, is larger than one when dynamical amplification takes place and smaller than 1 when damping occurs. In addition, τ^* is always positive.

Analysis of equations (4.22-4.23) showed that no singularities are present in the range of positive excitation frequency. Taking the first derivative of τ^* with respect to the excitation frequency ω_0 showed that the interfacial shear stress amplification factor has one or two extrema, depending on the value of the dimensionless number N_{fs} defined as

$$N_{fs} = \frac{\eta}{H\sqrt{\mu\rho_s}} \,. \tag{4.24}$$

The dimensionless number N_{fs} emerged out after analysis of the discriminant of the sixth order polynomial appearing as nominator after the derivation of (4.22)[3]. For values of N_{fs} smaller than $4/\pi$, the interfacial shear stress scaling factor has one and only one extremum, which is a maximum (see figure 4.4 left). In other words, the dimensionless interfacial shear stress τ^* follows a resonance like behavior. The magnitude and location of the maximum are related to the dimensionless number N_{fs} and the cell layer height h. The smaller N_{fs} is, the larger the shear stress amplification becomes.

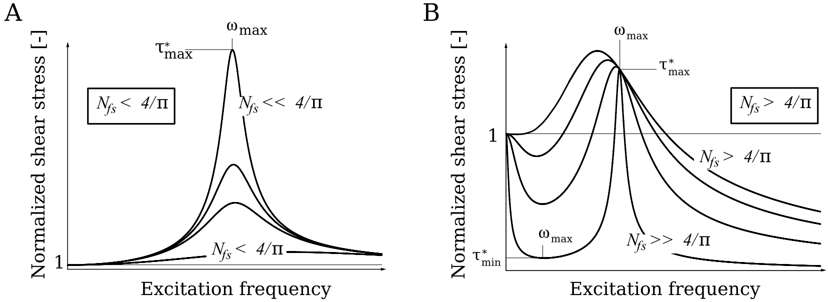

Figure 4.4: Dimensionless shear stress at the interface between fluid and cell layer as a function of the excitation frequency for (A) $N_{fs} < 4/\pi$ and (B) $N_{fs} > 4/\pi$. The magnitude of N_{fs} is related to the magnitude of the interfacial shear stress.

For values of N_{fs} higher than $4/\pi$, the interfacial shear stress scaling factor has two extrema - a minimum and a maximum. The interfacial shear stress first decreases rapidly toward a local minimum. Then, it increases toward a upper maximum bounded by 1.48 and finally tends to zero for $\omega_0 \to \infty$ (see figure 4.4 right). The magnitude and location of the local minimum are dependent on the dimensionless number N_{fs} and the cell layer height h. The bigger N_{fs} is, the stronger the damping of the interfacial shear stress becomes.

---

[3] See appendix E for the detailed mathematical steps

4.2.2 The Cell Layer Deformation

The cell layer deformation was obtained by computing the transient reaction of an elastic layer to a sinusoidal shear stress of the form $\tau(t) = \tau\sin(\omega_0 t + \delta)$. The analytical solution discussed hereafter was obtained by solving the Navier equations (4.9) together with assumptions (A1, A2), initial and boundary conditions (4.10-4.11).

$$\begin{aligned} u(x,t) =&\tau \sum_{n=1}^{\infty}(-1)^n \frac{2}{\omega_n^3 h\rho_s}\frac{\omega_0}{\omega_n^2-\omega_0^2}\left[\omega_n\omega_0\sin(\omega_0 t+\delta)\right. \\ &\left.+(\omega_n^2-2\omega_0^2)\sin\left(\omega_n t+\frac{\omega_n}{\omega_0}\delta\right)\right]\sin\frac{\omega_n}{a}x \qquad (4.25) \\ &+\frac{\tau}{\mu}x\sin(\omega_0 t+\delta) \end{aligned}$$

The equation (4.25) is composed of two main terms. The first term (the first two lines) represents the cell deformation due to inertial effects. This term vanishes for zero excitation frequency ω_0, and grows in magnitude as the excitation frequency gets closer to the resonance frequencies $\omega_n = \frac{\pi}{2h}\sqrt{\frac{\mu}{\rho_s}}(2n-1)$. Note that the inertial term of the cell layer deformation is composed of two wave groups: one that has the same period as the excitation frequency, and a second one that has frequencies equal to the resonance frequencies ω_n (see figure 4.5). Finally, the term on the second line of equation (4.25) represents the quasi-static response of an elastic layer to a sinusoidal shear stress excitation.

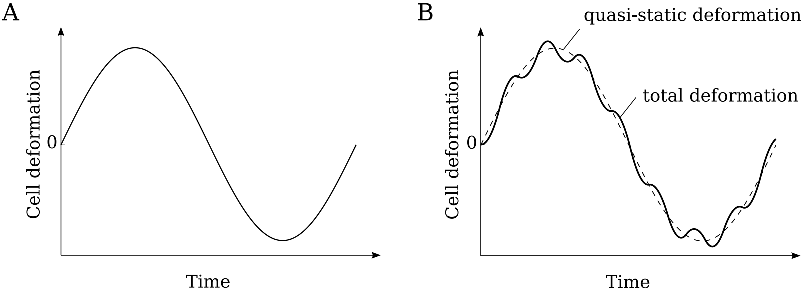

Figure 4.5: Cell elastic response to sinusoidal shear stress excitation at excitation frequency (A) much smaller than the resonance frequency and (B) at excitation frequency close to resonance.

4.3 Numerical Validation

The analytical development discussed in the previous section was possible thanks to simplifying but not simplistic assumptions. In particular, the assumption that the cell layer deformations were small is questionable. Therefore, a numerical model was built to assess the accuracy of the analytical approach with respect to these assumptions.

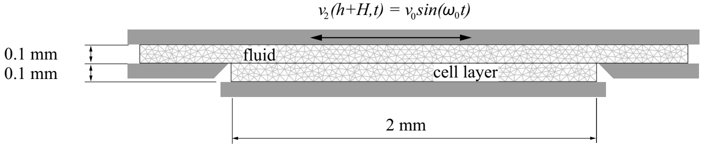

Figure 4.6: Layout of the numerical model.

A two dimensional numerical model was created with the commercial software Comsol 3.2b (Comsol Inc., Burlington, MA, USA). The cell layer and fluid domains were discretized into 936 elements in total (8894 degrees of freedom). The quality of the mesh was checked by comparing the solution obtained with this mesh and the solution obtained with a much finer mesh of 14’833 elements. A maximal deviation of 0.0515% was observed, which is acceptable.

The fluid motion was modeled by the incompressible Navier-Stokes equations. A neo-Hookean incompressible hyperelastic constitutive law was assumed for the cell monolayer. Such material description shows good agreement with experimental data for isolated endothelial cell [23], and was therefore used. The constitutive law is given by

$$\mathbf{S} = -p\mathbf{C}^{-1} + \mu\mathbf{I}\,, \tag{4.26}$$

where $\mathbf{S}$ is the Piola-Kirchhoff II stress tensor, p is the hydrostatic pressure, μ is the shear modulus and $\mathbf{C}$ is right Cauchy-Green strain tensor. The coupling at the interface was achieved by continuity of stress and velocity. The numerical solution was computed on a moving mesh using the arbitrary-Lagrange-Euler method (ALE), and large deformations were assumed for the solid domain.

Initially, the cell/fluid system was at rest. At $t > 0$, the upper wall of the canal was accelerated smoothly so that it reached a harmonic oscillating velocity after one period.

$$v_1(H+h,t) = \begin{cases} v_0\left(\dfrac{\omega_0}{2\pi}t\right)^2 \sin\left(\omega_0 t\right) & \forall\, t \in \left[0, \dfrac{2\pi}{\omega_0}\right] \\ v_0 \sin\left(\omega_0 t\right) & \forall\, t > \dfrac{2\pi}{\omega_0} \end{cases}$$

The computation of the stresses and deformations were carried out during four periods. The last two periods were used for determining the shear stress and shear deformation amplitude.

Large fluid and cell layer aspect ratios (>20) were chosen to approach a one dimensional condition around the cell layer mid length. In such configurations, 54.2% of the total cell layer length had pressure, deformation and velocity values within a 1% interval around the mid-length

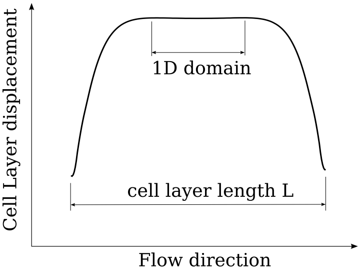

Figure 4.7: Typical variation of the cell layer deformation with flow direction.

value and reached 72% within a 10% interval (see figure 4.7). In addition, this proportion was found to increase with increasing cell layer aspect ratio. As a result, the shear stress computed from the analytical model is likely to be representative of the shear stress experienced by most cells in bone, blood vessel and synovial capsule. Indeed, in these particular locations, cells form layer of millions of individuals, presenting very large aspect ratio.

4.3.1 Effect of Large Deformations on Interfacial Shear Stress

The numerical model was first used to demonstrate that although the analytical approach assumed small deformations, the model remained valid for large deformations. The interfacial shear stress amplitudes computed with the numerical model assuming large deformations matched with the analytical results. Discrepancies smaller than 0.8% were observed for a range of deformation spreading over 4 orders of magnitude, from 0.003% to 30% (see Figure 4.8).

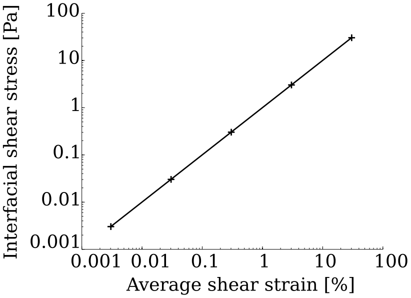

Figure 4.8: Interfacial shear stress determined for different upper wall velocities and related to the solid averaged strain. The values obtained from the analytical model are drawn in plain line (-), where the cross symbol (+) are used for values computed with the numerical model assuming large deformation.

The very good agreement between the analytical and numerical model was due to two facts. First, the cell layer deformation induced by the fluid movement was largely dominated by shear strain. Second, the neo-Hookean constitutive law that successfully describes endothelial cell, related linearly the shear strain to the Piola-Kirchhoff II shear stress. Therefore, material and geometrical non-linearities did not play a role in this particular configuration, at least for shear strains smaller than 30%.

4.3.2 Effect of Excitation Frequency on Interfacial Shear Stress

The numerical model was then used to compute the shear stress at the interface between the cell layer and fluid for different excitation frequencies. These values were normalized by the steady state interfacial shear stress and compared to those obtained with the analytical model.

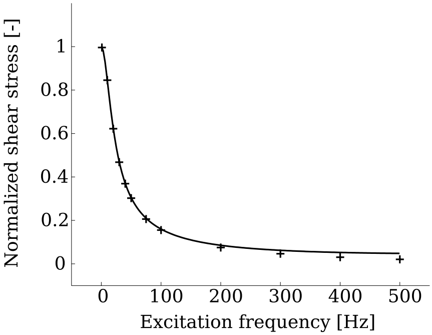

Figure 4.9: Effect of excitation frequency on dimensional shear stress τ^* obtained with the analytical model (plain line) and the numerical model (+).

The two models matched very well for low excitation frequencies ($<$ 100Hz). However, for high excitation frequencies, the analytical model overestimated the interfacial shear stress. This discrepancy may be explained by two sources of error. First, as the fluid inertial loads were neglected in the analytical model, an excitation frequency dependent error was introduced. Second, by reducing the infinite series of equation (A4) to its first term, a frequency dependent error was introduced. Both errors combined and became important at high frequency.

4.4 Applications To Osteoblasts in PLLA Construct

As discussed in chapter 3, the global fluid motion inside a bone construct due to mechanical loading is important for its osteoinduction and osteogenesis characteristics. In addition to ensuring the transport of nutriment and waste, the fluid motion exerts shear stresses on the osteoblast's surfaces that are shown to increase the production and release of TGF-β1 and other essential growth factors [90, 104, 161]. These proteins are essential for the recruitment inside the construct of mesenchymal stem cells and for their differentiation into bone forming cells [75, 78, 136]. An optimized construct that induces an adequate global fluid motion due to mechanical loading is thus likely to enhance its osteointegration and osteoinduction properties.

On a smaller length scale, the cell/fluid interaction phenomenon described in this chapter may also impact bone cell stimulation and construct osteoinduction. The local changes of fluid velocity near the cell membrane were shown to modulate the shear stress at their common interface. This phenomenon was found to be characterized by a novel dimensionless number N_{fs} that identifies whether the shear stress is likely to be amplified or damped at high frequency. Its application to a typical construct pore geometry colonized by a layer of active bone cells might define a specific range of pore diameter that favors bone cell stimulation.

The typical configuration of bone cells inside a PLLA construct pore was estimated from μ-CT images of dry constructs (Scanco Medical AG, Bassersdorf, Switzerland). The averaged pore diameter was computed from these images with help of a dedicated algorithm [68]. The cell layer that colonizes the pore walls[4] was assumed to have a height h of 20 μm [42]. The fluid and cell layer mass densities were assumed to be similar to water density. Finally, the cell shear modulus was taken from the literature [23, 54]. All values used in the model are summarized in table 4.1.

Table 4.1: A typical configuration of osteoblast layers inside construct pore.

Parameter	Symbol	Value
Mean pore size	D	480 ± 220 μm
Mean cell height	h	20 μm
Mean cell density	ρ_s	1000 kg/m^2
Mean cell shear modulus	μ	500 Pa

The viscosity of the fluid that stimulates the cells may spread over three to four orders of magnitude. Immediately after implantation, the viscosity of the fluid saturating the pores is of the order of 0.001 Pa·s, as culture medium was used for the impregnation process. Then, the fluid viscosity is likely to increase with time as the initial fluid is gradually replaced by the peri-implant fluid that has a viscosity similar to bone marrow (0.01-1 Pa·s [18, 113]). Consequently, the dimensionless number N_{fs} is likely to vary with time.

In particular, a construct corresponding to the description of table 4.1 would exhibit a dimensionless number N_{fs} higher than $4/\pi$ for fluid viscosity greater than 0.22 Pa·s. In this case, the dynamic shear stress at the cell/fluid interface is damped for increasing excitation frequency (see Figure 4.4). For instance, the shear stress damping due to a viscous fluid of 1 Pa·s was computed to be 1% at 50 Hz and to reach 32% at 1 kHz.

On the other hand, a low viscous fluid inside the same artificial bone construct was computed to amplify the interfacial shear stress. For instance, a culture medium that has a viscosity of 0.001 Pa·s was computed to induce a maximal amplification of 111 times the steady shear stress at resonance frequency of 8.8 kHz. However, the shear stress amplification was computed to be less than 2.6% for excitation frequencies less than 1 kHz. Consequently, the shear stress

---

[4] Osteoblasts seeded in PLLA construct spontaneously attach to the pore walls and proliferate until confluency [123].

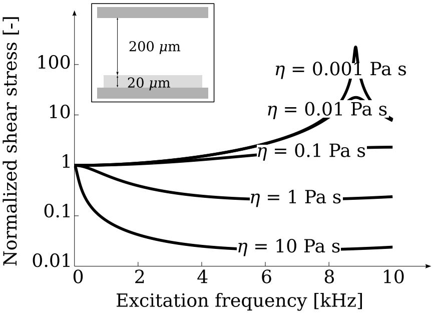

Figure 4.10: Dimensionless shear stress amplification factor due to the interaction between a layer of osteoblast inside a construct's pore and a fluid of different viscosity η, as a function of excitation frequency.

amplification due to the dynamic coupling of a low viscous fluid and bone cells is likely to be small in the range of frequencies to which a person may be subject. A frequency range between 0 and 1 kHz is often considered to encompass most daily and manual activities such as car driving (1-60 Hz), pneumatic drill (1-100 Hz) or chainsaw (0-1 kHz) induced vibrations.

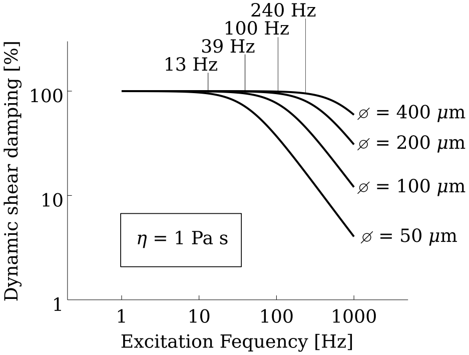

Figure 4.11: Impact of the construct pore size on the dimensionless interfacial shear stress between an osteoblast cell layer and bone marrow (η = 1 Pa·s) as a function of the excitation frequency.

In this range of frequencies (0-1kHz), the construct pore size could play a central role in the modulation of the bone cell stimulation. Although the cell/fluid interaction had negligible effect on the modulation of the interfacial shear stress for N_{fs} values less than $4/\pi$, it was computed to have an important damping effect when N_{fs} was greater than $4/\pi$. In this particular case, the mechanical stimulus on the bone cells was found to be increasingly damped at frequencies greater than 13 Hz in a construct with 50 μm pore diameter. The effective shear stress at the cell/fluid interface was computed to be 63% of the steady state shear stress when stimulated at 100 Hz and was only 4% at 1 kHz. However, the damping magnitude decreased rapidly with increasing pore size and was negligible in the frequency range of 0-1 kHz when the construct pore diameter was larger than 300 μm (see figure 4.11). This suggests that a more efficient bone cell stimulation might be achieved with a construct of pore size larger than 300 μm as no dynamic damping effect is likely to take place.

4.5 Discussion and Conclusions

This chapter focused on the dynamic phenomenon that might modulate cell stimulation embedded in a porous construct. The theoretical approach identified a dimensionless number N_{fs} that indicated whether the interaction amplifies or damps the dynamic shear stress at the cell/fluid interface. Pore diameter was found to impact the dynamic coupling phenomenon between the cells attached to the pore surface and the surrounding fluid.

Several studies show that constructs with pore diameters larger than 300 μm are likely to induce a better and faster osteointegration than constructs with smaller pore size [29, 91, 112]. Besides purely biological reasons, the cell/fluid coupling phenomenon could perhaps also contribute to explain this empirical result.

It is shown that high frequency mechanical stimulation induces higher bone cell response [145, 182] and bone formation [157, 176] than steady stimulation. The damping of high frequency stimulation could perhaps significantly decrease bone cell stimulation. Based on the theoretical development discussed in this chapter, dynamic damping of high frequency stimulation was computed for constructs with pore diameter smaller than 100 μm. On the other hand, it was found that constructs with pore size larger than 300 μm are unlikely to damp dynamic stimulation with excitation frequency below 170 Hz.

It may thus be hypothesized that constructs with pore diameter larger than 300 μm could perhaps stimulate more efficiently bone cells at high frequency than constructs with smaller pore size. Although part of a more complex phenomenon, the mechanical coupling between a cell layer and its surrounding fluid may contribute to explain why construct with small pore size are less osteoinductive than constructs with pore sizes larger than 300 μm. The new dimensionless number N_{fs} is a useful and simple indicator of the type of coupling phenomenon that is likely to take place at the cell/fluid interface and of its magnitude.

The model was intentionally kept simple in many aspects. The objective was to highlight the sensitivity to some mechanical parameters. This choice was made in order to obtain an analytical solution and therefore to develop a global understanding of the problem. Considering that the cell/fluid interaction in a one dimensional and time dependent framework did not permit studying the effect of cell height variation [7, 46] or any phenomena taking place in the other dimensions such as traveling wave flutter observed on dolphin skin [24]. In addition, the assumptions about the cell material neglected the viscous and inhomogeneous effects on the interaction phenomena. Nevertheless, this model brought new insights and aided better understanding of some basic points of fluid cell interaction phenomenon that may be part of more complex phenomena.

Although beyond the scope of this work, the impact of the cell/fluid interaction on the cell deformation should be studied *in vitro*. It would be interesting to compare the cell deformation at low and high stimulation frequency which would assess the impact of dynamic effects on local cell deformation. As an extendion of the work of Davis and Barbee [7,46], the role of dynamic cell/fluid interaction on endothelial cell stimulation would contribute to elucidate the sensitivity of cells to high temporal gradient of shear stress. The cell/fluid interaction could also modify the shear stress spatial gradient distribution over endothelial or osteoblast cell layer and should therefore be studied in more detail. Finally, an essential open issue of mechanotransduction that should be studied taking into account dynamic effects is the role of cell membrane and cytoplasm deformation due to fluid induced stresses.

CHAPTER 5

Conclusions and Perspectives

5.1 Conclusions

Bone harvesting procedures are still associated today with a large number of complications. Summers *et al.* [178] reported that 25% of the patients that underwent iliac crest bone harvest procedure complained of chronic pain at the donor site. It appears that about 8% of grafting procedures using autogenic bone graft are subject to major complications at the donor site such as neurological injuries, iliac wing fracture or deep hematoma formation requiring surgical intervention [4, 178, 202]. Therefore, an efficient and secure bone substitute that avoids the harvesting procedure would be a major breackthrough.

The alternative options to autografts are allografts and synthetic bone grafts. Today, the surgeon's second choice is allograft despite the risks of virus transmission. Synthetic bone substitute presents attractive assets that will probably make it the first choice for tomorrow's surgeons. However, many clinical and biomechanical issues still have to be resolved before it could replace autograft.

Within this framework, this study focused on the biomechanical issues associated with a tissue engineered bone substitute. The principal objective was to identify the optimal biomechanical parameters that would maximize the construct osteointegration and osteoinduction. The multi-scale approach that was adopted permitted systematic screening of the impact of different parameters at three different length scales (see Figure 5.1 for a systematic view of the study).

At a large length scale (0.5 m), the mechanical environment of a bone graft was evaluated for the particular case of open wedge tibial osteotomy. A finite element model was created that had accurate bone geometry and that took into account the inhomogeneity and anisotropy of the bone mechanical properties. The maximal gait load superimposed to the muscle tonus and soft tissue elongation loads was assumed to be the worst loading case that is likely to take place in the first post-operative weeks.

Various wedge geometry, size and mechanical properties were tested. Whilst pursuing the goal of optimizing the wedge osteointegration, an optimized configuration was established. The best compromise was found to be a wedge that covers quarter of the osteotomy cross section, that has a stiffness of between 0.5 and 3 GPa and that is placed together with an anteromedial supporting plate. Such a configuration is likely to favor wedge osteointegration and to present acceptable structural stability and associated costs. However, the level of shear strains and interfacial micromotions at maximal gait load were computed to be above known values for the mineralization of the interface. The use of two crutches during the first six post-operative weeks may be recommended to limit the maximal knee load to an ad hoc value of 50 kg. By doing so, the interfacial micromotions and shear strains were computed to be small enough to favor mineralized bone ingrowth at the interface between the bone and the wedge.

At an intermediate length scale (10 mm), the wedge was no longer considered as a solid bulk material but as a construct: a porous material impregnated with bone cells and saturated with a fluid. Again, the biomechanical parameters that characterize the construct were screened to maximize the osteoinduction and osteogenesis. Three parts may be distinguished which correspond to the parameters related to (*i*) the fluid, (*ii*), the porous solid and (*iii*) the mechanical coupling between the fluid and porous solid.

First, a viability study of the cell embedded in the porous material was conducted which distinguished between two cell delivery systems. It appeared that the use of a standard culture medium together with a customized impregnation device was the most appropriate method to impregnate thick porous samples. This method was rapid and user-friendly which made it a potential candidate for use in the operating theater.

Second, the construct fatigue limit stresses were determined by performing mechanical tests in a controlled atmosphere mimicking the physiological environment. It was found that the PLLA-5%βTCP porous material developed at EPFL supports at least 170'000 cycles of 0-0.4 MPa compression stress oscillating at 1 Hz. Additional tests permitted the identification of the mechanical behavior of this material which was found to be non-linear elastic with long and short term viscous effects. Limited plasticity was observed when the material was submitted to long term dynamic loading. No aging effect could be detected during a loading period of 24 days.

Third, the coupling phenomenon between the porous solid and the saturating fluid was determined using linear poroelasticity. On the basis of fluid conductivity experiments and the above mentioned mechanical tests, the linear poroelasticity described the averaged fluid motion in the PLLA-5%βTCP constructs. It was computed that the equivalent of the total fluid volume enclosed in the porous construct was expelled and sucked-in every 70 compression cycles of 0-0.4 MPa. The corresponding maximal fluid-induced shear stress exerted by the culture medium was evaluated to range from 0 to 0.08 Pa which lies within the values reported to stimulate bone cells [61, 84, 132, 150, 181]. Consequently, the fluid motion inside the PLLA-5%βTCP constructs could favor its osteoinduction and osteogenesis when stimulated below its fatigue limit.

In addition, the poroelastic model permitted systematic screening of the impact of the construct fluid conductivity and mechanical parameters. An algorithm was proposed to identify the optimal physical parameters that maximize the fluid volume exchange and were associated with fluid-induced shear stresses that are likely to stimulate the embedded bone cells.

At a small length scale (400 μm), the fluid motion inside the construct was considered to be impacted by the dynamic movement of the cell membranes due to fluid induced shear stress. A simple theoretical model was created to highlight the sensitivity of some mechanical parameters. This approach was rewarding as it identified a novel dimensionless number N_{fs} characterizing the coupling phenomenon. The application of this theoretical model to bone cells embedded in a porous construct showed that the pore diameter may greatly impact the effective mechanical stimulus taking place at the cell surface. Indeed, the dynamic shear stress was found to be strongly damped when the pore diameter were smaller than 100 μm. On the other hand, the coupling phenomenon did not significantly damp the interfacial shear stress for constructs with pore diameters larger than 300 μm. Such a construct could perhaps stimulate more efficiently the bone cells that colonize its pores as it seems that they are especially sensitive to high frequency mechanical loading [145, 182]

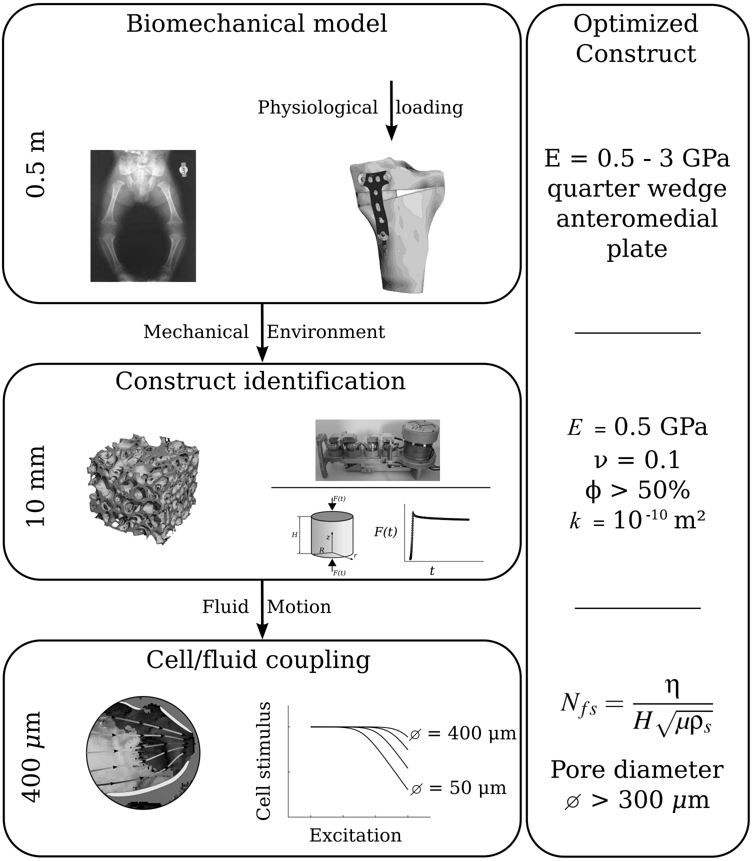
Biomechanical model
0.5 m
Physiological loading
Mechanical Environment
Construct identification
10 mm
F(t)
H
z
R
r
F(t)
F(t)
t
Fluid Motion
Cell/fluid coupling
400 μm
Cell stimulus
∅ = 400 μm
∅ = 50 μm
Excitation
Optimized Construct
E = 0.5 - 3 GPa
quarter wedge
anteromedial
plate
E = 0.5 GPa
ν = 0.1
ϕ > 50%
k = 10^-10 m^2
N_fs = η / (H √(μρ_s))
Pore diameter
∅ > 300 μm

Figure 5.1: Schematic representation of the thesis' principal results.

5.2 Perspectives

As mentioned in the previous section, this study permitted the identification of some biomechanical properties that are essential to the development of an efficient tissue engineered bone construct. It also raised questions that could perhaps be the subject of further investigations.

At the large length scale (0.5 m), possible extensions of the open wedge tibial osteotomy model would be to take into account the poroelastic properties of the bone and wedge and to apply the loads taking place during a whole gait cycle. Indeed, the role of the fluid motion was identified to be central for the development of an efficient bone construct. Pursuing this approach, optimal construct fluid conductivity and mechanical characteristics could be investigated, taking into account fluid flow exchange between the construct and the trabecular bone. As the fluid flow at the bone/construct interface is likely to transport mesenchymal stem cell from the bone to the construct it could significantly enhance construct osteoinduction. The full gait cycle loading would give a realistic dynamic loading for the optimization of the wedge fluid conductivity.

At the intermediate length scale (10 mm), a natural extension of the research would be to continue investigating the PLLA-5%βTCP construct's mechanical evolution on a time scale of the order of one to two years. The combination of *in vitro* and *in vivo* tests could perhaps quantify the construct mechanical evolution due to the PLLA-5%βTCP degradation through hydrolysis and resorption and due to new bone formation. Ideally, the mechanical evolution would be modeled by including internal variables related to construct resorption and new bone formation. The obtained model could then be used in a particular clinical application to quantify its mechanical evolution.

At the small length scale (400 μm), the experimental validation of the fluid/cell interaction phenomenon may be a challenging goal for future studies. In fact, I have been working on this topic during the past few months and a test bench was setup (see Figure 5.2). Preliminary tests were carried out using digital holography microscopy (Lyncée Tec SA, Lausanne, Switzerland) and a custom flow chamber developed at the Laboratory of Biomechanical Orthopedics EPFL-HOSR. The first results are encouraging and pointed out specific experimental issues that are still open. Nevertheless, the motion of the cell surface could be tracked at high excitation frequencies (up to 50 Hz).

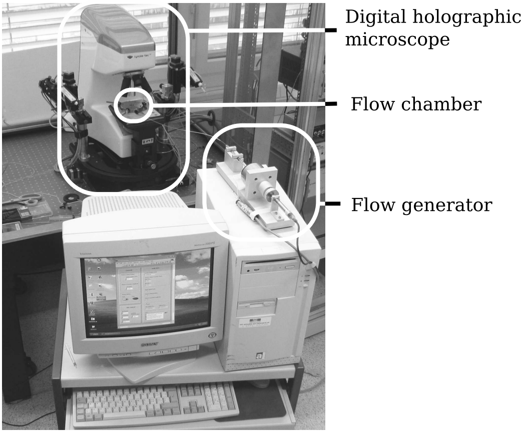

Figure 5.2: Experimental setup for the validation of the fluid/cell interaction theory.

APPENDIX A

Glossary

angiogenesis	The physiological process involving the growth of new blood vessels from pre-existing vessels. It is a normal process in growth and development, as well as in wound healing.
anterior	Toward the front or in front of.
apoptosis	One of the main types of programmed cell death.
arthrodesis	The artificial induction of joint ossification between two bones via surgery
cancellous bone	Porous bone located in the shaft of long bones.
chemotaxis	The movement of an organism or an individual cell, such as leukocyte, in response to a chemical concentration gradient.
compartment syndrom	A group of symptoms which indicate that a nerve, blood vessel or tendon is being constricted due to swelling within a closed anatomic space.
construct	Designate the bone tissue engineered material made of a porous material impregnated with bone cells and saturated with a fluid.
coronal plan	A vertical plan at right angles to a sagittal plan, dividing the body into anterior and posterior portions.
cortical bone	The superficial thin layer of compact bone.
CT	Computed Tomography. It is a medical imaging method that generates a three-dimensional image of the internals of an object from a large series of two-dimensional X-ray images taken around a single axis of rotation.
cytoplasm	The organized complex of inorganic and organic substances external to the nuclear membrane of a cell and including the cytosol and membrane-bound organelles.

cytosol	The fluid portion of the cytoplasm exclusive of organelles and membranes.
differentiated cell	Specialised cell from the morphological and/or physiological point of view.
distal	Situated away from the main part or away from the main part.
DMEM	Dulbecco's Modified Eagle Medium.
EMEA	European Medicines Agency (EMEA) is a European agency for the evaluation of medicinal products.
endoabdominal fascia	The flat layers of fibrous tissue that separate different layers of tissue within the abdomen.
FCS	Fetal Calf Serum.
FDA	The Food and Drug Administration (FDA) is an agency of the United States Department of Health and Human Services and is responsible for regulating food (humans and animal), dietary supplements, drugs (human and animal), cosmetics, medical devices (human and animal) and radiation emitting devices (including non-medical devices), biologics, and blood products in the United States of America.
fibula	A long bone in the lower leg that is adjacent to the tibia.
genotype	Set of genetical material that carries an individual and that consitute its hereditary material.
golden standard	Denotes the reference and, by extension, the most used technique.
immunogenic	Is said of substance's power to induce a immunitary response.
lateral	Farther from the medial plan.
medial	Nearer to the median plan.
median plan	Plan that divides the body into left right portions. Is synonimous to midsagittal plan.
megakaryocyte	Bone marrow cell responsible for the production of blood platelets.
mesenchymal stem cell	Multipotent stem cell that can differentiate into osteoblasts, chondrocytes, myocytes, adipocytes, neuronal cells, beta-pancreatic islets cells. They are produced in the bone marrow.
nucleotide	Monomers of the nucleic acids and are the structural units of RNA and DNA.

osteoarthritis	Noninflammatory degenerative joint disease characterized by degeneration of the articular cartilage, hypertrophy of bone at the margins and changes in the synovial membrane. It is accompanied by pain and stiffness, particularly after prolonged activity.
osteoarthrosis	Sinonymous of osteoarthritis.
osteoconductive	Refers to the ability to provide a support on which bone cells can attach, migrate, grow and divide.
osteogenic	That generates bone tissue formation.
osteoinductive	Refers to the capacity to stimulate primitive stem cells or immature bone cells to differentiate into mature, bone forming cells.
osteointegration	The ability to chemically bond to the surface of bone without an intervening layer of fibrous tissue.
PBS	Phosphate buffered saline.
pheontype	Set of morphologic or fonctional characteristics that defines a species, individual or cell and that results from its genotype together with the action of the enviroment.
PID	Proportional-Integral-Derivative control.
posterior	Situated in back of or in the back part of.
spongious bone	See cancellous bone.
sagittal plan	The longitudinal vertical plan that divides the body into two halves left and right.
sinus lift	Surgery that adds bone or bone substitute to the upper jaw in the molars and premolars area to permit .
total knee arthroplasty	Replacement of the knee joint by a prosthesis.
valgus	Is said of a member that is turned outward away from the midline of the body to an abnormal degree.
varus	is said of a member that is turned inward towards the midline of the body to an abnormal degree.
weight-bearing line	Line drawn from the mid femoral head to mid ankle.

APPENDIX B

Fluid Flow in a Poroelastic Cylinder

This appendix presents the analytical steps necessary to obtain the pore pressure distribution inside a cylindrical poroelastic sample of radius R and height H. The governing equations that result from the simplification of the general linear elastic equations are recalled from section 3.4.

$$(\lambda+2\mu)\frac{\partial}{\partial r}(\nabla\cdot\mathbf{u})=b\nabla p \tag{B.1}$$

$$\frac{\partial^2 w}{\partial z^2}=0 \tag{B.2}$$

$$\frac{\eta}{kM}\frac{\partial p}{\partial t}+\frac{\eta b}{k}\frac{\partial}{\partial t}\nabla\cdot\mathbf{u}=\nabla^2 p \tag{B.3}$$

The boundary and initial conditions are explicitely writen hereafter.

Stress Boundary Conditions

$$2\pi\int_0^R \sigma_{zz}(r,z=H,0<t<t_0)r\,dr=F(t) \tag{B.4}$$

$$\sigma_{rr}(r=R,z,0<t<t_0)=0 \tag{B.5}$$

Displacement Boundary Conditions

$$u(r=0,0<t<t_0)=0 \tag{B.6}$$

$$w(z=0,0<t<t_0)=0 \tag{B.7}$$

Pressure Boundary Conditions The impermeability condition at the sample top and bottom are given by

$$\left.\frac{\partial p}{\partial z}\right|_{z=0}=\left.\frac{\partial p}{\partial z}\right|_{z=H}=0 \tag{B.8}$$

and the free flow condition at outer edge is

$$p(r=R,t)=0 \tag{B.9}$$

Note that the no flow condition (B.8) is fulfilled *a priori* by assumption (3.61)

Initial Conditions

$$u(r,t=0)=0 \qquad w(z,t=0)=0 \qquad p(r,t=0)=0 \tag{B.10}$$

Analytical Resolution

Lets first begin with the easiest, i.e. the solid displacement in z-direction. Equation (B.2) together with boundary condition (B.7) gives

$$w(z,t)=f_1(t)z \tag{B.11}$$

where $f_1(t)$ is a unknown function.

The integration of the solid displacement equation in r-direction (B.1) together with result (B.11) gives a useful relation between the divergence of the displacement and the fluid pressure.

$$\nabla\cdot\mathbf{u}=\frac{1}{r}\frac{\partial}{\partial r}(ur)+f_1(t)=\frac{b}{\lambda+2\mu}p(r,t)+f_2(t) \tag{B.12}$$

with the unknown function $f_2(t)$ appearing after integration. The above relation permit to determine by integration and using the displacement boundary condition (B.6), the radial displacement in function of the pressure and the two unknown functions $f_2(t)$ and $f_1(t)$.

$$u(r,t)=\frac{b}{r(\lambda+2\mu)}\int_0^r r^*p(r^*,t)\,dr^*+\frac{r}{2}(f_2(t)-f_1(t)) \tag{B.13}$$

To determine the unknown functions $f_2(t)$ and $f_1(t)$, the constitutive law (3.57) is injected in the stress boundary conditions (B.4) and (B.5). The use of the relation between the divergence and the fluid pressure (B.12) allow me to rewrite the boundary condition (B.4) as.

$$2\pi\int_0^R\left[\frac{-2\mu b}{\lambda+2\mu}p(r,t)+\lambda f_2(t)+2\mu f_1(t)\right]r\,dr=F(t) \tag{B.14}$$

Thus

$$f_1(t)=\frac{F(t)}{2\pi\mu R^2}-\frac{\lambda}{2\mu}f_2(t)+\frac{2b}{R^2(\lambda+2\mu)}\int_0^R rp(r,t)\,dr \tag{B.15}$$

Thanks to the fact that $p(r=R,t)=p_0$ (boundary condition (B.9)), the boundary condition (B.5) together with relation (B.12) yields to.

$$f_2(t)=-\frac{2\mu}{\lambda}\left.\frac{\partial u}{\partial r}\right|_{r=R} \tag{B.16}$$

Injecting the expression for $u(r,t)$ (B.13) into the right hand side of (B.16) gives

$$f_2(t)=C_0\int_0^R rp(r,t)\,dr+C_1F(t) \tag{B.17}$$

with

$$C_0=\frac{8\mu b}{R^2(\lambda+2\mu)(3\lambda+2\mu)} \tag{B.18}$$

$$C_1=\frac{1}{\pi R^2(3\lambda+2\mu)} \tag{B.19}$$

The equation of fluid movment (B.3) may be rewritten using relation (B.12).

$$\alpha\frac{\partial p(r,t)}{\partial t}+\beta\frac{\partial f_2(t)}{\partial t}=\triangle p(r,t) \tag{B.20}$$

with

$$\alpha=\frac{\eta}{k}\frac{\lambda+Mb^2+2\mu}{M(\lambda+2\mu)} \tag{B.21}$$

$$\beta=\frac{\eta b}{k} \tag{B.22}$$

The relations (B.17) and (B.20) gives a differential equation for $p(r,t)$.

$$\alpha\frac{\partial p(r,t)}{\partial t}+\beta C_0\int_0^R r\frac{\partial p(r,t)}{\partial t}dr+\beta C_1\dot{F}(t)=\triangle p(r.t) \tag{B.23}$$

As the second and third term of the left hand side are function of time only, they are actually the inhomogeneous terms. Lets first consider first the homogeneous part.

$$\alpha\frac{\partial p}{\partial t}=\frac{\partial^2 p}{\partial r^2}+\frac{1}{r}\frac{\partial p}{\partial r} \tag{B.24}$$

Using the method of variable separation $p(r,t)=R(r)T(t)$, equation (B.24) becomes.

$$\alpha\frac{\dot{T}}{T}=\frac{R''}{R}+\frac{R'}{R^2}=-k_n^2 \tag{B.25}$$

Integration of each variable $T(t)$ and $R(r)$ gives the general solution of the form.

$$p_h(r,t)=\sum_{n=1}^{\infty}\left(A_nJ_0(k_nr)+B_nY_0(k_nr)\right)e^{\lambda_nt} \tag{B.26}$$

As the solution shall remain bounded for $r=0$, the coefficients B_n must be zero. Applying the boundary conditions (B.9) determines the coefficients k_n as follows

$$J_0(k_nR)=0\ . \tag{B.27}$$

In order to find the solution of the inhomogeneous equation (B.23), a spectral decomposition is used.

$$p(r,t)=\sum_{n=1}^{\infty}p_n(t)J_0(k_nr) \tag{B.28}$$

Injection of (B.28) in equation (B.23) gives

$$\sum_{n=1}^{\infty}\dot{p}_n\left[\alpha J_0(k_nr)+\beta C_0\frac{R}{k_n}J_1(k_nR)\right]+\sum_{n=1}^{\infty}p_n\left[k_n^2J_0(k_nr)\right]=-\beta C_1\dot{F}(t) \tag{B.29}$$

Multiplication by $J_0(k_mr)$ and integration over the domain yields to an inhomogeneous system of first order ordinary differential equation for $\mathbf{p}_n$ with constant coefficients.

$$\mathbf{A}\dot{\mathbf{p}}(t)+\mathbf{B}\mathbf{p}(t)=\mathbf{f}_p(t) \tag{B.30}$$

Where $\mathbf{p}$ is a column vector of dimension n of unknown functions. Finally, the vector $\mathbf{f}_p(t)$ containes the inhomogeneities.

$$\mathbf{f}_p(t) = -\beta C_1 \dot{F}(t) \begin{Bmatrix} \frac{R}{k_1} J_1(k_1 R) \\ \vdots \\ \frac{R}{k_n} J_1(k_n R) \end{Bmatrix} \tag{B.31}$$

The matrix $\mathbf{A}$ is formed by the following terms.

$$\mathbf{A} = \begin{cases} \left(\frac{1}{2}\alpha R^2 + \beta C_0 \frac{R^2}{k_n^2}\right) J_1^2(k_n R) & n = m \\ \beta C_0 \frac{R}{k_m} J_1(k_m R) \frac{R}{k_n} J_1(k_n R) & m \neq n \end{cases} \tag{B.32}$$

and $\mathbf{B}$ is a diagonal matrice which diagonal terms are given by

$$B_{nn} = \frac{1}{2} k_n^2 R^2 J_1^2(k_n R) \; . \tag{B.33}$$

The system of ordinary first order differential equations (B.30) has n solution of the form

$$\mathbf{p}(t) = \mathbf{p}_h(t) + \mathbf{p}_p(t) \tag{B.34}$$

where the $\mathbf{p}_h(t)$ is the solution of the corresponding homogeneous system

$$\mathbf{A}\dot{\mathbf{p}}_h(t) + \mathbf{B}\mathbf{p}_h(t) = 0 \tag{B.35}$$

and $\mathbf{p}_p(t)$ is the particular solution. The homogeneous solution of the ODE system (B.30) is determined by the Euler method [101] and has the following form.

$$\mathbf{p}_h(t) = \mathbf{X}(t)\mathbf{c} \tag{B.36}$$

where $\mathbf{c}$ is a vector containing n constant coefficient and $\mathbf{X}$ is the matrix of the homogeneous solution basis.

$$\mathbf{X} = \left[\mathbf{u}_1 e^{\lambda_1 t} \cdots \mathbf{u}_n e^{\lambda_n t}\right] \tag{B.37}$$

The λ_i and $\mathbf{u}_i$ are the i-th eigenvalue resp. eigenvector of matrice $-\mathbf{A}^{-1}\mathbf{B}$. The particular solutions $\mathbf{p}_p(t)$ of the system (B.30) has the following form [101]

$$\mathbf{p}_p(t) = \mathbf{X}(t)\mathbf{d}(t) \tag{B.38}$$

where $\mathbf{d}(t)$ are n unknown functions. Injecting the particular solution (B.38) in the system of ODE (B.30) gives

$$\mathbf{d}(t)\left(\dot{\mathbf{X}} + \mathbf{A}^{-1}\mathbf{B}\mathbf{X}\right) + \mathbf{X}\dot{\mathbf{d}}(t) = \mathbf{A}^{-1}\mathbf{f}_p(t) \tag{B.39}$$

As $\dot{\mathbf{X}} + \mathbf{A}^{-1}\mathbf{B}\mathbf{X} = 0$ (B.35), I obtain

$$\dot{\mathbf{d}}(t) = \mathbf{X}^{-1}\mathbf{A}^{-1}\mathbf{f}_p(t) \tag{B.40}$$

Integration of (B.40) gives the expression for $\mathbf{d}(t)$. The particular solutions are thus

$$\mathbf{p}_p(t) = \mathbf{X}(t)\Upsilon(t) \tag{B.41}$$

where the $\Upsilon(t)$ is the primitive of $\mathbf{X}^{-1}\mathbf{A}^{-1}\mathbf{f}_p(t)$.

$$\Upsilon(t) = \int_0^t \mathbf{X}^{-1}\mathbf{A}^{-1}\mathbf{f}_p(\tau)\,d\tau + \mathbf{c}_p \tag{B.42}$$

Thus the solutions of the system of inhomogeneous ordinary differential equation (B.30) are

$$\mathbf{p}(t) = \mathbf{X}(t)\left(\mathbf{c}^* + \int_0^t \mathbf{X}^{-1}\mathbf{A}^{-1}\mathbf{f}_p(\tau)\,d\tau\right) \tag{B.43}$$

where $\mathbf{c}^*$ is sum of constant coeffîcent vector $\mathbf{c}$ of equation (B.36) and the constants vector $\mathbf{c}_p$ appearing after integration of equation (B.40).Finally the coefficents $\mathbf{c}^*$ are detemined with the initial condition for the pressure $p(t=0)=0$ (B.10). As the matrix $\mathbf{X}$ is not zero at $t=0$, the second term shall be equal to zero at time $t=0$.

$$\mathbf{c}^* + \left[\int_0^t \mathbf{X}^{-1}\mathbf{A}^{-1}\mathbf{f}_p(\tau)\,d\tau\right]_{t=0} = 0 \tag{B.44}$$

Because the second term is zero, the vector coefficient $\mathbf{c}^*$ is equal to zero. Therefore, the solution of equations (B.30) are.

$$\mathbf{p}(t) = \mathbf{X}(t)\left(\int_0^t \mathbf{X}^{-1}\mathbf{A}^{-1}\mathbf{f}_p(\tau)\,d\tau\right)\ . \tag{B.45}$$

The total pore pressure is thus given by

$$p_{tot}(r,t) - p_0 = \sum_{n=1}^{\infty} p_n(t) J_0(k_n r) \tag{B.46}$$

where the $p_n(t)$ are the n-th function of the vector defined by equation (B.45). Knowing the pore pressure, it may be injected in equation (B.15) and (B.17) which may be in turn injected in (B.13) and (B.11) to have the solution for the displacements. The general forms for the solid skeleton displacement are.

$$\begin{aligned} u(r,t) &= \frac{b}{\lambda+2\mu}\sum_{n=1}^{\infty}\frac{p_n(t)}{k_n}J_1(k_n r) \\ &\quad - \left[\frac{b(\lambda-2\mu)}{R(\lambda+2\mu)(3\lambda+2\mu)}\sum_{n=1}^{\infty}\frac{p_n(t)}{k_n}J_1(k_n R) + \frac{F(t)}{\pi R^2}\frac{\lambda}{2\mu(3\lambda+2\mu)}\right] r \\ w(z,t) &= \left[\frac{F(t)}{\pi R^2}\frac{\lambda+\mu}{\mu(3\lambda+2\mu)} + \frac{2b}{R(3\lambda+2\mu)}\sum_{n=1}^{\infty}\frac{p_n(t)}{k_n}J_1(k_n R)\right] z \end{aligned}$$

The stress tensor is diagonal and given by

$$\begin{aligned}
\sigma_{rr}(r,t) &= -\frac{2b\mu}{R(\lambda+2\mu)}\sum_{n=1}^{\infty}\frac{p_n(t)}{k_n}\left(\frac{R}{r}J_1(k_n r)-J_1(k_n R)\right)\\
\sigma_{\theta\theta}(r,t) &= \frac{F(t)}{\pi R^2}\frac{\lambda}{3\lambda+2\mu}-\frac{2b\mu}{R(\lambda+2\mu)}\sum_{n=1}^{\infty}\frac{p_n(t)}{k_n}\left[Rk_nJ_0(k_n r)-\frac{4\lambda}{(3\lambda+2\mu)}J_1(Rk_n)\right]\\
\sigma_{zz}(r,t) &= \frac{F(t)}{\pi R^2}-\frac{2\mu b}{R(\lambda+2\mu)}\sum_{n=1}^{\infty}\frac{p_n(t)}{k_n}\left(Rk_nJ_0(k_n r)-2J_1(k_n R)\right)
\end{aligned}$$

APPENDIX C

Average Wall Shear Stress

The fluid conductivity inside a linear porous medium was found to be governed by Darcy's Law (3.51) which was derived from continuum mechanics in chapter 3. However, the Darcy's law may also be obtained using the averaging theory applied to poroelastic medium [11].

First, the averaging of microscopic mass balance equation together with the assumption that the inertial forces and the viscous drag forces inside the fluid are negligible in comparison of the viscous drag forces at the fluid/solide interface yields to the definition of the intrinsic permeability **k** in function to geometric parameters.

$$\mathbf{k} = \frac{\phi \Delta_f^2}{C_f} \alpha^{-1} \mathbf{T} \tag{C.1}$$

The porosity is denoted by ϕ, Δ_f is the hydraulic radius, C_f is the macroscopic dimensionless shape factor, α is a matrix characterizing the configuration of the interface surface between fluid and solid, and **T** is the tortuosity tensor.

Second, the average shear stress exerted by the fluid at the fluid/solid interface is given by [11]

$$\bar{\tau} = -\eta \frac{\phi^2}{\Sigma_{fs}} \mathbf{T} \mathbf{k}^{-1} \mathbf{q}_r \ , \tag{C.2}$$

where Σ_{fs} is the specific surface of the fluid/solid interface, η is the fluid viscosity, $\mathbf{q}_r$ is the fluid mass flux relative to the solid skeleton. For isotropic material the tortuosity tensor reduces to

$$\mathbf{T} = \frac{\phi^s}{\phi} \mathbf{I} \tag{C.3}$$

where ϕ^S is the surface porosity. Finally, the equation (C.2) simplifies to:

$$\bar{\tau} = -\frac{\eta}{k} \frac{\phi \phi^S}{\Sigma_{fs}} \bar{\mathbf{v}}^f \tag{C.4}$$

where $\bar{\mathbf{v}}^f$ is the fluid velocity relative to the solid skeleton, and k is the isotropic permeability.

APPENDIX D

Analytical Solution of the Cell/fluid Interaction Problem

The detailed resolution of the cell/fluid interaction problem is exposed here. I first recall the simplified governing equations from chapter 4 together with the boundary and initial conditions. Then, the mathematical resolution is presented.

Governing Equations

fluid continuity
$$\frac{\partial v_2}{\partial x_2} = 0 \tag{D.1}$$

fluid Navier-Stokes in x_1
$$\frac{\partial p}{\partial x_1} = \eta \frac{\partial^2 v_1}{\partial x_2^2} \tag{D.2}$$

fluid Navier-Stokes in x_2
$$\frac{\partial p}{\partial x_2} = \eta \frac{\partial^2 v_2}{\partial x_2^2} \tag{D.3}$$

cell force equilibrium in x_1
$$\frac{\partial^2 u_1}{\partial t^2} = a^2 \frac{\partial^2 u_1}{\partial x_2^2} \tag{D.4}$$

cell force equilibrium in x_2
$$\frac{\partial^2 u_2}{\partial t^2} = a_2^2 \frac{\partial^2 u_2}{\partial x_2^2} \tag{D.5}$$

with $a^2 = \dfrac{\mu}{\rho_{s0}}$ and $a_2^2 = \dfrac{(\lambda + 2\mu)}{\rho_{s0}}$

Initial Conditions

fluid
$$\mathbf{v}(x_2, 0) = 0 \tag{D.6}$$

cell
$$\mathbf{u}(x_2, 0) = 0 \tag{D.7}$$

$$\frac{\partial \mathbf{u}}{\partial t}(x_2, 0) = 0 \tag{D.8}$$

Boundary Conditions

fluid's upper boundary $$v_1\,(H+h,t) = v_0 \sin\omega_0 t \tag{D.9}$$

$$v_2\,(H+h,t) = 0 \tag{D.10}$$

$$p(H+h,t) = 0 \tag{D.11}$$

cell's lower boundary $$u_1(0,t) = 0 \tag{D.12}$$

$$u_2(0,t) = 0 \tag{D.13}$$

kinetic coupling $$v_1\,(h(t),t) = \frac{\partial u_1}{\partial t}\,(h(t),t) \tag{D.14}$$

$$v_2\,(h(t),t) = \frac{\partial u_2}{\partial t}\,(h(t),t) \tag{D.15}$$

dynamic coupling $$\frac{\partial v_1}{\partial x_2}\,(h(t),t) = \frac{\mu}{\eta}\frac{\partial u_1}{\partial x_2}\,(h(t),t) \tag{D.16}$$

$$p(h(t),t) = \eta\frac{\partial v_2}{\partial x_2}\,(h(t),t) - (\lambda+2\mu)\frac{\partial u_2}{\partial x_2}\,(h(t),t) \tag{D.17}$$

Solving Procedure

Fluid

Injecting the continuity equation (D.1) into the Navier-Stokes equation in x_2 direction (D.3) gives

$$\frac{\partial p}{\partial x_2} = 0\,. \tag{D.18}$$

Solving above equation with the boundary condition (D.11) yields to

$$p = 0\,. \tag{D.19}$$

The solution of the continuity equation (D.1) with boundary condition (D.10) is then

$$v_2 = 0\,. \tag{D.20}$$

Finally, the Navier-Stokes in x_1 direction (D.2) together with boundary condition (D.9) gives the velocity in x_1 direction.

$$v_1(x_2,t) = C(t)x_2 + [v_0 \sin\omega_0 t - C(t)\,(H+h)] \tag{D.21}$$

Solid

Thanks to the fact that the pressure is zero in the whole fluid (D.19), the force equilibrium equation in x_2 direction (D.5) becomes homogeneous with the following general solution

$$u_2(x_2,t) = (A_2\cos k_2 a_2 t + B_2 \sin k_2 a_2 t)(C_2 \cos k_2 x_2 + D_2 \sin k_2 x_2)\,. \tag{D.22}$$

According to the initial conditions (D.7, D.8), the coefficient A_2 and B_2 shall be zero. The deformation in x_2 direction is thus zero inside the cell layer and for any time $t \geq 0$.

$$u_2(x_2,t) = 0 \tag{D.23}$$

Therefore, the interface position is constant and equal to its initial position h.

$$h(t) = h \tag{D.24}$$

To solve the force equilibrium equation in x_1 direction (D.4) with the inhomogeneous boundary condition at the interface between the cell and the fluid (D.12), a change of variable is necessary. As the shear stress τ is only dependent on the time, the following change of variable is possible

$$u_1(x_2,t) = \tilde{u}(x_2,t) + \frac{\tau(t)}{\mu}x_2\ . \tag{D.25}$$

The force equilibrium in x_1 (D.4) becomes thus

$$\frac{\partial^2 \tilde{u}}{\partial t^2} = a^2 \frac{\partial^2 \tilde{u}}{\partial x_2^2} - \frac{\ddot{\tau}}{\mu}x_2\ , \tag{D.26}$$

and has homogeneous boundary conditions

$$\tilde{u}(0,t) = 0 \tag{D.27}$$

$$\frac{\partial \tilde{u}}{\partial x_2}(h,t) = 0\ . \tag{D.28}$$

The initial conditions (D.7-D.8) become then

$$\tilde{u}(x_2,0) = -\frac{\tau(0)}{\mu}x_2 \tag{D.29}$$

$$\frac{\partial \tilde{u}}{\partial t}(x_2,0) = -\frac{\dot{\tau}(0)}{\mu}x_2\ . \tag{D.30}$$

The function $\tilde{u}$ may then be split into two functions

$$\tilde{u}(x_2,t) = w_1(x_2,t) + w_2(x_2,t)\ ,$$

where w_1 is the solution of the non homogeneous differential equation (D.26) with homogeneous initial conditions, and w_2 is the solution of the homogeneous differential equation i.e. $(\tau = 0)$, with non homogeneous initial conditions (D.29,D.30) [101]. The first term is given by

$$w_1(x_2,t) = \sum_{n=1}^{\infty} T_n(t) \sin k_n x_2 \tag{D.31}$$

with

$$k_n = \frac{\pi}{2h}(2n-1) \qquad k_n = 1,2,... \tag{D.32}$$

$$T_n(t) = \frac{2(-1)^n}{k_n^3 a h \mu} \int_0^t \dot{\tau}(s) \sin k_n a(t-s) ds\ . \tag{D.33}$$

The second term is given by

$$w_2(x_2,t) = \frac{2}{h\mu}\sum_{n=1}^{\infty}\frac{(-1)^n}{k_n^2}\left(\tau(0)\cos k_n at + \frac{\dot{\tau}(0)}{k_n a}\sin k_n at\right)\sin k_n x_2\ . \tag{D.34}$$

Putting all together gives the solution of the displacement in the solid in function of τ.

$$\begin{aligned} u_1(x_2,t) = &\sum_{n=1}^{\infty} T_n(t,\tau(t))\sin k_n x_2 \\ &+ \frac{2}{h\mu}\sum_{n=1}^{\infty}\frac{(-1)^n}{k_n^2}\left(\tau(0)\cos k_n at + \frac{\dot{\tau}(0)}{k_n a}\sin k_n at\right)\sin k_n x_2 \\ &+ \frac{\tau(t)}{\mu}x_2 \end{aligned} \tag{D.35}$$

Injecting the above solution for u_1 (D.35), the fluid velocity given by (D.21) into the dynamic coupling condition (D.16) gives following condition for $C(t)$ of equation (D.21).

$$C(t) = \frac{\tau(t)}{\eta} \tag{D.36}$$

This definition coupled with the fluid's initial condition (D.6) gives the initial condition for the interfacial shear stress.

$$\tau(0) = 0 \tag{D.37}$$

Injection of equations (D.21,D.35, D.36) into the kinetic coupling condition (D.14) gives an equation for $\tau(t)$.

$$\begin{aligned} v_0\sin\omega_0 t - \frac{H}{\eta}\tau(t) = -\frac{d}{dt}&\left(\sum_{n=1}^{\infty}\frac{2}{k_n^3 ah\mu}\int_0^t \ddot{\tau}(s)\sin k_n a(t-s)ds\right) \\ &-\frac{2}{h\mu}\sum_{n=1}^{\infty}\frac{\dot{\tau}(0)}{k_n^2}\cos k_n at + \frac{h}{\mu}\dot{\tau}(t) \end{aligned} \tag{D.38}$$

The above equation shall then be solved for τ, which is further discussed in chapter 4.

APPENDIX E

Derivation of N_{fs}

I expose here the detailed mathematical steps necessary to obtain the explicit expression of the interfacial shear stress (4.22) from the coupling equation (4.16). Then, the derivation of dimensionless number N_{fs} is exposed.

Interfacial Shear Stress

As explained in chapter 4, the resolution's first step in the equation for the interfacial shear stress (4.16) is the isolation of τ using the Laplace transformation. However, the inverse Laplace transformation of the expression (4.17) is then rather difficult. Therefore, the infinite series of expression (4.17) is approached by its first term. The Laplace transformed interfacial shear stress is then given

$$\mathcal{L}\left\{\tau(t)\right\} = \frac{v_0\omega_0}{\omega^2+\omega_0^2}\cdot\frac{\omega^2+\omega_1^2}{(\beta-\alpha_1)\omega^3+\gamma\omega^2+\beta\omega_1^2\omega+\gamma\omega_1^2}\ , \tag{E.1}$$

with

$$\omega_1 = \frac{\pi}{2h}\sqrt{\frac{\mu}{\rho_s}},\quad \alpha_1 = \frac{8h}{\pi^2\mu},\quad \beta = \frac{h}{\mu},\quad \gamma = \frac{H}{\eta},\quad \mu = \frac{E}{2(1+\nu)}\ . \tag{E.2}$$

The Laplace transformed interfacial shear stress (E.1) has five poles. The first two are complex conjugates and are given by

$$s_0 = \overline{s_1} = i\sqrt{\omega_0} \tag{E.3}$$

The last three poles are solutions of the third degree polynomial

$$\omega^3 + a_2\omega^2 + a_1\omega + a_0\ , \tag{E.4}$$

with

$$a_2 = \frac{\pi^2 H\mu}{(\pi^2-8)h\eta},\quad a_1 = \frac{\pi^4\mu}{4(\pi^2-8)h^2\rho_s},\quad a_0 = \frac{\pi^4 H\mu^2}{4(\pi^2-8)h^3\eta\rho_s}. \tag{E.5}$$

The number of roots of the polynomial (E.4) is determined by the sign of the polynomial discriminant D given by

$$D = Q^2 - P^3 \ , \tag{E.6}$$

with

$$Q = \frac{a_2 a_1}{6} - \frac{a_0}{2} - \frac{a_2^3}{27} \quad \text{and} \quad P = \frac{a_2^2}{9} - \frac{a_1}{3} \ . \tag{E.7}$$

By rewriting (E.6) in function of η, μ, ρ_s, H, h using equations (E.5,E.7), the polynomial discriminant D appears to be greater than zero for all η, μ, ρ_s, H, h greater than zero. Thus, the polynomial (E.4) has one real root and the two complex conjugate roots.

$$s_2 \in \mathbf{R}, \quad s_3 = \overline{s_4} \in \mathbf{C} \tag{E.8}$$

The explicit expression of these poles is given by Cardano's method[1]

$$\begin{aligned} s_2 &= -\tfrac{a_2}{3} + A + B \\ s_{3,4} &= -\tfrac{a_2}{3} - \tfrac{1}{2}(A+B) \pm i\tfrac{\sqrt{3}}{2}(A-B) \end{aligned} \ , \tag{E.9}$$

with

$$A = \sqrt[3]{Q + \sqrt{D}}, \quad B = \frac{P}{A} \ , \tag{E.10}$$

Using the poles' definition (E.3) and (E.8), the inverse Laplace transform of (E.1) can be written in a compact form as

$$\tau(t) = \tau \sin(\omega_0 t + \delta) + g(t) \ . \tag{E.11}$$

Let's first have a look at the function $g(t)$, which is in fact composed of two components

$$g(t) = g_1(t) + g_2(t) \ , \tag{E.12}$$

with following expressions

$$\begin{aligned} g_1(t) &= \frac{v_0 \omega_0}{\beta - \alpha_1} \frac{\left(s_2^2 + \omega_1^2\right) e^{s_2 t}}{\left(s_2^2 + \omega_0^2\right)(s_2 - s_3)(s_2 - \overline{s_3})} \\ g_2(t) &= \frac{v_0 \omega_0}{\beta - \alpha_1} \left[\frac{\left(s_3^2 + \omega_1^2\right) e^{s_3 t}}{\left(s_3^2 + \omega_0^2\right)(s_3 - s_2)(s_3 - \overline{s_3})} + \frac{\left(\overline{s_3}^2 + \omega_1^2\right) e^{\overline{s_3} t}}{\left(\overline{s_3}^2 + \omega_0^2\right)(\overline{s_3} - s_2)(\overline{s_3} - s_3)} \right] \end{aligned} \tag{E.13}$$

The first function vanishes exponentially because the real pole s_2 is negative for all positive η, μ, ρ_s, H, h. The proof can be formulated in word as follows. As the polynomial (E.4) exhibits a positive discriminant, there is only one real root. In addition, the sign of this unique real root has a sign opposite to the polynomial's sign at $\omega = 0$. As a_0 is bigger then zero far all η, μ, ρ_s, H, $h > 0$, the unique real root is smaller than zero.

The second function $g_2(t)$ also vanishes exponentially with time. Indeed, after some algebra, $g_2(t)$ appears to be proportional to

$$g_2(t) \propto e^{\Re(s_3)t} \tag{E.14}$$

---

[1] Although the method was first discovered by Scipione de Ferro (1465-1526), it was first published by Cardano (1501-1576) in his treatise *Ars Magna*.

and the real part of the third pole is smaller than zero.

$$\Re(s_3) \in \left[-\frac{a_2}{2}, 0\right[\quad \forall\, \eta, \mu, \rho_s, H, h > 0 \tag{E.15}$$

In summary, g_1 and g_2 vanish exponentially with time. Consequently, the term $g(t)$ models the transient response of the system, and may be neglected for stationary regimes. In this case, the interfacial shear stress becomes

$$\tau(t) = \tau \sin(\omega_0 t + \delta)\ , \tag{E.16}$$

where the interfacial shear stress magnitude τ and the phase shift δ are given by

$$\tau = \frac{\pi^2 \mu v_0}{(\pi^2 - 8)h} \frac{\omega_0^2 + \omega_1^2}{\sqrt{c_1^2 + c_2^2}} \qquad \tan\delta = \left(\frac{c_1}{c_2}\right)\ , \tag{E.17}$$

with

$$\begin{aligned} c_1 &= \omega_0 \left[\omega_0^2 - |s_3|^2 - 2 s_2 \Re(s_3)\right] \\ c_2 &= \omega_0^2 \left[2\Re(s_3) + s_1\right] - s_2 |s_3|^2\ . \end{aligned} \tag{E.18}$$

Injecting the poles' expression (E.9) in the expression for interfacial shear stress magnitude (E.17) yields to an explicit expression for the shear stress magnitude τ. It is then made dimensionless through division by the steady wall shear stress given by $\tau_0 = \dfrac{\eta v_0}{H}$.

$$\tau^* = \frac{\pi^2 \mu H}{(\pi^2 - 8) h \eta} \frac{\omega_0^2 + \omega_1^2}{\sqrt{\omega_0^6 + J_2 \omega_0^4 + J_1 \omega_0^2 + J_0}} \tag{E.19}$$

with

$$\begin{aligned} J_2 &= \frac{\pi^4}{2(\pi^2 - 8)^2} \frac{\mu}{h^2 \eta^2 \rho_s} \left[2H^2 \mu \rho_s - \eta^2 (\pi^2 - 8)\right] \\ J_1 &= -\frac{\pi^6}{16(\pi^2 - 8)^2} \frac{\mu^2}{h^4 \eta^2 \rho_s^2} \left(8H^2 \mu \rho_s - \eta^2 \pi^2\right) \\ J_0 &= \left[\frac{\pi^4 H \mu^2}{4(\pi^2 - 8) h^3 \rho_s \eta}\right]^2 \end{aligned} \tag{E.20}$$

Note that the dimensionless interfacial shear stress magnitude τ^* is always positive. In addition, τ^* is equal to one for $\omega_0 = 0$, and tends towards zero for infinite excitation frequency ω_0. Finally, let's verify that the sixth order polynomial under the square root of equation (E.19) has no real root for all $\omega_0 \geq 0$ and for all η, H, h, $\rho_s > 0$. With help of the change of variable $X = \omega_0^2$, the sixth order polynomial reduces to a third order polynomial.

$$p_3(X) = X^3 + J_2 X^2 + J_1 X + J_0 \tag{E.21}$$

The discriminant of (E.21) is always strictly positive for positive real value of η, H, μ and ρ_s. Therefore, only one real root X_0 exists. Similarly to the line of thought taken a few lines above, the sign of this real root is opposite to the sign of the polynomial's value at $X = 0$. As

$$p_3(X = 0) = J_0 > 0 \quad \forall\, \eta, \mu, \rho_s, H, h > 0\ , \tag{E.22}$$

the only real root of (E.21) is smaller than one. Consequently, the polynomial (E.21) is positive for all values of $X > 0$. In conclusion, the dimensionless interfacial shear stress magnitude $\tau*$ has no singularities for all $\omega_0 \geq 0$ and for all η, H, h, $\rho_s > 0$.

Dimensionless number N_{fs}

To have a better idea on the variation of dimensionless interfacial shear stress magnitude τ^* with excitation frequency ω_0, the extrema shall be determined.

$$\frac{\partial \tau^*}{\partial \omega_0} = 0 \tag{E.23}$$

First, let's write the first derivative of τ^*.

$$\frac{\partial \tau^*}{\partial \omega_0} = -\frac{\pi^2}{\pi^2 - 8}\frac{\mu H}{\eta h}\frac{\omega_0\left[\omega_0^6 + 3\omega_1^2\omega_0^4 + \left(2\omega_1^2 J_2 - J_1\right)\omega_0^2 + \left(\omega_1^2 J_1 - 2J_0\right)\right]}{\sqrt{\left(\omega_0^6 + J_2\omega_0^4 + J_1\omega_0^2 + J_0\right)^3}} \tag{E.24}$$

Note that the denominator of the first derivative is positive. Indeed, the sixth order polynomial under the square root is the same as the one studied above. Therefore, the behavior of equation (E.24) is determined by the sixth order polynomial at the numerator. Introducing the change of variable $X = \omega_0^2$ reduces the sixth order polynomial to the following third order polynomial.

$$p_{p,3}(X) = X^3 + 3\omega_1^2 X^2 + \left(2\omega_1^2 J_2 - J_1\right)X + \left(\omega_1^2 J_1 - 2J_0\right) \tag{E.25}$$

The discriminant D_p of the above polynomial may be positive, zero or negative for positive values of η, H, h, $\rho_s > 0$. Three cases shall be distinguished.

Case 1

$$D_p > 0 \quad \Leftrightarrow \quad 0 \leq \frac{\eta}{H\sqrt{\mu\rho_s}} < C_1 \tag{E.26}$$

with $C_1 = 1.0147695$. In that case, the polynomial (E.25) has one positive real root if, and only if $\left(\omega_1^2 J_1 - 2J_0\right) < 0$. The last condition is fulfilled for all $\eta < 4/\pi H\sqrt{\mu\rho_s}$, which is the case. Thus, τ^* has one and only one maximum located at

$$\omega_{0,max} = \sqrt{\sqrt[3]{Q_p + \sqrt{D_p}} + \frac{P_p}{\sqrt[3]{Q_p + \sqrt{D_p}}} - \frac{1}{3}\left(\omega_1^2 J_1 - 2J_0\right)}\ , \tag{E.27}$$

where

$$\begin{aligned} Q_p &= \frac{1}{2}\omega_1^2(2\omega_1^2 J_2 - J_1) - \frac{1}{2}\omega_1^2 J_1 + J_0 - \omega_1^6 \\ P_p &= \omega_1^4 - \frac{2}{3}\omega_1^2 J_2 + \frac{1}{3}J_1\ . \end{aligned} \tag{E.28}$$

Furthermore, function τ^* is monotonously increasing from 1 to the maximum, and then is monotonously decreasing and tend to 0 for $\omega_0 \to +\infty$.

Case 2

$$Dp = 0 \quad \Leftrightarrow \quad \frac{\eta}{H\sqrt{\mu\rho_s}} = C_1 \tag{E.29}$$

with $C_1 = 1.0147695$. In this case the polynomial (E.25) has two real roots, which are

$$\begin{aligned} X_{0,1} &= C_2 \frac{\mu}{\rho_s h^2}\,, \\ X_{0,2} &= -C_3 \frac{\mu}{\rho_s h^2}\,, \end{aligned} \tag{E.30}$$

with $C_1 \approx 5.652$ and $C_3 \approx 6.527$. Thus, the function τ^* has only one extremum in this case, which is located at

$$\omega_{0,max} = C_4 \sqrt{\frac{\mu}{\rho_s h^2}}\,, \tag{E.31}$$

with $C_4 \approx 2.377$.

Case 3

$$Dp < 0 \quad \Leftrightarrow \quad \frac{\eta}{H\sqrt{\mu\rho_s}} > C_1 \tag{E.32}$$

with $C_1 = 1.0147695$. In this case the polynomial (E.25) has three real solutions. As the polynomial's center of symmetry is located at $X_{sym} = -\omega_1^2$ which is negative, there exists at most two positive roots. In addition, if the polynomial takes a negative value at $\omega_0 = 0$, i.e. $\left(\omega_1^2 J_1 - 2J_0\right) < 0$, there exists only one positive root. On the other hand, when $\left(\omega_1^2 J_1 - 2J_0\right) > 0$ there are either two or no real positive roots. Finally, if $\left(\omega_1^2 J_1 - 2J_0\right) > 0$ and the location of the local minimum of polynomial (E.25) is positive, there are two real positive roots. The location of the local minimum is given by

$$\omega_{min} = \sqrt{-\omega_1^2 + \sqrt{P_p}}\,. \tag{E.33}$$

ω_{min} is a real number for $\eta > C_5 H\sqrt{\mu\rho_s}$, with $C_5 \approx 0.960$. Lets recall that the condition $\left(\omega_1^2 J_1 - 2J_0\right) > 0$ is equivalent to $\eta > 4/\pi H\sqrt{\mu\rho_s}$. The intersection of the two conditions is thus given by the last condition. As a result, the function τ^* has two extrema when

$$\frac{\eta}{H\sqrt{\mu\rho_s}} > \frac{4}{\pi}\,, \tag{E.34}$$

and one extremum for

$$\frac{\eta}{H\sqrt{\mu\rho_s}} < \frac{4}{\pi}\,, \tag{E.35}$$

References

[1] Annual Report. Technical report, Aastrom Biosciences, Inc., 2005.

[2] L. A. Abraham and E. J. MacKie. Modulation of osteoblast-like cell behavior by activation of protease-activated receptor-1. *Journal of Bone and Mineral Research*, 14(8):1320–1329, 1999.

[3] A. M. Ahmed and D. L. Burke. In-vitro measurement of static pressure distribution in synovial joints - part i: tibial surface of the knee. *Journal of Biomechanical Engineering*, 105(3):216–225, August 1983.

[4] E. D. Arrington, W. J. Smith, H. G. Chambers, A. L. Bucknell, and N. A. Davino. Complications of iliac crest bone graft harvesting. *Clinical Orthopaedics and Related Research*, 329:300–309, 1996.

[5] M. Asik, C. Sen, B. Kilic, S. B. Goksan, F. Ciftci, and O.F. Taser. High tibial osteotomy with Puddu plate for the treatment of varus gonarthrosis. *Knee Surgury, Sports Traumatolgy, Arthroscopy*, 14(10):948–954, 2006.

[6] N. P. Badhe and I. W. Forster. High tibial osteotomy in knee instability: the rationale of treatment and early results. *Knee Surgery, Sports Traumatology, Arthroscopy*, 10(1):38–43, January 2002.

[7] K. A. Barbee. Role of subcellular shear-stress distributions in endothelial cell mechanotransduction. *Annals of Biomedical Engineering*, 30(4):472–482, 2002.

[8] F. A. Barber and W. D. Dockery. Long-term absorption of poly-L-lactic Acid interference screws. *Arthroscopy*, 22(8):820–826, 2006.

[9] E. Barrett-Connor, D. Black, J.-P. Bonjour, J. Dequeker, G. E. Ehrlich, S. R. Eis, H. K. Genant, C. G. Gennari, O. Johnell, J. Kanis, U. A. Liberman, B. Masri, C. A. Mautalen, P. J. Meunier, P. D. Miller, H. Morii, G. Poor I. Reid, B. SankaranB A. D. Woolf, W. Yu, T. Gruber-Tabsoba, and N. Khaltaev. Prevention and management of osteoporosis. *World Health Organization - Technical Report Series*, 921, 2003.

[10] N. Basso and J. N. M. Heersche. Characteristics of in vitro osteoblastic cell loading models. *Bone*, 30(2):347–351, 2002.

[11] J. Bear and Y. Bachmat. *Introduction to modeling of transport phenomena in porous media*. Kluwer Academic Publishers, 1991.

[12] W. Bensaid, J. T. Triffitt, C. Blanchat, K. Oudina, L. Sedel, and H. Petite. A biodegradable fibrin scaffold for mesenchymal stem cell transplantation. *Biomaterials*, 24(14):2497–2502, June 2003.

[13] M. A. Biot. General Theory of Three-Dimensional Consolidation. *Journal of Applied Physics*, 12(2):155–164, February 1941.

[14] G. Bluteau, P. Pilet, X. Bourges, M. Bilban, R. Spaethe, G. Daculsi, and J. Guicheux. The modulation of gene expression in osteoblasts by thrombin coated on biphasic calcium phosphate ceramic. *Biomaterials*, 27(15):2934–2943, 2006.

[15] T. Boyce, J. Edwards, and N. Scarborough. Allograft bone: The influence of processing on safety and performance. *Orthopedic Clinics of North America*, 30(4):571–581, 1999.

[16] R.A. Brand, R.D. Crowninshield, C.E. Wittstock, D.R. Pedersen, C.R. Clark, and F.M. van Krieken. A model of lower extremity muscular anatomy. *Journal of Biomechanical Engineering*, 104(4):304–10, 1982.

[17] R.A. Brand, D.R. Pedersen, D.T. Davy, G.M. Kotzar, K.G. Heiple, and V.M. Goldberg. Comparison of hip force calculations and measurements in the same patient. *Journal of Arthroplasty*, 9(1):45–51, 1994.

[18] J. D. Bryant, T. David, P. H. Gaskell, P. H. King, and G. Lond. Rheology of bovine bone marrow. *Proceedings of the Institution of Mechanical Engineers, Part H: Journal of Engineering in Medicine*, 203(2):71–75, 1989.

[19] P. Büchler, D. P. Pioletti, and L. Rakotomanana. Biphasic constitutive laws for biological interface evolution. *Biomechanics and Modeling in Mechanobiology*, 1(4):239–249, April 2003.

[20] P. Büchler, N.A. Raminaraka, L.R. Rakotomanana, J.P. Iannotti, and A. Farron. A finite element model of the shoulder: Application to the comparison of normal and osteoarthritic joints. *Clinical Biomechanics*, 17(9-10):630–639, 2002.

[21] R. W. Bucholz. Nonallograft osteoconductive bone graft substitutes. *Clinical Orthopaedics and Related Research*, (395):44–52, 2002.

[22] E. H. Burger and J. Klein-Nulend. Mechanotransduction in bone - role of the lacuno-canalicular network. *THE FASEB Journal*, 13:S101–S112, 1999.

[23] N. Caille, O. Thoumine, Y. Tardy, and J. J. Meister. Contribution of the nucleus to the mechanical properties of endothelial cells. *Journal of Biomechanics*, 35(2):177–187, February 2002.

[24] P. W. Carpenter, C. Davies, and A. D. Lucey. Hydrodynamics and compliant walls: Does the dolphin have a secret? *Current Science*, 79(6):758–765, September 2000.

[25] D. R. Carter. *Non-cemented total hip arthroplasty*, chapter The cemented acetabular component: biomechanics and skeletal adaptation, pages 257–276. Raven Press, New York, 1988.

[26] D. R. Carter, M. Wong, and T. E. Orr. Musculoskeletal ontogeny, phylogeny, and functional adaptation. *Journal of Biomechanics*, 24 Suppl 1:3–16, 1991.

[27] D.R. Carter, P.R. Blenman, and G.S. Beaupre. Correlations between mechanical stress history and tissue differentiation in initial fracture healing. *Journal of Orthopaedic Research*, 6(5):736–748, 1988.

[28] D.R. Carter, D.P. Fyhrie, and R.T. Whalen. Trabecular bone density and loading history: regulation of connective tissue biology by mechanical energy. *Journal of Biomechanics*, 20(8):785–794, 1987.

[29] B. S. Chang, C. K. Lee, K. S. Hong, H. J. Youn, H. S. Ryu, S. S. Chung, and K. W. Park. Osteoconduction at porous hydroxyapatite with various pore configurations. *Biomaterials*, 21(12):1291–1298, 2000.

[30] M. C. Chapuy, M. E. Arlot, F. Duboeuf, J. Brun, B. Crouzet, S. Arnaud, P. D. Delmas, and P. J. Meunier. Vitamin D3 and calcium to prevent hip fractures in the elderly women. *New England Journal of Medicine*, 327(23):1637–1642, 1992.

[31] N. X. Chen, K. D. Ryder, F. M. Pavalko, C. H. Turner, D. B. Burr, J. Qiu, and R. L. Duncan. Ca(2+) regulates fluid shear-induced cytoskeletal reorganization and gene expression in osteoblasts. *American Journal of Physiology. Cell Physiology*, 278(5):C989–997, May 2000.

[32] R. Chevray and J. Mathieu. *Topics in fluid mechanics*. Cambridge University Press, 1993.

[33] M. Chiquet. Regulation of extracellular matrix gene expression by mechanical stress. *Matrix Biology*, 18(5):417–426, 1999.

[34] J. Y. Choi, B. H. Lee, K. B. Song, R. W. Park, I. S. Kim, K. Y. Sohn, J. S. Jo, and H. M. Ryoo. Expression patterns of bone-related proteins during osteoblastic differentiation in mc3t3-el cells. *Journal of Cellular Biochemistry*, 64(4):609–618, June 1996.

[35] E.D. Clarkson. Fetal tissue transplantation for patients with Parkinson's disease: a database of published clinical results. *Drugs Aging*, 18(10):773–85, 2001.

[36] B. D. Coleman and W. Noll. Foundations of linear viscoelasticity. *Review of Modern Physics*, 3(2):239–249, 1961.

[37] P. Cordo, J. T. Inglis, S. Verschueren, J. J. Collins, D. M. Merfeld, S. Rosenblum, S. Buckley, and F. Moss. Noise in human muscle spindles. *Nature*, 383(6603):769–770, Oct 31 1996.

[38] M. Couette. Sur un nouvel appareil pour l'étude du frottement des fluides. *Compte Rendu de l'Académie des Sciences*, 107:388–390, 6 August 1888.

[39] O. Coussy. *Méchanique des milieux poreux*. Editions Technip, 1991.

[40] O. Coussy, L. Dormieux, and E. Detournay. From mixture theory to Biot's approach for porous media. *International Journal of Solids and Structures*, 35(34-35):4619–4635, December 1998.

[41] M. B. Coventry, D. M. Ilstrup, and S. L. Wallrichs. Proximal tibial osteotomy. a critical long-term study of eighty-seven cases. *The Journal of Bone and Joint Surgery. American volume*, 75(2):196–201, February 1993.

[42] Stephen C. Cowin. *Bone mechanics handbook*. CRC Press,, Boca Raton, 2nd edition, 2001.

[43] A. Curnier. *Mécanique des solides déformables : Volume 1, Cinématique, dynamique, énergétique*. Presses Polytechniques et Universitaires Romandes, 2005.

[44] C. S. Cutter and B. J. Mehrara. Bone grafts and substitutes. *Journal of Long-Term Effects of Medical Implants*, 16(3):249–60, 2006.

[45] I. Date, K. Kawamura, and H. Nakashima. Histological signs of immune reactions against allogeneic solid fetal neural grafts in the mouse cerebellum depend on the MHC locus. *Experimental Brain Research*, 73(1):15–22, 1988.

[46] P. F. Davies, T. Mundel, and K. A. Barbee. A mechanism for heterogeneous endothelial responses to flow in vivo and in vitro. *Journal of Biomechanics*, 28(12):1553–1560, 1995.

[47] S. W. Donahue, H. J. Donahue, and C. R. Jacobs. Osteoblastic cells have refractory periods for fluid-flow-induced intracellular calcium oscillations for short bouts of flow and display multiple low-magnitude oscillations during long-term flow. *Journal of Biomechanics*, 36(1):35–43, January 2003.

[48] T. L. Haut Donahue, M. L. Hull, M. M. Rashid, and C. R. Jacobs. How the stiffness of meniscal attachments and meniscal material properties affect tibio-femoral pressure computed using a validated finite element model of the human knee joint. *Journal of Biomechanics*, 36(1):19–34, 2003.

[49] W. M. Duan, H. Widner, E. M. Frodl, and P. Brundin. Immune reactions following systemic immunization prior or subsequent to intrastriatal transplantation of allogeneic mesencephalic tissue in adult rats. *Neuroscience*, 64(3):629–641, 1995.

[50] G. N. Duda, F. Mandruzzato, M. Heller, J. Goldhahn, R. Moser, M. Hehli, L. Claes, and N. P. Haas. Mechanical boundary conditions of fracture healing: borderline indications in the treatment of unreamed tibial nailing. *Journal of Biomechanics*, 34(5):639–650, 2001.

[51] D. M. Ehrler and A. R. Vaccaro. The use of allograft bone in lumbar spine surgery. *Clinical Orthopaedis and Relatated Research*, (371):38–45, 2000.

[52] I. Esenkaya and N. Elmali. Proximal tibia medial open-wedge osteotomy using plates with wedges: early results in 58 cases. *Knee Surgery, Sports Traumatology, Arthroscopy*, 14(10):955–961, 2006.

[53] M. Fabrizio and A. Morro. Thermodynamic restriction on relaxation functions in linear viscoelasticity. *Mechanics Research Communications*, 12(2):101–105, 1985.

[54] B. Fabry, G.N. Maksym, J.P. Butler, M. Glogauer, D. Navajas, and J.J. Fredberg. Scaling the microrheology of living cells. *Physical Review Letter*, 87(14):148102, 2001.

[55] J. Fang, R. Freeman, R. Jeganathan, and M. H. Alderman. Variations in hip fracture hospitalization rates among different race/ethnicity groups in New York city. *Ethnicity and Disease*, 14(2):280–284, Spring 2004.

[56] J. P. Fisher, J. W. Vehof, D. Dean, J. P. van der Waerden, T. A. Holland, A. G. Mikos, and J. A. Jansen. Soft and hard tissue response to photocrosslinked poly(propylene fumarate) scaffolds in a rabbit model. *Journal of Biomedical Material Research*, 59(3):547–556, 2002.

[57] E. A. Friis, R. S. Lakes, and J. B. Park. Negative Poisson's ratio polymeric and metallic foams. *Journal of Materials Science*, 23(12):4406–4414, December 1988.

[58] A. Frost, K. B. Jonsson, P. Ridefelt, O. Nilsson, S. Ljunghall, and O. Ljunggren. Thrombin, but not bradykinin, stimulates proliferation in isolated human osteoblasts, via a mechanism not dependent on endogenous prostaglandin formation. *Acta Orthopaedica Scandinavica*, 70(5):497–503, 1999.

[59] P.V. Giannoudis, H. Dinopoulos, and E. Tsiridis. Bone substitutes: an update. *Injury*, 36 Suppl 3:S20–7, 2005.

[60] L. J. Gibson and M. F. Ashby. *Cellular solids - Structure and properties*. Solid State Science. Press Syndicate of the University of Cambridge, The Pitt Building, Trumpington Street, Cambridge, CB2 1RP, UK, cambridge university press edition, 1997.

[61] A. S. Goldstein, T. M. Juarez, C. D. Helmke, M. C. Gustin, and A. G. Mikos. Effect of convection on osteoblastic cell growth and function in biodegradable polymer foam scaffolds. *Biomaterials*, 22(11):1279–1288, 2001.

[62] L. Han, J. A. Noble, and M. Burcher. A novel ultrasound indentation system for measuring biomechanical properties of in vivo soft tissue. *Ultrasound in Medicine & Biology*, 29(6):813–823, June 2003.

[63] E. J. Harper and W. Bonfield. Tensile characteristics of ten commercial acrylic bone cements. *Journal of Biomedical Materials Research*, 53(5):605–616, September 2000.

[64] R.C. Haut and R.W. Little. Rheological properties of canine anterior cruciate ligaments. *Journal of Biomechics*, 2(3):289–98, 1969.

[65] G. Hedlund and H. O. Sjogren. Induction of transplantation immunity to rat colon carcinoma isografts by implantation of intact fetal colon tissue. *International Journal of Cancer*, 26(1):71–73, 1980.

[66] P. Hernigou and W. Ma. Open wedge tibial osteotomy with acrylic bone cement as bone substitute. *The Knee*, 8(2):103–110, June 2001.

[67] P. Hernigou, D. Medevielle, J. Debeyre, and D. Goutallier. Proximal tibial osteotomy for osteoarthritis with varus deformity. a ten to thirteen-year follow-up study. *The Journal of Bone and Joint Surgery. American volume*, 69(3):332–354, March 1987.

[68] T. Hildebrand and P. Ruegsegger. A new method for the model-independent assessment of thickness in three-dimensional images. *Journal of Microscopy*, 185(1):67–75, 1997.

[69] P. F. Hill, V. Vedi, A. Williams, H. Iwaki, V. Pinskerova, and M. A. Freeman. Tibiofemoral movement 2: the loaded and unloaded living knee studied by mri. *The Journal of Bone and Joint Surgery. British volume*, 82(8):1196–1198, November 2000.

[70] J. Hohlfeld, A. de Buys Roessingh, N. Hirt-Burri, P. Chaubert, S. Gerber, C. Scaletta, P. Hohlfeld, and L.A. Applegate. Tissue engineered fetal skin constructs for paediatric burns. *Lancet*, 366(9488):840–842, 2005.

[71] G. A. Holzapfel. *Nonlinear Solid Mechanics*. John Wiley and sons, Ltd., 2000.

[72] H. A. Hoogendoorn, W. Renooij, L. M. Akkermans, W. Visser, and P. Wittebol. Long-term study of large ceramic implants (porous hydroxyapatite) in dog femora. *Clinical Orthopaedics and Related Research*, (187):281–288, 1984.

[73] K. A. Hooper, N. D. Macon, and J. Kohn. Comparative histological evaluation of new tyrosine-derived polymers and poly (L-lactic acid) as a function of polymer degradation. *Journal of Biomedical Materials Research*, 41(3):443–454, 1998.

[74] U. Hornung. *Homogenization and Porous Media*. Interdisciplinary Applied Mathematics. Springer-Verlag New York, Inc., 1997.

[75] Q. Huang, J.C. Goh, D.W. Hutmacher, and E.H. Lee. In vivo mesenchymal cell recruitment by a scaffold loaded with transforming growth factor beta1 and the potential for in situ chondrogenesis. *Tissue Engineering*, 8(3):469–82, 2002.

[76] M. J. Hubble. Bone grafts. *Surgical Technology International*, 10:261–265, 2002.

[77] R. Huiskes, W. D. Van Driel, P. J. Prendergast, and K. Søballe. A biomechanical regulatory model for periprosthetic fibrous-tissue differentiation. *Journal of Materials in Medicine*, 8:785–788, 1997.

[78] E.B. Hunziker and L.C. Rosenberg. Repair of partial-thickness defects in articular cartilage: cell recruitment from the synovial membrane. *Journal of Bone and Joint Surgury - Serie A*, 78(5):721–33, 1996.

[79] D. E. Hurwitz, D. R. Sumner, T. P. Andriacchi, and D. A. Sugar. Dynamic knee loads during gait predict proximal tibial bone distribution. *Journal of Biomechanics*, 31(5):423–430, 1998.

[80] A. Ignatius, H. Blessing, A. Liedert, C. Schmidt, C. Neidlinger-Wilke, D. Kaspar, B. Friemert, and L. Claes. Tissue engineering of bone: effects of mechanical strain on osteoblastic cells in type i collagen matrices. *Biomaterials*, 26(3):311–318, 2005.

[81] H. Iwaki, V. Pinskerova, and M. A. Freeman. Tibiofemoral movement 1: the shapes and relative movements of the femur and tibia in the unloaded cadaver knee. *The Journal of Bone and Joint Surgery. British volume*, 82(8):1189–1195, November 2000.

[82] D. Seligson J.A. Von Fraunhofer, L. A. Schaper. The rotational friction characteristics of human long bones. *Surface Technology*, 25(4):377–388, august 1985.

[83] C. R. Jacobs, C. E. Yellowley, B. R. Davis, Z. Zhou, J. M. Cimbala, and H. J. Donahue. Differential effect of steady versus oscillating flow on bone cells. *Journal of Biomechanics*, 31(11):969–976, 1998.

[84] C. R. Jacobs, J. You, G. Reilly, M. M. Saunders, K. Kurokouchi, C. E. Yellowley, and H. J. Donahue. An overview of oscialltory fluid flow as a potent loading-induced physical signal in bone cells. *American Society of Mechanical Engineers, Bioengineering Division*, BED 50:339–340, 2001.

[85] M. Jasty, C. Bragdon, D. Burke, D. O'Connor, J. Lowenstein, and W. H. Harris. In vivo skeletal responses to porous-surfaced implants subjected to small induced motions. *The Journal of Bone and Joint Surgery. American volume*, 79(5):707–714, May 1997.

[86] K.-L. C. Jen, A. Buison, L. Darga, and D. Nelson. The relationship between blood leptin level and bone density is specific to ethnicity and menopausal status. *Journal of Laboratory and Clinical Medicine*, 146(1):18–24, July 2005.

[87] G. L. Jiang, C. R. White, H. Y. Stevens, and J. A. Frangos. Temporal gradients in shear stimulate osteoblastic proliferation via erk1/2 and retinoblastoma protein. *American Journal of Physiology - Endocrinology and Metabolism*, 283(2):E383–E389, 2002.

[88] K. Jukkala-Partio, T. Pohjonen, O. Laitinen, E. K. Partio, J. Vasenius, T. Toivonen, J. Kinnunen, P. Tormala, and P. Rokkanen. Biodegradation and strength retention of poly-L-lactide screws in vivo. An experimental long-term study in sheep. *Annales Chirurgiae et Gynaecologiae*, 90(3):219–224, 2001.

[89] I. A. Kapandji. *Physiologie articulaire*, volume II. Maloine, 27, Rue de l'Ecole-de-Medecine, F-75006 Paris, 5eme edition edition, 1994.

[90] S. Kapur, D. J. Baylink, and K. H. W. Lau. Fluid flow shear stress stimulates human osteoblast proliferation and differentiation through multiple interacting and competing signal transduction pathways. *Bone*, 32(3):241–251, 2003.

[91] V. Karageorgiou and D. Kaplan. Porosity of 3D biomaterial scaffolds and osteogenesis. *Biomaterials*, 26(27):5474–5491, 2005.

[92] J. M. Karp, T. S. Tanaka, R. Zohar, J. Sodek, M. S. Shoichet, J. E. Davies, and W. L. Stanford. Thrombin mediated migration of osteogenic cells. *Bone*, 37(3):337–348, 2005.

[93] D. Kaspar, W. Seidl, C. Neidlinger-Wilke, A. Beck, L. Claes, and A. Ignatius. Proliferation of human-derived osteoblast-like cells depends on the cycle number and frequency of uniaxial strain. *Journal of Biomechanics*, 35(7):873–880, July 2002.

[94] D. Kaspar, W. Seidl, C. Neidlinger-Wilke, A. Ignatius, and L. Claes. Dynamic cell stretching increases human osteoblast proliferation and cicp synthesis but decreases osteocalcin synthesis and alkaline phosphatase activity. *Journal of Biomechanics*, 33(1):45–51, January 2000.

[95] T. M. Keaveny and O. C. Yeh. Architecture and trabecular bone - toward an improved understanding of the biomechanical effects of age, sex and osteoporosis. *Journal of Musculoskeletal Neuronal Interactions*, 2(3):205–208, 2002.

[96] J.C. Kennedy, R.J. Hawkins, R.B. Willis, and K.D. Danylchuck. Tension studies of human knee ligaments. Yield point, ultimate failure, and disruption of the cruciate and tibial collateral ligaments. *Journal of Bone and Joint Surgery. American Volume*, 58(3):350–5, 1976.

[97] S. N. Khan, H. S. Sandhu, J. M. Lane, F. P. Cammisa, Jr, and F. P. Girardi. Bone morphogenetic proteins: relevance in spine surgery. *The Orthopedic Clinics of North America*, 33(2):447–463, 2002.

[98] C. P. Klein, A. A. Driessen, K. de Groot, and A. van den Hooff. Biodegradation behavior of various calcium phosphate materials in bone tissue. *Journal of Biomedical Materials Research*, 17(5):769–784, 1983.

[99] J. Klein-Nulend, E. H. Burger, C. M. Semeins, L. G. Raisz, and C. C. Pilbeam. Pulsating fluid flow stimulates prostaglandin release and inducible prostaglandin g/h synthase mrna expression in primary mouse bone cells. *Journal of Bone and Mineral Research*, 12(1):45–51, January 1997.

[100] T. Koshino, T. Murase, and T. Saito. Medial opening-wedge high tibial osteotomy with use of porous hydroxyapatite to treat medial compartment osteoarthritis of the knee. *The Journal of Bone and Joint Surgery. American volume*, 85-A(1):78–85, January 2003.

[101] M. Krasnov, A. Kisselev, G. Makarenko, and E. Chikine. *Mathematiques superieures pour ingenieurs et polytechniciens*. Acces Sciences. De Boeck-Wesmael, 1993.

[102] S. Kujala, J. Ryhanen, A. Danilov, and J. Tuukkanen. Effect of porosity on the osteointegration and bone ingrowth of a weight-bearing nickel-titanium bone graft substitute. *Biomaterials*, 24(25):4691–4697, 2003.

[103] L.E. Lanyon, W.G. Hampson, A.E. Goodship, and J.S. Shah. Bone deformation recorded in vivo from strain gauges attached to the human tibial shaft. *Acta Orthopaedica Scandinavica*, 46(2):256–68, 1975.

[104] K.H. Lau, S. Kapur, C. Kesavan, and D.J. Baylink. Up-regulation of the Wnt, estrogen receptor, insulin-like growth factor-I, and bone morphogenetic protein pathways in C57BL/6J osteoblasts as opposed to C3H/HeJ osteoblasts in part contributes to the differential anabolic response to fluid shear. *Journal of Biological Chemistry*, 281(14):9576–9588, 2006.

[105] R. C. Lawrence, C. G. Helmick, F. C. Arnett, R. A. Deyo, D. T. Felson, E. H. Giannini, S. P. Heyse, R. Hirsch, M. C. Hochberg, G. G. Hunter, M. H. Liang, S. R. Pillemer, V. D. Steen, and F. Wolfe. Estimates of the prevalence of arthritis and selected musculoskeletal disorders in the united states. *Arthritis and Rheumatism*, 41(5):778–799, May 1998.

[106] J. Lemaitre and J.-L. Chaboche. *Mécanique des matériaux solides*. Dunod, 1985.

[107] G. Li, Y. Cui, L. McIlmurray, W. E. Allen, and H. Wang. rhBMP-2, rhVEGF(165), rhPTN and thrombin-related peptide, TP508 induce chemotaxis of human osteoblasts and microvascular endothelial cells. *Journal of Orthopaedic Research*, 23(3):680–685, 2005.

[108] D. R. Lide. *CRC Handbook of Chemistry and Physics*. CRC Press, 85th edition, 2005.

[109] F. Linde, P. Norgaard, I. Hvid, A. Odgaard, and K. Soballe. Mechanical properties of trabecular bone dependency on strain rate. *Journal of Biomechanics*, 24(9):803–809, 1991.

[110] J.B. Litzenberger, P. Tummala, and C.R. Jacobs. Integrin signaling and the response of osteocytes to oscillatory fluid flow. *MCB Molecular and Cellular Biomechanics*, 3(4):219–220, 2006.

[111] P. Lobenhoffer, J. Agneskirchner, and W. Zoch. Open-wedge high tibial osteotomy with special medial plate fixator. *Der Orthopaede*, 33(2):153–160, January 2004.

[112] J.X. Lu, B. Flautre, K. Anselme, P. Hardouin, A. Gallur, M. Descamps, and B. Thierry. Role of interconnections in porous bioceramics on bone recolonization in vitro and in vivo. *Journal of Materials Science. Materials in Medicine*, 10(2):111–120, 1999.

[113] F. Luppé, J.-M. Connoir, and H. Franklin. Scattering by a fluid cylinder in a porous medium: Application to trabecular bone. *Journal of Acoustical Society of America*, 111(6):2573–2582, June 2002.

[114] E.J. Mackie and U. Trechsel. Stimulation of bone formation in vivo by transforming growth factor-beta: remodeling of woven bone and lack of inhibition by indomethacin. *Bone*, 11(4):295–300, 1990.

[115] M. E. Maragoudakis, N. E. Tsopanoglou, and P. Andriopoulou. Mechanism of thrombin-induced angiogenesis. *Biochemical Society Transactions*, 30(2):173–177, 2002.

[116] P. J Marie, F. Debiais, and E. Hay. Regulation of human cranial osteoblast phenotype by FGF-2, FGFR-2 and BMP-2 signaling. *Histology and histopathology*, 17(3):877–885, 2002.

[117] C.B. Marti and R.P. Jakob. Accumulation of irrigation fluid in the calf as a complication during high tibial osteotomy combined with simultaneous arthroscopic anterior cruciate ligament reconstruction. *Arthroscopy*, 15(8):864–866, 1999.

[118] L. Mathieu. *Processing of Porous Polymer Composites for Bone Tissue Engineering*. Phd thesis n° 3121, Ecole Polytechnique Fédérale de Lausanne, 2004.

[119] L. M. Mathieu, M.-O. Montjovent, P-E. Bourban, D. P. Pioletti, and J.-A. E. Månson. Bioresorbable composites prepared by supercritical fluid foaming. *Journal of Biomedical Materials Research - Part A*, 75(1):89–97, October 2005.

[120] Y. Matsusue, T. Yamamuro, M. Oka, Y. Shikinami, S. H. Hyon, and Y. Ikada. In vitro and in vivo studies on bioabsorbable ultra-high-strength poly(L-lactide) rods. *Journal of Biomedical Materials Research*, 26(12):1553–1567, 1992.

[121] R. Mohle, D. Green, M. A. Moore, R. L. Nachman, and S. Rafii. Constitutive production and thrombin-induced release of vascular endothelial growth factor by human megakaryocytes and platelets. *Proceedings of the National Academy of Sciences of the United States of America*, 94(2):663–668, 1997.

[122] M.-O. Montjovent, N. Burri, S. Mark, E. Federici, C. Scaletta, P.-Y. Zambelli, P. Hohlfeld, P.-F. Leyvraz, L. L. Applegate, and D. P. Pioletti. Fetal bone cells for tissue engineering. *Bone*, 35(6):1323–1333, December 2004.

[123] M.-O. Montjovent, L. Mathieu, B. Hinz, L. L. Applegate, P.-E. Bourban, P.-Y. Zambelli, J.-A. Månson, and D. P. Pioletti. Biocompatibility of bioresorbable poly(l-lactic acid) composite scaffolds obtained by supercritical gas foaming with human fetal bone cells. *Tissue Engineering*, 11(11-12):1640–1649, November 2005.

[124] W.R. Moore, S.E. Graves, and G.I. Bain. Synthetic bone graft substitutes. *ANZ Journal of Surgery*, 71(6):354–61, 2001.

[125] M. Mullender, A. J. El Haj, Y. Yang, M. A. van Duin, E. H. Burger, and J. Klein-Nulend. Mechanotransduction of bone cells in vitro: mechanobiology of bone tissue. *Medical & Biological Engineering & Computing*, 42(1):14–21, January 2004.

[126] E. Namihira. Shinto concept concerning the dead human body. *Transplantation Proceedings*, 22(3):940–941, 1990.

[127] K. W. Ng, D. T. Leong, and D. W. Hutmacher. The challenge to measure cell proliferation in two and three dimensions. *Tissue Engineering*, 11(1-2):182–191, January-February 2005.

[128] B. E. Nilsson and N. E. Westlin. Bone density in athletes. *Clinical Orthopaedics and Related Research*, 77:179–182, 1971.

[129] T. Niu and C. J. Rosen. The insulin-like growth factor-I gene and osteoporosis: a critical appraisal. *Gene*, 361:38–56, 2005.

[130] M. Noda and J.J. Camilliere. In vivo stimulation of bone formation by transforming growth factor-beta. *Endocrinology*, 124(6):2991–4, 1989.

[131] J. Oertel, M. Samii, and G. F. Walter. Fetal allogeneic dopaminergic cell suspension grafts in the ventricular system of the rat: characterization of transplant morphology and graft-host interactions. *Acta Neuropathologica*, 107(5):421–427, 2004.

[132] A. Ogasawara, T. Arakawa, T. Kaneda, T. Takuma, T. Sato, H. Kaneko, M. Kumegawa, and Y. Hakeda. Fluid shear stress-induced cyclooxygenase-2 expression is mediated by c/ebp beta, camp-response element-binding protein, and ap-1 in osteoblastic mc3t3-e1 cells. *The Journal of Biological Chemistry*, 276(10):7048–7054, Mar 9 2001.

[133] C.A. Paccola and F. Fogagnolo. Open-wedge high tibial osteotomy: a technical trick to avoid loss of reduction of the opposite cortex. *Knee Surgery, Sports Traumatology, Arthroscopy*, 13(1):19–22, 2005.

[134] V. V. Paciauskas and P. A. Domenico. Fluid pressures in deforming porous rocks. *Water Resources Research*, 25(2):203–213, 1989.

[135] C. N. Pagel, M. R. de Niese, L. A. Abraham, C. Chinni, S. J. Song, R. N. Pike, and E. J. Mackie. Inhibition of osteoblast apoptosis by thrombin. *Bone*, 33(4):733–743, 2003.

[136] F.S. Panagakos. Transforming growth factor–alpha stimulates chemotaxis of osteoblasts and osteoblast-like cells in vitro. *Biochemistry And Molecular Biology International*, 33(4):643–50, 1994.

[137] A. M. Parfitt, Z.-H. Han, S. Palnitkar, D. S. Rao, M.-S. Shih, and D. Nelson. Effects of ethnicity and age or menopause on osteoblast function, bone mineralization, and osteoid accumulation in iliac bone. *Journal of Bone and Mineral Research*, 12(11):1864–1873, November 1997.

[138] S.N. Parikh. Bone graft substitutes: past, present, future. *Journal of Postgraduate Medicine*, 48(2):142–8, 2002.

[139] R. M. Pilliar, J. M. Lee, and C. Maniatopoulos. Observations on the effect of movement on bone ingrowth into porous-surfaced implants. *Clinical Orthopaedics and Related Research*, (208):108–113, July 1986.

[140] D. P. Pioletti. *Viscoelastic properties of soft tissues: Application to knee ligaments and tendons*. Phd thesis n° 1643, Ecole Polytechnique Fédérale de Lausanne, 1997.

[141] D. P. Pioletti, L. R. Rakotomanana, J. F. Benvenuti, and P. F. Leyvraz. Viscoelastic constitutive law in large deformations: application to human knee ligaments and tendons. *Journal of Biomechanics*, 31(8):753–757, 1998.

[142] D. P. Pioletti, L. R. Rakotomanana, P. Dahlgren, J. Vallotton, and P. F. Leyvraz. Intrinsic coordinate system for the tibial plateau. *The Knee*, 5(2):95–98, 1998.

[143] T. E. Popowics, Z. Zhu, and S. W. Herring. Mechanical properties of the periosteum in the pig, sus scrofa. *Archives of Oral Biology*, 47(10):733–741, October 2002.

[144] P. J. Prendergast, R. Huiskes, and K. Soballe. ESB research award 1996. biophysical stimuli on cells during tissue differentiation at implant interfaces. *Journal of Biomechanics*, 30(6):539–548, June 1997.

[145] Y.-X. Qin, C. T. Rubin, and K. J. McLeod. Nonlinear dependence of loading intensity and cycle number in the maintenance of bone mass and morphology. *Journal of Orthopaedic Research*, 16(4):482–489, July 1998.

[146] A. Quintin, N. Hirt-Buri, C. Scaletta, C. Schizas, D. P. Pioletti, and L. A. Appelgate. Consitency of fetal cells banks for research and clinical use. *Cell Transplantation*, In Press, 1007.

[147] L. R. Rakotomanana. *Dynamique des structures elastiques*. University of Rennes I, 2003.

[148] R. L. Rakotomanana, P. F. Leyvraz, A. Curnier, J. H. Heegaard, and P. J. Rubin. A finite-element model for evaluation of tibial prosthesis bone interface in total knee replacement. *Journal of Biomechanics*, 25(12):1413–1424, 1992.

[149] N.A. Ramaniraka, A. Terrier, N Theumann, and O. Siegrist. A numerical study on the influence of graft mechanical properties after posterior cruciate (pcl) reconstruction. In *International Congress on Computational Bioengineering*, pages 417–422, 2003.

[150] K. M. Reich, C. V. Gay, and J. A. Frangos. Fluid shear-stress as a mediator of osteoblast cyclic adenosine-monophosphate production. *Journal of Cellular Physiology*, 143(1):100–104, 1990.

[151] P. J. Reier. Cellular transplantation strategies for spinal cord injury and translational neurobiology. *NeuroRx: the journal of the American Society for Experimental NeuroTherapeutics*, 1(4):424–451, 2004.

[152] D. T. Reilly and A. H. Burstein. The elastic and ultimate properties of compact bone tissue. *Journal of Biomechanics*, 8(6):393–405, 1975.

[153] W. Renooij, H.A. Hoogendoorn, W.J. Visser, R.H. Lentferink, M.G. Schmitz, H. Van Ieperen, S.J. Oldenburg, W.M. Janssen, L.M. Akkermans, and P. Wittebol. Bioresorption of ceramic strontium-85-labeled calcium phosphate implants in dog femora. A pilot study to quantitate bioresorption of ceramic implants of hydroxyapatite and tricalcium orthophosphate in vivo. *Clinical Orthopaedics and Related Research*, (197):272–285, 1985.

[154] J. C. Rice, S. C. Cowin, and J. A. Bowman. On the dependence of the elasticity and strength of cancellous bone on apparent density. *Journal of Biomechanics*, 21(2):155–168, 1988.

[155] M. L Richardson. Anteroposterior (AP) view of the legs in a 2 year old child with rickets, 28 September 2004.

[156] A.E. Rosser and S.B. Dunnett. Neural transplantation in patients with Huntington's disease. *CNS Drugs*, 17(12):853–867, 2003.

[157] C. Rubin, R. Recker, D. Cullen, J. Ryaby, J. McCabe, and K. McLeob. Prevention of postmenopausal bone loss by a low-magnitude, high-frequency mechanical stimuli: A clinical trial assessing compliance, efficacy, and safety. *Journal of Bone and Mineral Research*, 19(3):343–351, March 2004.

[158] C. T. Rubin, K. J. McLeod, and S. D. Bain. Functional strains and cortical bone adaptation: epigenetic assurance of skeletal integrity. *Journal of Biomechanics*, 23 Suppl 1:43–54, 1990.

[159] J. Rubin, C. Rubin, and C.R. Jacobs. Molecular pathways mediating mechanical signaling in bone. *Gene*, 367:1–16, 2006.

[160] P. J. Rubin, R. L. Rakotomanana, P. F. Leyvraz, P. K. Zysset, A. Curnier, and J. H. Heegaard. Frictional interface micromotions and anisotropic stress-distribution in a femoral total hip component. *Journal of Biomechanics*, 26(6):725–739, 1993.

[161] K. Sakai, M. Mohtai, and Y. Iwamoto. Fluid shear stress increases transforming growth factor beta 1 expression in human osteoblast-like cells: modulation by cation channel blockades. *Calcified Tissue International*, 63(6):515–520, 1998.

[162] H. S. Sandhu, H. S. Grewal, and H. Parvataneni. Bone grafting for spinal fusion. *Orthopedic Clinics of North America*, 30(4):685–698, 1999.

[163] R. Sanjeevi. A viscoelastic model for the mechanical properties of biological materials. *Journal of Biomechanics*, 15(2):107–9, 1982.

[164] H. Sato and S. Morishita. Effect of quadriceps exercise on synostosis following tibial osteotomy with internal fixation: a finite element simulation. *Clinical Biomechanics*, 14(1):1–6, January 1999.

[165] J. Schmitt, J. Meiforth, and M. Lengsfeld. Development of a hybrid finite element model for individual simulation of intertrochanteric osteotomies. *Medical Engineering & Physics*, 23(8):529–539, 2001.

[166] L. Sharma, J. Song, D. T. Felson, S. Cahue, E. Shamiyeh, and D. D. Dunlop. The role of knee alignment in disease progression and functional decline in knee osteoarthritis. *Journal of the American Medical Association*, 286(2):188–195, 2001.

[167] J. S. Shockey, J. A. von Fraunhofer, and D. Seligson. A measurement of the coefficient of static friction of human long bones. *Surface Technology*, 25(2):167–173, june 1985.

[168] R. E. Showalter and B. Momken. Single-phase flow in composite poroelastic media. *Mathematical Methods in the Applied Sciences*, 25(2):115–139, January 2002.

[169] V. I. Sikavitsas, G. N. Bancroft, H. L. Holtorf, J. A. Jansen, and A. G. Mikos. Mineralized matrix deposition by marrow stromal osteoblasts in 3d perfusion culture increases with increasing fluid shear forces. *Proceedings of the National Academy of Sciences of the United States of America*, 100(25):14683–14688, December 9 2003.

[170] S. M. Smith, M. E. Wastney, K. O. O'Brien, B. V. Morukov, I. M. Larina, S. A. Abrams, J. E. Davis-Street, V. Oganov, and L. C. Shackelford. Bone markers, calcium metabolism, and calcium kinetics during extended-duration space flight on the mir space station. *Journal of Bone and Minereral Research*, 20(2):208–218, February 2005.

[171] K. Soballe, H. Brockstedt-Rasmussen, E. S. Hansen, and C. Bunger. Hydroxyapatite coating modifies implant membrane formation. controlled micromotion studied in dogs. *Acta Orthopaedica Scandinavica*, 63(2):128–140, April 1992.

[172] K. Soballe, E. S. Hansen, H. B-Rasmussen, P. H. Jorgensen, and C. Bunger. Tissue ingrowth into titanium and hydroxyapatite-coated implants during stable and unstable mechanical conditions. *Journal of Orthopaedic Research*, 10(2):285–299, March 1992.

[173] K. Soballe, E. S. Hansen, H. Brockstedt-Rasmussen, and C. Bunger. Hydroxyapatite coating converts fibrous tissue to bone around loaded implants. *The Journal of Bone and Joint Surgery. British volume*, 75(2):270–278, March 1993.

[174] A. E. Staubli, C. De Simoni, R. Babst, and P. Lobenhoffer. Tomofix: a new lcp-concept for open wedge osteotomy of the medial proximal tibia - early results in 92 cases. *Injury*, 34 Suppl 2:B55–62, November 2003.

[175] S. Stevenson, S.E. Emery, and V.M. Goldberg. Factors affecting bone graft incorporation. *Clinical Orthopaedics and Related Research*, (324):66–74, 1996.

[176] J. M. Stewart, C. Karman, L. D. Montgomery, and K. J. McLeod. Plantar vibration improves leg fluid flow in perimenopausal women. *American Journal of Physiology - Regulatory, Integrative and Comparative Physiology*, 288(3 57-3):R623–R629, March 2005.

[177] L. C. E. Struik. *Physical aging in amorphous polymers and other materials*. Elsevier Scientific Publishing Company, 1978.

[178] B. N. Summers and S. M. Eisenstein. Donor site pain from the ilium. a complication of lumbar spine fusion. *Journal of Bone and Joint Surgery - Series B*, 71(4):677–680, 1989.

[179] R. Suuronen, T. Pohjonen, J. Hietanen, and C. Lindqvist. A 5-year in vitro and in vivo study of the biodegradation of polylactide plates. *Journal of Oral and Maxillofacial Surgery*, 56(5):604–615, 1998.

[180] C. C. Swan, R. S. Lakes, R. A. Brand, and K. J. Stewart. Micromechanically based poroelastic modeling of fluid flow in haversian bone. *Journal of Biomechanical Engineering*, 125(1):25–37, 2003.

[181] S. M. Tanaka, I. M. Alam, and C. H. Turner. Stochastic resonance in osteogenic response to mechanical loading. *The FASEB Journal*, 17(2):313–314, February 2003.

[182] S. M. Tanaka, J. Li, R. L. Duncan, H. Yokota, D. B. Burr, and C. H. Turner. Effects of broad frequency vibration on cultured osteoblasts. *Journal of Biomechanics*, 36(1):73–80, January 2003.

[183] S. J. Taylor, J. S. Perry, J. M. Meswania, N. Donaldson, P. S. Walker, and S. R. Cannon. Telemetry of forces from proximal femoral replacements and relevance to fixation. *Journal of Biomechanics*, 30(3):225–234, March 1997.

[184] H. Teramoto, A. Kawai, S. Sugihara, A. Yoshida, and H. Inoue. Resorption of apatite-wollastonite containing glass-ceramic and beta-tricalcium phosphate in vivo. *Acta Medica Okayama*, 59(5):201–207, 2005.

[185] A. Terrier. *Adaptation of bone to mechanical stress: Theoretical model, experimental identification and orthopedic applications*. Phd thesis n°2048, Ecole Polytechnique Fédérale de Lausanne, 1999.

[186] K. Terzaghi. *Erdbaumechanik auf bodenphysikalischer Grundlage*. Deuticke, Leipzig, 1925.

[187] R. R. Tjandrawinata, V. L. Vincent, and M. Hughes-Fulford. Vibrational force alters mrna expression in osteoblasts. *The FASEB Journal*, 11(6):493–7, May 1997.

[188] J. L. Touraine, M. G. Roncarolo, R. Bacchetta, D. Raudrant, A. Rebaud, S. Laplace, P. Cesbron, L. Gebuhrer, M.T. Zabot, F. Touraine, and et al. Fetal liver transplantation: biology and clinical results. *Bone Marrow Transplantation*, 11 Suppl 1:119–122, 1993.

[189] C. H. Turner. Three rules for bone adaptation to mechanical stimuli. *Bone*, 23(5):399–407, November 1998.

[190] C. H. Turner and A. G. Robling. Mechanical loading and bone formation. *BoneKEy-Osteovision*, 1(9):15–23, September 2004.

[191] E. Uchiyama, K. Yamakoshi, and T. Sasaki. Measurement of mechanical characteristics of tibial periosteum and evaluation of local differences. *Journal of Biomechanical Engineering*, 120(1):85–91, February 1998.

[192] R. L. Valmassy. *Clinical biomechanics of the lower extremities*. Mosby, 1996.

[193] S. Wadhwa, S. Choudhary, M. Voznesensky, M. Epstein, L. Raisz, and C. Pilbeam. Fluid flow induces cox-2 expression in mc3t3m-e1 osteoblasts via a pka signaling pathway. *Biochemical and Biophysical Research Communications*, 297(1):46–51, 2002.

[194] H. Wang, X. Li, E. Tomin, S. B. Doty, J. M. Lane, D. H. Carney, and J. T. Ryaby. Thrombin peptide (TP508) promotes fracture repair by up-regulating inflammatory mediators, early growth factors, and increasing angiogenesis. *Journal of Orthopedic Research*, 23(3):671–679, 2005.

[195] G. M. Wardlaw. Putting body weight and osteoporosis into perspective. *American Journal of Clinical Nutrition*, 63(3 Suppl):433S–436S, 1996.

[196] K. Whang, T. K. Goldstick, and K. E. Healy. A biodegradable polymer scaffold for delivery of osteogenic factors. *Biomaterials*, 21:2542–2551, 2000.

[197] G. D. Whedon. Disuse osteoporosis: physiological aspects. *Calcified Tissue International*, 36 Suppl 1:S146–150, 1984.

[198] J. L. Williams and J. L. Lewis. Properties and an anisotropic model of cancellous bone from the proximal tibial epiphysis. *Journal of Biomechanical Engineering*, 104(1):505–506, February 1982.

[199] P. Wretenberg, D. K. Ramsey, and G. Nemeth. Tibiofemoral contact points relative to flexion angle measured with mri. *Clinical Biomechanics*, 17(6):477–485, July 2002.

[200] J. You, C. E. Yellowley, H. J. Donahue, Y. Zhang, Q. Chen, and C. R. Jacobs. Substrate deformation levels associated with routine physical activity are less stimulatory to bone cells relative to loading-induced oscillatory fluid flow. *Journal of Biomechanical Engineering*, 122(4):387–393, 2000.

[201] L. You, S. C. Cowin, M. B. Schaffler, and S. Weinbaum. A model for strain amplification in the actin cytoskeleton of osteocytes due to fluid drag on pericellular matrix. *Journal of Biomechanics*, 34(11):1375–1386, 2001.

[202] E. M. Younger and M. W. Chapman. Morbidity at bone graft donor sites. *Journal of Orthopaedic Trauma*, 3(3):192–195, 1989.

[203] C. Zhang, J. Wang, H. Feng, B. Lu, Z. Song, and X. Zhang. Replacement of segmental bone defects using porous bioceramic cylinders: a biomechanical and X-ray diffraction study. *Journal of Biomedical Materials Research*, 54(3):407–411, 2001.

[204] L. J. Zhao, Y. J. Liu, P. Y. Liu, J. Hamilton, R. R. Recker, and H. W. Deng. Relationship of obesity with osteoporosis. *Journal of Clinical Endocrinology Metabolism*, In Press, 13 February 2007.

[205] L. Zou, X. Zou, H. Li, T. Mygind, Y. Zeng, N. Lu, and C. Bunger. Molecular mechanism of osteochondroprogenitor fate determination during bone formation. *Advances in Experimental Medicine and Biology*, 585:431–441, 2006.

Curriculum Vitae

BLECHA Luc
Bd de Grancy 30
CH-1006 Lausanne

Swiss
32 years
single

Formations

April 2003 - June 2007

Doctoral Degree ès Sciences

Laboratory for Biomechanical Orthopaedics, Ecole Polytechnique Fédérale de Lausanne (EPFL), Switzerland

Theoretical and Experimental Multi-Scale Study Of An Artificial Bone Construct: From Tibial Osteotomy To Cell/Fluid Interaction

Thesis directions: Pr. D.P. Pioletti (EPFL) & Pr. L.R. Rakotomanana (IRMAR, Université de Rennes I, France)

April 1999

Diploma of Mechanical Engineer ETH

Swiss Federal Institute of Technology Zurich (ETHZ), Switzerland

Specializations: Aeronautical Structures, Pr. Dr. H.-R. Meyer-Piening; Fluid Mechanics, Pr. Dr. L. Kleiser

Diploma Thesis

Southampton Institute of Higher Education (SIHE), UK

Numerical and Experimental Investigation of the Active Keel's Concept

Direction: Pr. Dr. Kleiser (ETHZ) & Pr. Dr. O. Khattab (SIHE)

1994

Scientific Baccalauréat

Public high school of Nyon, Switzerland

Work Experiences

November 2000 to
April 2003

Structural Engineer

Structural & Numerical Analysis Office, APCO Technologies SA, Switzerland

Designs, numerical simulations and validations of flight hardware according to ESA and NASA standards.

January 2000 to
November 2000

Quality Assurance Engineer

Quality Assurance Office, APCO Technologies SA, Switzerland

Document elaboration and test definition related to the quality assurance requirements. Client receptions and follow through manufacturing subcontractors.

Traineeship

1997 - 1998
3 semesters

Demonstrator

Institute of Fluid Mechanics, ETHZ, Switzerland

Helping the students during the tutorial and evaluation of their written exercises.

1997
12 weeks

Trainee Period

Technical University of Eindhoven (TUE), The Netherlands

Modeling of bubbles trajectories in accelerated flow for a project founded by Shell.

Langages

French: Mother tongue
English: Fluent (FCE grade A)
German: Good
Spanish: Good

Publications

Articles

Blecha LD, Zambelli PY, Ramaniraka NA, Rakotomanana LR, Bourban P-E, Manson J-A, Pioletti DP, How Plate Positioning Impacts the Biomechanics of the Open Wedge Varus Osteotomy; a Finite Element Analysis. *Computer Methods in Biomechanics and Biomedical Engineering*, 8(5), October 2005.

Blecha LD, Rakotomanana LR, Razafimahery F, Zambelli P-Y, Pioletti DP, Mechanical interaction between cell and fluid: modulation of the fluid-induced interfacial shear stress, *Submitted*, 2007.

Blecha LD, Rakotomanana LR, Razafimahery F, Pioletti DP, Target Mechanical properties for optimal fluid motion inside artificial bone constructs, *Submitted*, 2007.

Book Chapters

Blecha LD, Rakotomanana LN, Razafimahery F, Zambelli P-Y, Pioletti DP, Mechanical interaction between fluid and cell modulates fluid flow induced shear stress, *In: Computer Methods in Biomechanics and Biomedical Engineering*, edited by Middleton J et al., 2006.

Abstracts

Blecha LD, Zambelli PY, Ramaniraka NA, Rakotomanana LR, Bourban P-E, Manson J-A, Pioletti DP, How Plate Positioning Impacts the Biomechanics of the Open Wedge Varus Osteotomy; a Finite Element Analysis, Poster at the Congress of the International Union for Theoretical and Applied Mechanics, Graz, Austria, Juin 2004.

Blecha LD, Zambelli PY, Ramaniraka NA, Rakotomanana LR, Bourban P-E, Manson J-A, Pioletti DP, Finite Element Analysis of an Open-Wedge Varus Tibial Osteotomy: Effect of Supporting Plate Position, Oral presentation at Congress of the Société de Biomécanique, Paris, France, September 2004.

Blecha LD, Zambelli P.-Y, Ramaniraka NA, Rakotomanana LR, Bourban P-E, Manson J-A, Pioletti DP, Effect Of The Scaffold Mechanical Properties On Interface Micromotions And Stress Distribution In Tibial Open Wedge Osteotomy, Oral presentation at the European Orthopaedic Research Society, Amsterdam, The Netherlands, November 2004.

Blecha LD, Zambelli P-Y, Ramaniraka NA, Rakotomanana LR, Bourban P-E, Manson J-A, Pioletti DP, Effect Of The Scaffold Mechanical Properties On Interface Micromotion And Stress Distribution In Tibial Open Wedge Osteotomy, Poster at the TESI, Lausanne, Switzerland, 2004.

Blecha LD, Montjovent M-O, Jaccoud S, Appelgate L, Pioletti DP, Impregnation of Porous Scaffold with Human Fetal Cells Entrapped in Fibrin Gel for Bone Tissue Engineered Applications, Oral presentation at the European Orthopaedic Research Society, Lisbon, Portugal, June 2005.

Blecha LD, Rakotomanana L, Razafimahery F, Zambelli P-Y, Pioletti DP, Mechanical Interaction Between Fluid And Cell Modulates Fluid Flow Induced Shear Stress, Oral presentation at the Computer Methods in Biomechanics and Biomedical Engineering, Antibes, France, February 2006.

Blecha LD, Rakotomanana L, Razafimahery F, Zambelli P-Y, Pioletti DP, Dynamic Shear Stress At Cell's Membrane Is Governed By Mechanical Interaction Between Fluid And Cell, Oral presentation at the World Congress of Biomechanic, Munich, Germany, August 2006.